ACOUSTICAL EMISSION TECHNIQUES FOR
DETECTION OF METALLIC LOOSE PARTS
IN A BOILING WATER REACTOR

A Thesis

Submitted to the Graduate Faculty of the
Louisiana State University and
Agricultural and Mechanical College
in partial fulfillment of the
requirements for the degree of
Master of Science

in

The Department of Nuclear Engineering

by
Hosein Zadafshar
B.A.Sc., Louisiana State University, 1981
May 1984

ACKNOWLEDGEMENTS

TABLE OF CONTENTS

TABLE OF CONTENTS (Continued)

TABLE OF CONTENTS (Continued)

LIST OF TABLES

LIST OF FIGURES

LIST OF FIGURES (Continued)

LIST OF FIGURES (Continued)

ABSTRACT

The Advisory Committee on Reactor Safeguards and the Nuclear Regulatory Commission, through Nuclear Regulatory Guide 1.133, have emphasized the need for loose parts monitoring systems for nuclear-heated electric plants. Such systems are being used effectively for pressurized-water reactors, but the applicability to boiling-water reactors has been debated. Analysis of the General Electric BWR/6 systems has led to identification of likely loose parts migration paths within the reactor vessel, with the conclusion that all paths may ultimately end at the control bottom lower plenum. Parts would have to be lifted from this region and carried upward toward the fuel coolant channels. Channel blockage is unlikely, and excessive heating of an element therefore has a low probability. Equations and calculational procedures for evaluating impact-induced stresses in reactor components were developed to be tested when adequate data can be acquired from operating reactors. The tank for a subcritical assembly was modified to simulate boiling with compressed air bubbling as a test bed for evaluating acoustical sensors for impact location. An array of six Acoustical Emission Technology Model AC 175-L sensors were fixed to the tank walls in a double-

diamond geometry. Time-of-arrival signals from the impact

of a spring-fired BB delivering 0.3j to the wall were

employed for two-dimension calculation of the impact

point. This time-differencing procedure was successful

to within less than $\pm$ 1 cm between the known and

calculated impact point when the impact was at least 20 cm

from the nearest of three array sensors. Closer approach

could be anticipated for sensors with faster resolving

time. Based on the experimental results and BWR/6

considerations, it is believed that four sensors would be

adequate for location of loose parts impacts in the bottom

plenum of the reactor vessel. However, because of

regulatory restrictions limiting sensor attachment only

to control-rod shrouds, direct experimental verification

with simulated shroud tubes on the subcritical tank will

be required.

Chapter 1

NATURE OF THE PROBLEM AND RELATED BACKGROUND

The Advisory Committee on Reactor Safeguards (ACRS)
and the Nuclear Regulatory Commission (NRC) staff have,
for the past several years, been encouraging applicants
to employ online loose-part detection systems in an
attempt to stimulate technological development in that
area.[1] The NRC Regulatory Guide 1.133, "Loose Part
Detection Program for the Primary System of Light-Water-
Cooled Reactors", emphasizes this need, stating that all
applicants for a construction permit or an operating
license are required to describe the loose-part detection
program for the proposed reactor. The presence of loose
parts in primary coolant system of today's nuclear re-
actors is a proven reality. Thus, the characterization
of a loose part as to its location, probable size, and
an estimate of its origin is valuable information for con-
tinuing safe and economical operation of a nuclear power
plant.

Loose parts monitoring is straight forward and
effective in a pressurized water reactor (PWR) which
operates in a generally quiet mode. In a boiling water
reactor (BWR), however, the noise introduced by boiling
imposes a high background which must be overcome by any

acoustical noise detection system. Both accelerometer and acoustical-signature techniques may be confounded by the background operating noise.

Background Information

The presence of a loose part in the primary coolant system can be indicative of degraded reactor safety resulting from failure or weakening of a safety-related component. A loose part, whether it be from a failed or weakened component or from an item inadvertently left in the primary system during construction, refueling, or maintenance procedures, can contribute to component damage and material wear by frequent impacting with other parts in the system. The metal-to-metal impact causes the initiation of an impact wave on the surface of the metallic structure. A loose part can pose a serious threat of partial flow blockage. The potential for damage initiated by a loose part is not necessarily proportional to the impact energy of the loose part. For example, a small piece of flat metal plate may impart little impact energy but could restrict local flow to the reactor core. However, there are technical difficulties in trying to distinguish very low-energy impact signals from the normal reactor acoustic background noise.

Sensor

Sensors of some type must be used to measure
vibration. Proper choice is important, though there is
some overlapping in frequency response. The range of
frequencies over which the response of the sensor is
linear or at least predictable is different for each type
of sensor. The more practical vibration sensors used with
machinery and structures are distance or gap measure,
velocity, and acceleration.[3] Present-day loose-part
monitoring systems (LPMS) (or metal-impact monitoring
system, as it is sometimes called) would detect and signal
the presence of an unexplained impact inside a pressure
vessel by continuously monitoring the sonic outputs (their
levels and other characteristics) from sensors installed
at a number of locations on the external surface of a
reactor vessel. Acceleration sensors are the most widely
used sensors. These sensors are usually radiation and
temperature-hardened accelerometers of the piezoelectric
type, although acoustic emission sensors (basically, high
frequency accelerometers) have also been employed in a
few developmental systems.

Identification of a Loose Part

The metal-to-metal impact causes the initiation of
an impact wave on the surface of the metallic structure.
Depending on the size of the loose part and force of

impact, the elastic wave patterns vary in their amplitude,
wave frequency structure, and duration. A loose part
(detached and drifting), which impacts many times is
often easier to locate than a loose part which impacts a
few times and is never heard from again. Also, it is
best to be able to observe that the impacts are not all
occurring at the same place because this may give
information to estimate where the part began its journey,
and helps in reducing the number of possible identities.

Operating Experience with LPMS's

Loose part monitoring systems have been developed
to provide a means for early detection of loose parts or
other sources of unusual noise and vibration in the
reactor coolant system. These systems are based on signals
detected by piezoelectric accelerometers mounted on the
exterior of primary system components and piping. The
sensors provide a direct response to the structural
vibrations and detect the acoustic noise at each location.
Loose part monitoring is accomplished by threshold
detectors which trigger when the noise signal exceeds set
criteria. In order to realize the benefits of early
detection, loose part monitoring systems must function
reliably over a wide range of plant operating conditions.
This requires a combination of adequate sensitivity and
false alarm rejection for various steady state and

transient background noise conditions. It is also desirable for loose part monitors to provide sufficient diagnostic capability to be able to locate and evaluate loose parts and other noises on-line.

Although loose-part monitoring systems have success-fully detected impacting parts in a number of operating reactors, a 1976 letter survey of licensees conducted by the U.S. NRC Division of Operating Reactors produced a wide range of both positive and negative replies to questions regarding operational experience with these systems. Some installations had reportedly been able to use their LPMS's effectively, but many complained of recurrent false alarms.

The best source of information for loose-parts origins are the results from the vessel internals vibration test. This test demonstrates the flow-induced vibration for the following systems: a) reactor recirculation systems, b) residual heat removal system, c) high pressure core spray system, d) low pressure core spray system, and e) reactor core isolation cooling system.

Examples of Successful Loose-Parts Detection

Nebraska Public Power District found three channels which had, in fact, fractured and were missing pieces in their Cooper (BWR type) reactor. The fracturing was related to vibration by the flow of the coolant[5].

The pieces were all recovered with the exception of one, which is a piece of fuel channel approximately one inch by one-and-half inches, 80 mill thick. An evaluation was conducted at the time to determine whether or not it could, in fact, create any problems; the evaluation determined that it could not, and they have not heard from it again.

The other instance of a loose part which has occurred in Cooper Nuclear Power Station (BWR) system was a sample probe which was located in the feedwater system.[6] It was used during the pre-operational testing phase for determination of water quality, and when the plant went into operation in early 1974 the probe was left in place, but it was capped off and was found during the conduct of surveillance procedure. Another instance was when the repair bridge was removed from the core and being disassembled. They discovered that a spring clip (approximately three-quarters of an inch in diameter) was missing from one of the switches on the underside of the bridge. An extensive search was conducted, but it could not be located. Therefore, it was presumed to have dropped into the core.

In another domestic Boiling Water Reactor-Mark 3 (BWR/3), it was noted that the eye of the west sparger bracket pin on the north feedwater sparger was missing during cleaning the walls of the reactor vessel. A sub-

sequent search of the vessel located part of the eye on the vessel shroud support plate. The other portion of the eye was not recovered.

During a scheduled spring, 1974, refueling and main-tenance outage at another BWR-3, a routine inspection of the internals revealed failure of certain restrainer gate components on three of 20 reactor jet pumps.

Over the years, miscellaneous small parts, tools, clothing, and other items, have been discovered at some BWR's during normal refueling outages.

Thesis Problem

In May, 1982, Gulf States Utilities expressed an interest in providing information and other support for an independent evaluation of the general problem of loose-parts monitoring in a reactor of the type scheduled for installation at the River Bend electric generating plant. This is a Mark 6 boiling water system manufactured by General Electric, generally designated as a BWR/6, which was released in 1972.

The project suggested by GSU can be divided into seven general objectives:

1. To examine the BWR/6 for probable origins of loose parts,

2. To follow the paths of potential loose parts
    within the reactor vessel,

3. To analyze the probability of coolant flow
    blockage,

4. To determine an appropriate procedure to assess
    the probability of component failure from low
    velocity loose parts impact,

5. To characterize sensor and sensing techniques
    for loose parts monitoring,

6. To verify impact-location procedures in a
    simulated boiling environment at atmospheric
    pressure, and

7. On the basis of information developed, to
    recommend a specific sensing procedure and
    analytical procedure for loose parts monitoring
    in the BWR/6.

Information was known to be available for objectives 1
and 3, therefore they were not examined in this thesis.
General information was also known to be available from
previous work on objective 5. Review of the previous
work was necessary, however, and has been included in
this thesis. To the author's knowledge item 2 has not
been examined previously for boiling water reactors.
Also, it was known that a LPMS was planned for install-
ation at River Bend, but details of the system and

and developmental analyses were not available. This thesis therefore was undertaken to accomplish the seven stated objectives, with emphasis particularly on developing new information for objectives 2, 4, and 6, augmenting information for objective 5, and finally making recommendations for objective 7.

Chapter 2

BWR/6 REACTOR ASSEMBLY[7]

The major internal structures in BWR/6 are illustrated in Figure 2.1. The principal components of the reactor vessel internals are the vessel and its internal components of the core, shroud, top guide assembly, core plate assembly, shroud head, steam separator, dryer assemblies, and jet pumps. Also included in the reactor assembly are the in-core neutron flux monitors, control rods, control rod drive (CRD) housings, and the CRDs. However due to the importance of these components, they are considered separately in later sections.

Most of the fuel assemblies that make up the core rest on orificed fuel supports mounted on top of the control rod guide tubes. Each guide tube with its fuel support piece, bears the weight of four assemblies and is supported by a CRD penetration nozzle in the bottom head of the reactor vessel. The core plate provides lateral guidance at the top of each control rod guide tube. The remaining fuel assemblies, located at the periphery of the core are supported by orificed

10

VENT AND HEAD SPRAY

STEAM OUTLET

CORE SPRAY INLET

LOW PRESSURE COOLANT
INJECTION INLET

CORE SPRAY SPARGER

JET PUMP ASSEMBLY

FUEL ASSEMBLIES

JET PUMP/RECIRCULATION
WATER INLET

VESSEL SUPPORT SKIRT

CONTROL ROD DRIVES

IN-CORE FLUX MONITOR

STEAM DRYER LIFTING LUG

STEAM DRYER
ASSEMBLY

STEAM SEPARATOR
ASSEMBLY

FEEDWATER INLET

FEEDWATER SPARGER

CORE SPRAY LINE

TOP GUIDE

CORE SHROUD

CONTROL BLADE

CORE PLATE

RECIRCULATION
WATER OUTLET

SHIELD WALL

CONTROL ROD DRIVE
HYDRAULIC LINES

Fig. 2.|. Reactor assembly (BWR/6)
(Per GE[8])

fuel supports that are welded to the core plate to pro-
vide both vertical and lateral support at the lower end
of the fuel. The top guide provides lateral support for
the top of each fuel assembly.

Control rods occupy alternate spaces between fuel
assemblies and can be withdrawn into the guide tubes
below the core during plant operation. The rods are
coupled to CRDs mounted within housings that are welded
to the bottom head of the reactor vessel.

Reactor Vessel

The reactor vessel is a pressure vessel with a single
full-diameter removable head. The base material of the
vessel is low-alloy steel that is clad on the interior,
except for the top head and nozzles, with stainless-steel
weld overlay to provide corrosion resistance.

The vessel head closure seal consists of two
concentric metal O-rings. To monitor seal integrity, a
leak detection system is provided.

Vessel supports, internal supports, their attachments,
and adjacent shell sections are designed to take maximum
combined loads, including CRD reactions, earthquake loads,
and pipe break reaction thrusts. The vessel is mounted
on a supporting skirt that is bolted to a concrete and
steel cylindrical vessel pedestal, which is integral with
the reactor building foundation.

Core Shroud

The core shroud is a cylindrical, stainless-steel structure that surrounds the core and provides a barrier to separate the upward flow through the core from the downward flow in the annulus. A flange at the top of the shroud mates with a flange on the top guide which, in turn, mates with a flange on the shroud head and steam separator assembly to form the core outlet plenum. The jet pump diffusers penetrate the peripheral shelf of the shroud support below the core elevation to introduce the coolant into the inlet plenum. The peripheral shelf of the shroud support is welded to the vessel wall to prevent the jet pump outlet flow from bypassing the core and to form a chamber around the core that can be reflooded in the event of a loss-of-coolant accident (LOCA). The shroud support is designed to carry the weight of the shroud, the steam separators, the jet pump system, and the seismic and pressure loads both in normal and abnormal conditions of operation.

Two ring spargers, one for low-pressure core spray and the other for high-pressure core spray are mounted inside the core shroud in the space between the top of the core and the steam separator base. The core spray ring spargers are provided with spray nozzles for the injection of cooling water. The core spray spargers and nozzles

have been designed not to interfere with the installation or removal of fuel from the core.

Shroud Head and Steam Separator Assembly

The shroud head and steam separator assembly consists of a domed base on top of which is welded an array of standpipes with a three-stage steam separator located at the top of each standpipe. The shroud head and steam separator assembly rests on the top flange of the top guide grid and forms the cover of the core outlet plenum region. The fixed axial flow-type steam separators have no moving parts and are made of stainless steel.

In each separator, the steam-water mixture rising through the standpipe impinges on vanes that give the mixture a spin to establish a vortex such that the centrifugal forces separate the water from the steam in each of three stages. Steam leaves the separator at the top and passes into the wet steam plenum below the dryer. The separated water exits from the lower end of each stage of the separator and enters the pool that surrounds the standpipes to join the downcomer annulus flow. An internal steam separator is shown schematically in Figure 2.2.

Steam Dryer Assembly

The steam dryer assembly is mounted in the reactor vessel above the shroud head and steam separator assembly

Fig. 2.3. Steam dryer
(Per GE[6])
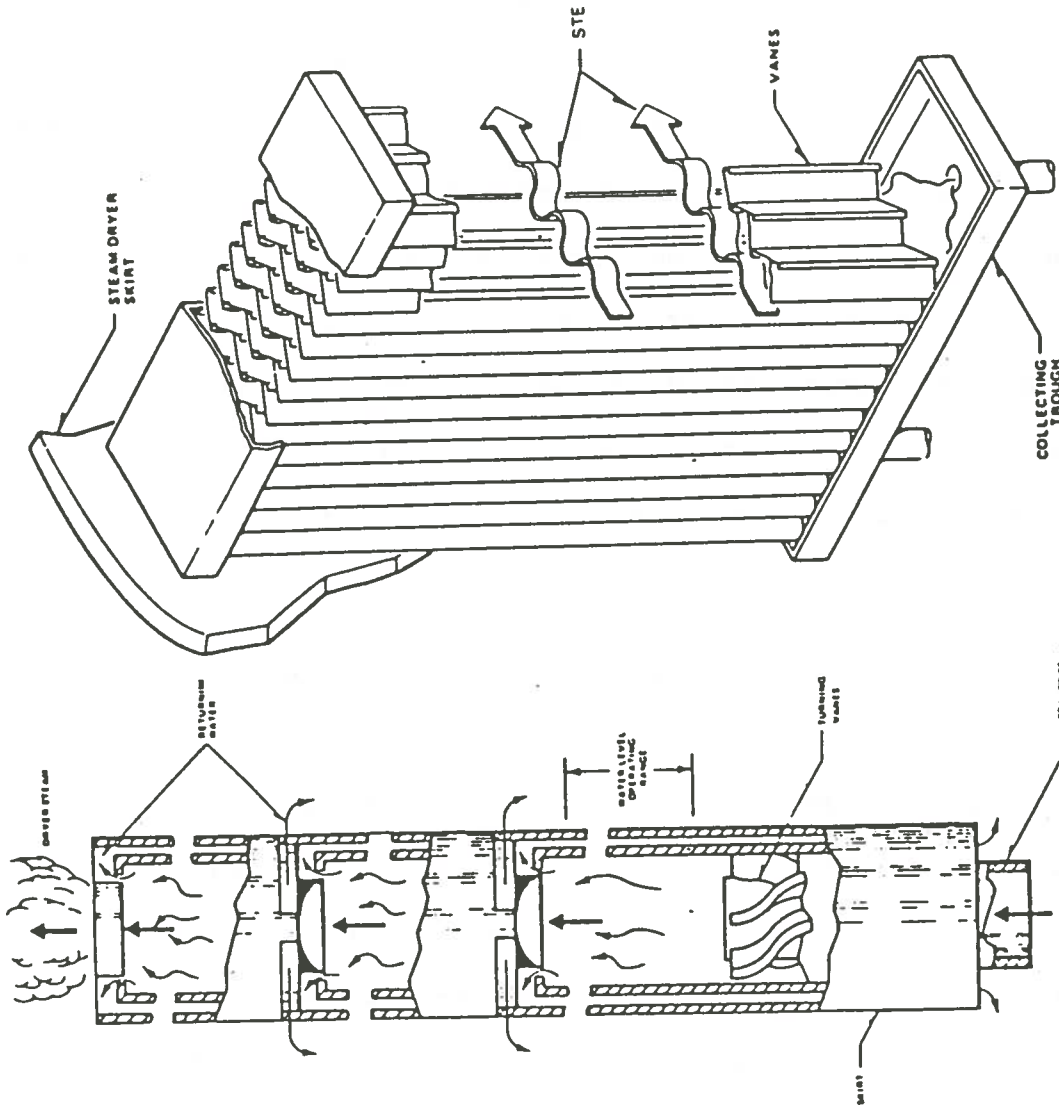
Fig. 2.2 Internal steam separator
(Per GE[8])

and forms the top and sides of the wet steam plenum. Vertical guides on the inside of the vessel provide alignment for the dryer assembly during installation. The dryer assembly is supported by brackets extending inward from the vessel wall. There are brackets attached to the vessel head, which would limit upward motion of the dryer assembly during seismic or pipe break conditions. Steam from the separators flows upward and outward through the chevron-type drying vanes. These vanes are attached to a top and bottom supporting member forming a rigid, integral unit. Moisture is removed and carried by a system of troughs and drains to the pool surrounding the separators and then into the recirculation downcomer annulus between the core shroud and reactor vessel wall. Figure 2.3 shows a typical steam dryer panel.

Reactor Water Recirculation System

The function of the reactor water recirculation system is to circulate the required coolant through the reactor core. The system consists of two loops external to the reactor vessel, each containing a pump with a directly coupled water-cooled motor, a flow control valve, two shutoff valves, and a bypass valve.

High-performance jet pumps located within the reactor vessel are used in the BWR/6 recirculation system. The jet pumps, which have no moving parts, provide a continuous

internal circulation path for a major portion of the core coolant flow.

Jet Pump Recirculation System

The jet pump recirculation system provides forced circulation flow through BWR cores. As shown in Figure 2.4, the recirculation pumps take suction from the downward flow in the annulus between the core shroud and the vessel wall. Approximately one third of the core flow is taken from the vessel through two recirculation suction nozzles. There, it is pumped to a higher pressure, distributed through a mainifold to which a number of riser pipes are connected, and returned to the vessel inlet nozzles. This flow is discharged from the jet pump nozzle into the initial stage of the jet pump throat where, due to momentum exchange, it induces the surrounding water in the downcomer region to be drawn into the jet pump throat where these two flows mix and flow through the diffuser, into the lower plenum of the reactor pressure vessel.

The jet pump diffusers are welded into openings in the core shroud support shelf, which forms a barrier between the lower plenum and the annular downcomer region where the jet pumps are located. The flow of water from the jet pumps enters the lower plenum, flows between the CRD guide tubes, and enters into the fuel support where the flow is individually directed to each fuel bundle
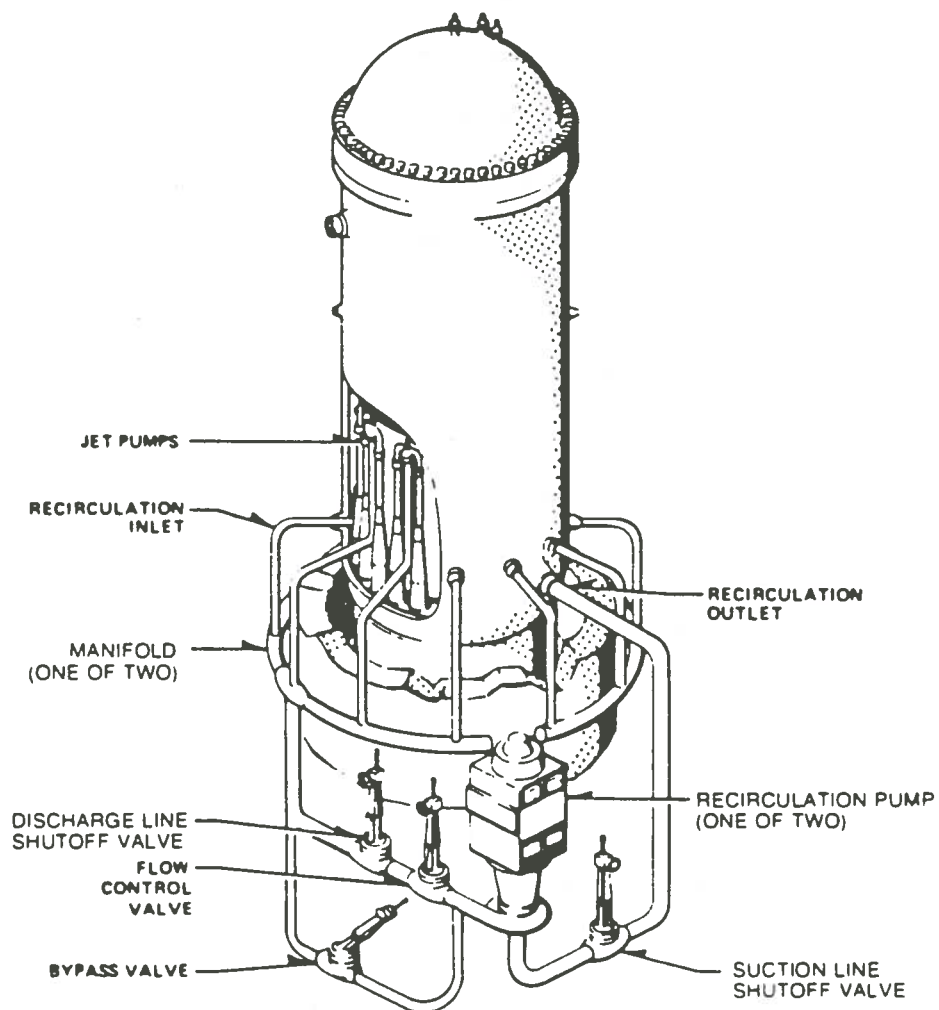
Fig. 2.4. The BWR vessel arrangement for jet pump
recirculation system.
(Per Lahey[7])

through the nose piece. Orifices in each fuel support piece provide the desired flow distribution among the fuel assemblies. The coolant water passes along the individual fuel rods inside the fuel channel where it boils and becomes a two-phase steam-water mixture. The steam-water mixture enters a plenum located directly above the core and bounded by the separator dome, which opens to the separator array of fixed steam separators. As discussed previously, the steam is separated from the water and passes through a dryer where any remaining water is removed. The saturated steam leaves the vessel though steam line nozzles located near the top of the vessel body and is piped to the turbine. Water collected in the support tray of the dryer is routed through drain lines, joins the water leaving the separators, and flows downward in the annulus between the core shroud and the vessel wall. Feedwater is added to the system through spargers located above the annulus and joins the downward flow of water. A portion (about two thirds) of this downward flow enters the jet pumps and the remainder exists from the vessel as recirculation flow.

As shown in Figure 2.5, each jet pump assembly is composed of two jet pumps and contains no moving parts. Each BWR/6 jet pump consists of an inlet mixer, a nozzle assembly with five discharge nozzles, and a diffuser.
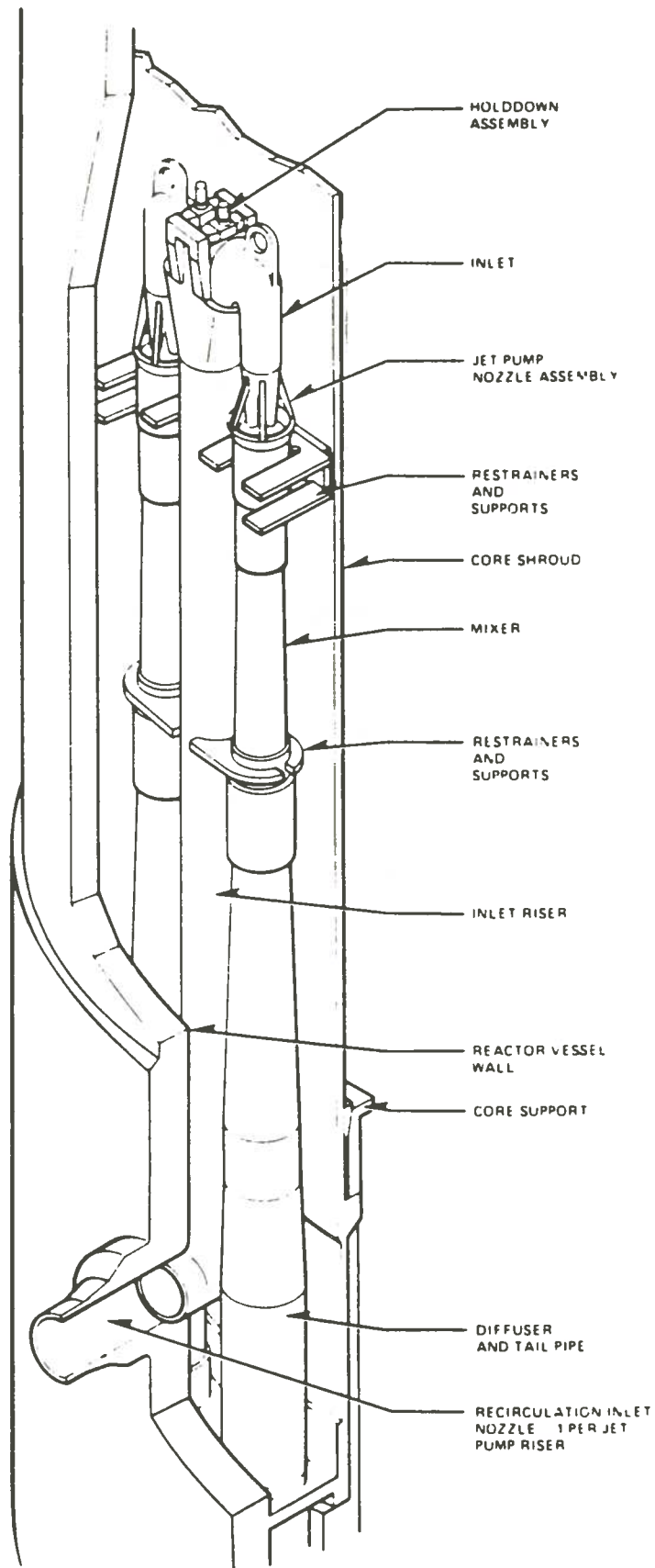
Fig. 2.5. Jet pump assembly.(Per GE[8])

The inlet mixer assembly is a constant diameter section of pipe with a diffuser entrance section at the lower end and the drive nozzle at the upper end.

The jet pump diffuser is a gradual conical section terminating in a straight cylindrical section at the lower end, which is welded into the shrouded support.

The overall length of the jet pumps is 19 ft. Each pair of jet pumps is supplied driving flow from a single riser pipe. These risers have individual vessel penetrations and receive flow from one of two external manifolds. Driving flow to each distribution manifold is furnished by its associated centrifugal pump. The recirculation system includes 20 jet pumps.

Chapter 3

LOOSE-PARTS INDUCED FLOW BLOCKAGE

Background: Review of Actual Flow Blockage
Accidents in the Nuclear Industry

A flow blockage accident is very unlikely, but some
flow blockage accidents have indeed occurred in operating
reactors. The occurrence of these incidents clearly
indicates that flow blockages by foreign objects are
within the realm of possibility. The following subsection
reviews the actual blockage accidents which have occurred
in water-moderated, water-cooled reactors to relate to a
BWR. In particular, flow blockage accidents at the
Material Test Reactor (MTR) and Engineering Test Reactor
(ETR) at the National Reactor Testing Station (now the
Idaho National Engineering Laboratory) will be reviewed.

Flow Blockage in the MTR[10]

On November 13, 1962, a piece of dislodged gasket
material from the MTR primary coolant system caused a
significant flow restriction in at least two flow channels
of a standard MTR fuel element. A visual examination of
this material in the fuel assembly indicated that it was
black rubber with an asbestos or fiber glass binder. The
gasket material caused a flow reduction of approximately
30%. The accident was immediately detected by in-core

22

instrumentation and an increase in radiation levels around the reactor proper and in the process water building. The damage was found to consist of one fuel plate which had partially melted, resulting in the loss of approximately 10.5 grams of metal alloy fuel containing an estimated 0.7 gram of fissionable material.

Flow Blockage in the ETR[11]

On December 12, 1961, the Engineering Test Reactor experienced fission breaks in six fuel elements as a result of a flow blockage in one quadrant of the core. Eighteen separate fuel plates, distributed among six fuel elements, were found to have melted in varying degrees. Approximately 12.4 grams of U-235 contained in 134 grams of alloy were lost. Examination of the core after shutdown revealed the cause of these fission breaks to be the presence of considerable amounts of foreign materials blocking off coolant to several fuel elements. The material was identified as lucite from a sight box which had escaped detection during prestartup inspection and checks. Hydraulic and thermal analysis after the accident revealed that the normal flow through the damaged fuel assemblies was reduced by 65%.

Geometrical Configuration of a Fuel Bundle

Before discussing loose parts restricting the flow
of coolant to a fuel assembly, it is first necessary to
describe the geometrical configuration of a fuel bundle.
This will indicate the most probable blockage location and
the degree of difficulty involved in blocking the coolant
flow path. Coolant to the flow channels is provided by
two recirculation pumps which circulate water via a jet
pump system. The flow exits from the jet pump diffuser
and enters the lower plenum which contains a forest of
control rod guide tubes. These tubes, approximately 10.9
inches in diameter, are spaced on a 12-inch pitch. The
guide tubes support four individual fuel assemblies,
except for the guide tubes on the periphery of the core,
which support only one assembly. The configuration is
depicted in Figure 3.1. The flow from the lower plenum
enters the fuel channel through an orifice located in
the support piece. This orifice is typically 1.5 to 2.5
inches in diameter. The fuel assembly which rests on the
support piece consists of a fuel bundle and a channel
which surrounds it as shown in Figure 3.2. The fuel bundle
itself contains 62 fuel rods and 2 water rods which are
spaced and supported in a square 8 x 8 array by the lower
and upper tie plates. The lower tie plate has a nosepiece
which fits into fuel support piece and distributes coolant

FUEL ASSEMBLY

LOWER TIE PLATE HOLES

FUEL SUPPORT PIECE

CORE SUPPORT ASSEMBLY

ORIFICE

CONTROL ROD GUIDE TUBE

FLOW

FLOW

PERIPHERAL BUNDLE

FOUR-LOBED (ONE LOBE SHOWN)
NORMAL BUNDLE
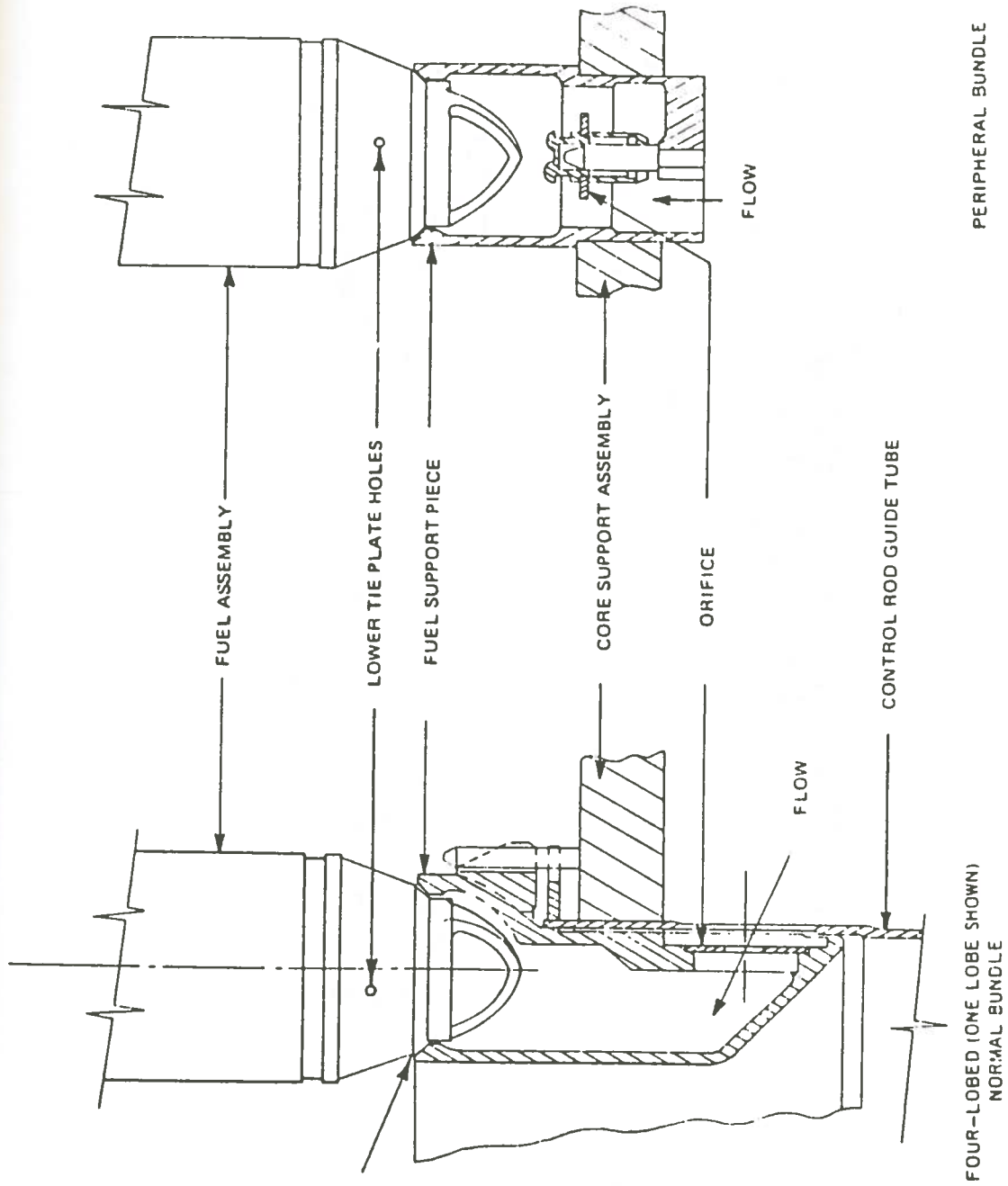
Fig. 3.1. Fuel support pieces
(per GE NEDO-10174[9])

BAIL HANDLE

UPPER TIE PLATE

FUEL BUNDLE

FUEL ROD INTERIM SPACER

FINGER SPRING (TYPICAL OF 4)

CHANNEL FASTENER ASSEMBLY

UPPER TIE PLATE

FUEL CLADDING

FUEL CLADDING

EXPANSION SPRING

FUEL CHANNEL

PLENUM SPRING

LOWER TIE PLATE

NOSEPIECE

FUEL PELLET
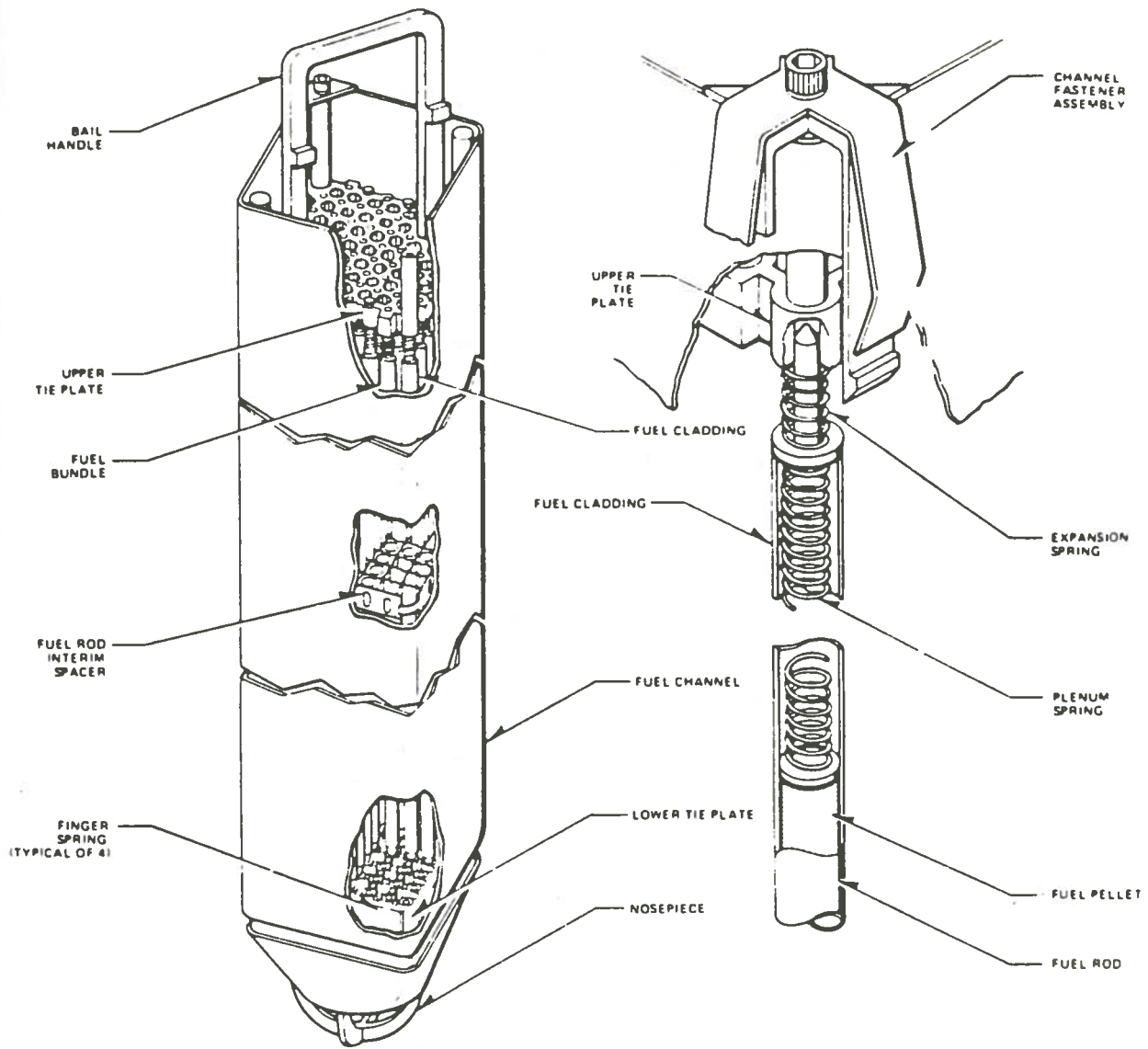
FUEL ROD

Fig. 3.2. Fuel assembly
(Per GE NEDO-10174[9])

flow from the fuel support piece to the fuel rods. Both tie plates are fabricated from Type-304 stainless steel.

Three types of rods are used in the bundle: tie rods, water rods, and standard rods. The third and sixth rod along each outer edge of a bundle are tie rods. The eight tie rods in each bundle have threaded end plugs which thread into the low tie plate casting and external through the upper tie plate casting. Two central rods in each fuel bundle are water rods, one of which is used to position seven zircoloy-4 fuel rod spacers vertically in the bundle. The standard rods are 0.483 inches in diameter located on a typical pitch of 0.640 inches.

Flow Blockage

One of the most obvious ways in which coolant flow could be restricted is for some foreign object to become lodged in the flow path of a channel. This can occur only in certain locations: the orifice could become partially restricted, an object could become lodged between the fuel support piece and the lower tie plate nosepiece or an object could enter the fuel bundle and become lodged between the fuel rods. This latter type of blockage is of less consequence than the former two because any one single object cannot restrict enough flow to pose a serious threat to the integrity of bundle. The reason for this is the

maximum size of an object capable of getting through the lower tie plate is only 0.410 inch (0.132 in.^{2}) in diameter (this is the size of the hole provided in the tie plate for flow distribution) compared to a total flow area of 15.82 in.^{2}. It would take a great many objects to block the flow area significantly to cause concern. This subject is discussed in more detail below. The other two locations, the orifice and the lower tie plate nosepiece, offer a more probable location in which objects can become lodged and cause a more significant reduction in flow.

As standard practice, great care is taken to remove and prevent any objects from entering the reactor system through strictly controlled operating and startup procedures. However, there does exist the possibility, remote as it may seem, that some object could either escape detection or break loose from the vessel internals. Such an object would have to make its way into the lower plenum through the jet pumps that have a typical nozzle diameter of 1.3 inches in diameter. The throat diameter of a jet pump is 6.5 inches for BWR/6 product lines. Once the object enters the lower plenum (if it was not there to begin with), it has to proceed along the tortuous path through the guide tubes before reaching the channel inlet. The guide tubes leave a minimum gap of 1.125 inches and a maximum gap of 6.096 inches between guide tubes, as shown in Figure 3.3.
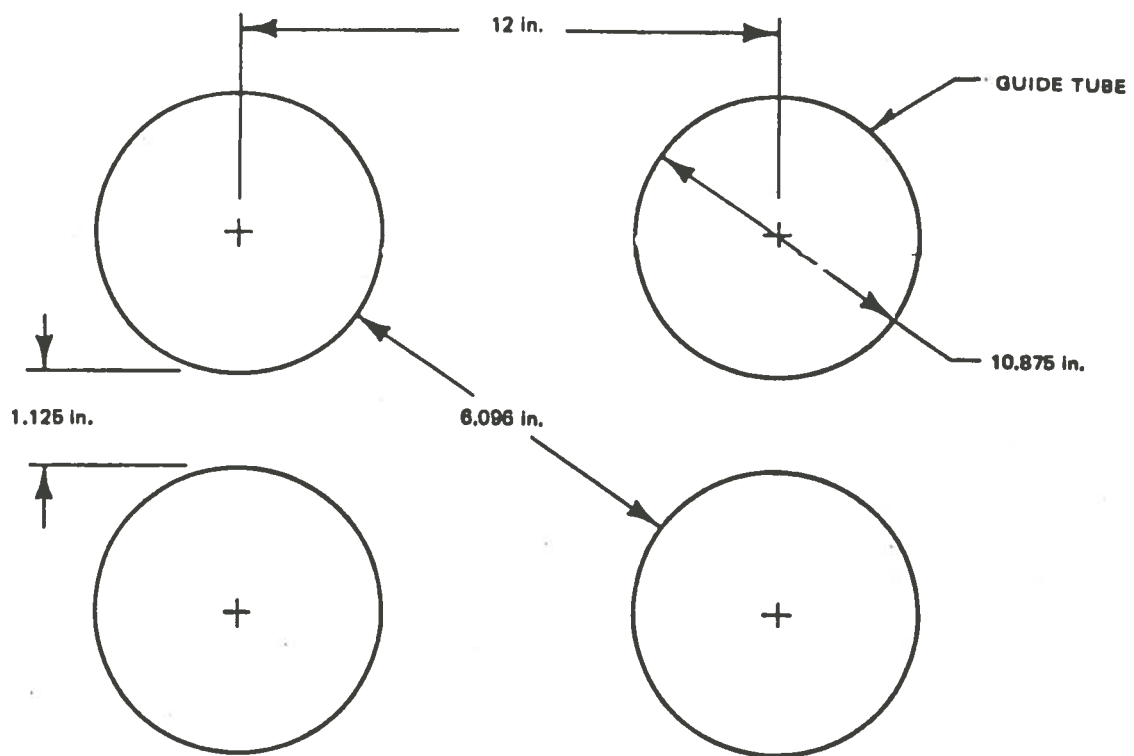
Fig. 3.3. Guide tube geometry
(Per GE[8])

If the object is initially in the lower plenum it will be resting on the bottom of the vessel, or if it is brought in through the jet pumps the high downward velocity component will tend to keep it on the bottom. The factor that will determine whether the object will be swept up off the bottom is dependent on the radial component of the velocity. Calculations of the average vertical and radial velocity components were made for typical plants at rated flow. These are given in Table 3.1 for a symmetrical wedge representing 1/8 of the guide tube field as shown in Figure 3.4.

The maximum radial velocity is that which occurs in the 1.125 inch gap between guide tubes, whereas the minimum is that which occurs between rows. As can be seen, as the flow proceeds toward the center of the core the coolant has very little radial velocity and for all practical purposes is flowing vertically.[12]

Figures 3.5 and 3.6 show the terminal velocity for sideways motion of cylindrical and flat-plate-type objects in water at 1000 psia and 520°F. If the vertical fluid velocity is greater than the terminal velocity, the object may be lifted by the drag forces from the fluid. Thus it is seen that most objects of reasonable size are capable of being swept up off the bottom of the vessel by the radial component and up toward the core by the vertical component.

Table 3.1

LOWER PLENUM VELOCITY COMPONENTS

	Average Radial Component (fps)		Average Vertical
Row	Maximum	Minimum	Component (fps)
I	7	<1	6
II	6	<1 ·	10
III	5	.	.
IV	.	.	.
.	.	.	.
.	.	.	.
VII	<1	<1	10

SYMMETRICAL WEDGE

ROW

RESTRICTION NO.

CIRCUMFERENTIAL RING APPROXIMATION
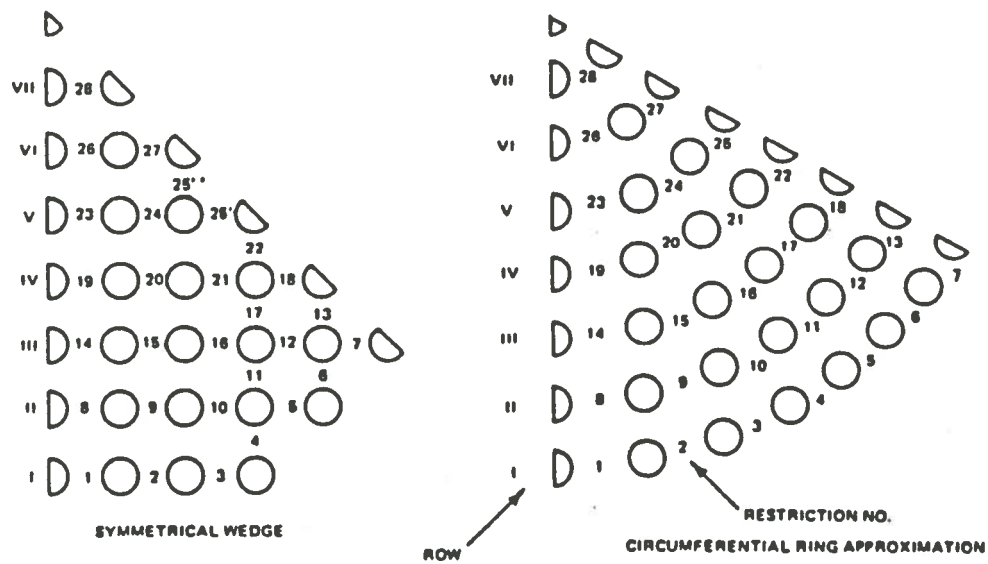
Fig. 3.4. Geometrical approximation for control rod guide
tube field.
(Per GE NEDO-10174[9])
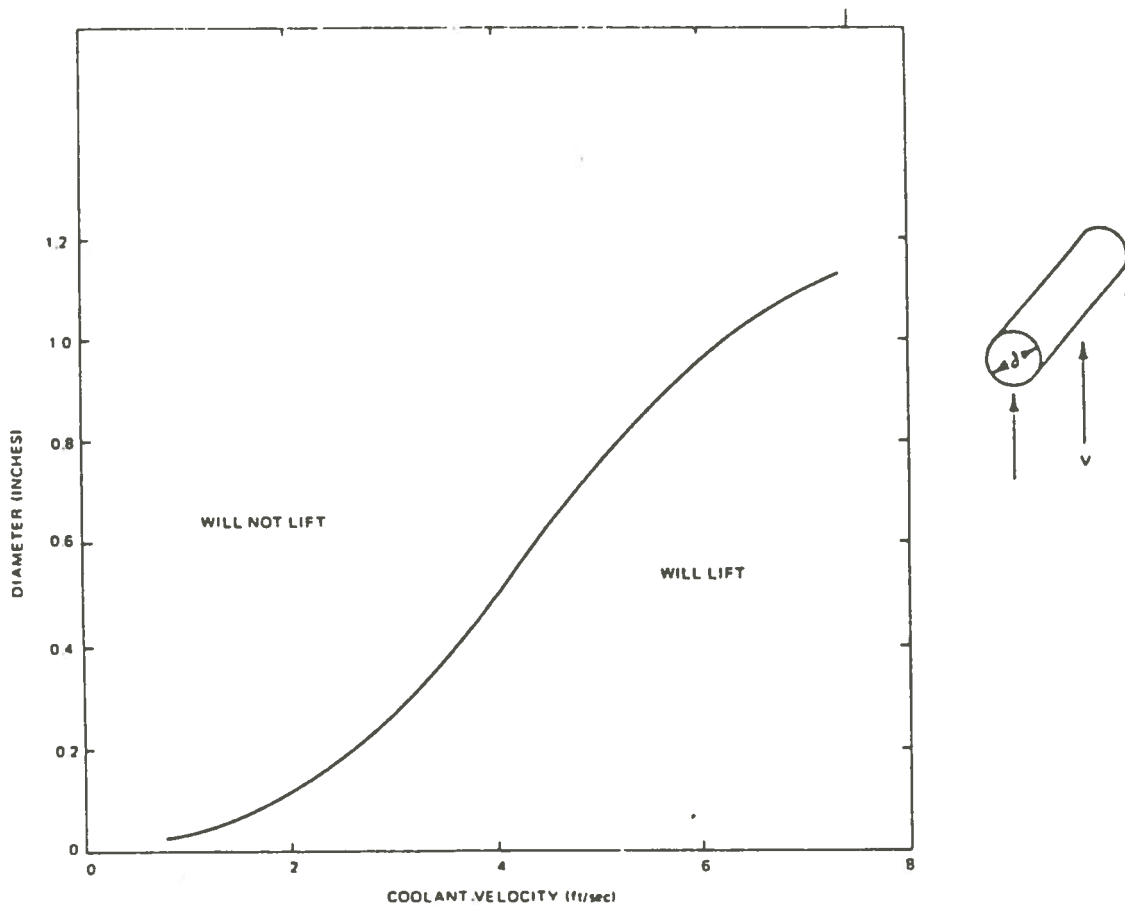
Fig. 3.5. Criteria for lift of a cylindrical steel rod
(Per GE NEDO-10174[9])
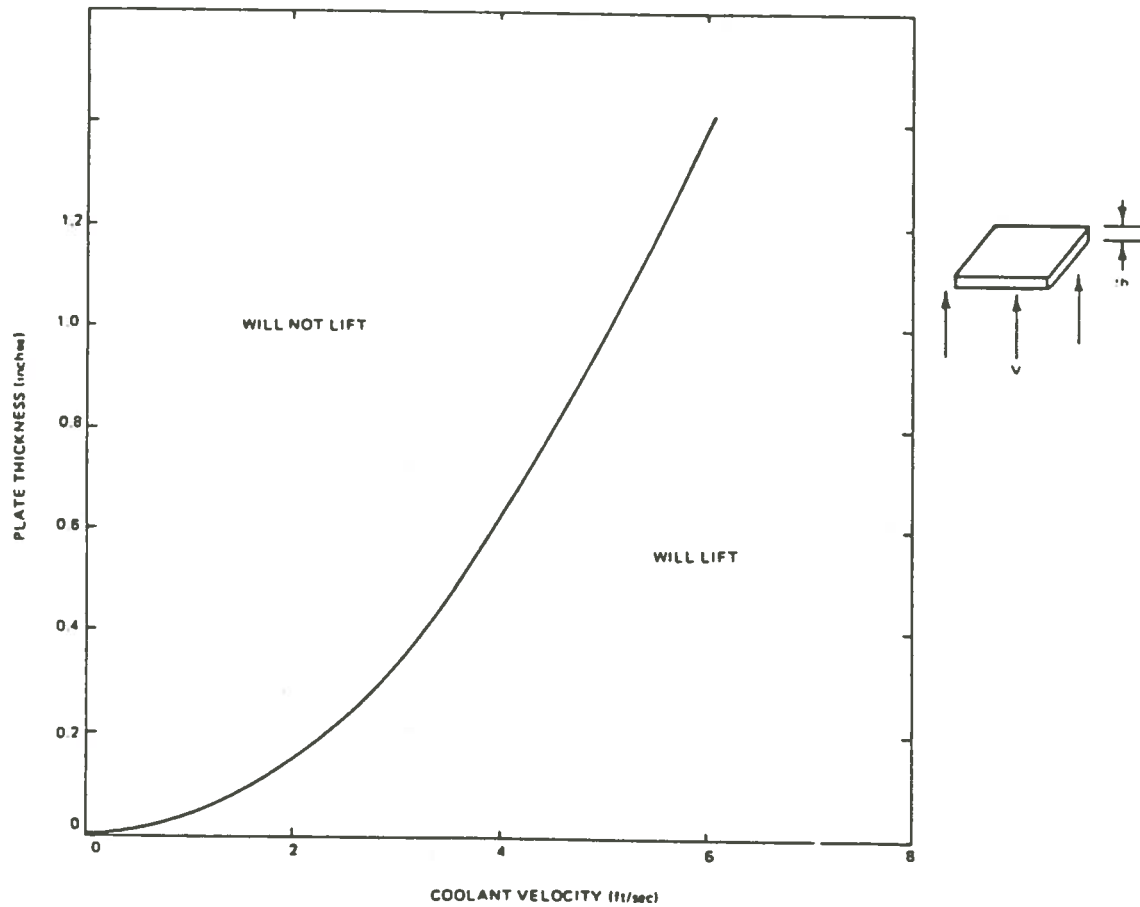
Fig. 3.6. Criteria for lift of a flat steel plate
(Per GE NEDO-10174[9])

However, while it is possible for certain sizes for objects to be swept upward toward the bundle entrance, the following factors tend to reduce this possibility:

a. There are very few locations where the radial velocity would be high enough to sweep the piece off the floor of the narrow 1.125 inch gap between guide tubes.

b. If an object fell to the bottom of the vessel, it would tend to drift toward the vessel centerline where horizontal velocities are low and the boundary layers on the vessel may be thicker than the object. Thus, the boundary-layer effect would reduce the capability of the fluid to sweep the piece up off the floor of the vessel so that the vertical components could carry it upward.

c. Even if the object were somehow swept upward, it seems unlikely that it could completely block the orifice holes, which are vertically oriented.

d. If the object were small enough to pass through the orifice, it would have to pass through the lower tie plate nosepiece and the lower tie plate to enter into the fuel channel, which would require very unlikely alignment of the

object and the passage through holes of only
0.410 inch diameter.

If the object were to make it through the lower tie plate, it would be stopped by the first spacer, which would probably cause local boiling transition and over-heating. Depending on the size and shape, the object will most likely remain in a vertical position since the maximum distance between fuel rods is only 0.422 inch. The object would not significantly reduce the flow in one bundle and cause serious degradation of the heat transfer conditions in other areas of the fuel assembly.

Therefore, even though it is possible for minor block-ages to occur by small objects entering the fuel bundle and affecting the life of the fuel, it is very unlikely that a blockage which would induce a significant flow reduction will occur. This is in part supported by the thermal shield vibration failure at Consumers Big Rock Point Reactor.[13] One-inch-diameter bolts on the thermal shield hold down assembly failed due to vibration. During the shutdown, debris was found on the bottom of the reactor vessel but there was no evidence that any had been swept up into the core.

Another possibility for flow blockage occurs during reactor fueling operations. It is remotely possible for an object to be dropped on top of the fuel support piece prior to loading a fuel bundle. Subsequently, when a fuel

bundle is loaded into this location, the object if un-
detected, could become lodged between the fuel support
piece and the bundle's lower tie plate nosepiece. This
type of blockage would, in most cases, result in improper
seating of the bundle, which represents another opportunity
for detection during the subsequent core loading verifi-
cation checks. Therefore, the opportunity for detection
is present: 1) at the time the object is dropped, 2)
during fuel loading, and 3) after fuel loading verification,
---making this an unlikely mechanism to cause a flow
blockage.

Chapter 4

CHARACTERIZATION OF SENSORS USED FOR LPMS's

Introduction

Vibrational analysis (also called Dynamic Testing) can provide detection of vibration and unbalance, and determination of severity with prediction of failure. The more practical vibration sensors used with loose part monitoring systems are the piezoelectric accelerometer and acoustic emission sensor which are also used in structural vibration monitoring. A piezoelectric material[18] has the property that when it is deformed by external mechanical pressure, electric charges are produced on its surface. This effect was discovered in 1880. The reverse phenomenon, according to which such a material, if placed between two electrodes changes its form if an electric potential is applied, was discovered soon afterwards (1881). Piezoelectric materials of either synthetic or natural crystals are used as the sensing element of accelerometers. When an accelerometer is attached to a structure, the charge produced by the piezoelectric element is proportional to the surface movement of the structure.

Technical Criteria of a Sensor[14]

Sensitivity

The sensitivity of an accelerometer is defined as the ratio of its electrical output to its mechanical input. The higher the sensitivity, the greater the system signal-to-noise ratio; also the system will be less susceptible to electrostatic and electromagnetic pickup. However the higher the sensitivity for a specific design, the greater the weight and the lower the resonance frequency. Sensitivity selection may therefore be limited by weight and frequency response constraints.

Strain Sensitivity

Strain sensitivity or base bending sensitivity is defined as the spurious output from an accelerometer caused by strains imposed in its base by the deformation of the specimen to which it is attached. In most applications, a strain may be known to exist in the specimen under an accelerometer. However, the actual magnitude of the strain may not be known. Thus, if the structure under an accelerometer is expected to bend or strain during a measurement, the accelerometer should be selected for minimum strain sensitivity.

Transverse Sensitivity

For single axis measurements, it is imperative that the accelerometer not produce any significant response to lateral motion of test objects. Because accelerometers are not mechanically perfect, they will have small sensitivity to transverse vibrations. For any piezoelectric accelerometer there exists one axis which provides maximum response for an input acceleration. The charge output along this axis for a 1 g input is Q_{max}, the maximum sensitivity. The sensitivity, Q_θ, along any other axis (inclined at an angle θ from the axis of Q_{max}) is $Q_{max} \cos\theta$. In a perfect transducer, the vertical axis (y axis in Figure 4.1) and the axis of Q_{max} would coincide. These transducers characteristically exhibit a basic sensitivity of $Q_\theta = Q_{max} \cos\theta$ and a (maximum) transverse output $Q_T = Q_X = Q_{max} \sin\theta$. Transverse sensitivity is expressed as a percentage of the basic sensitivity and, thus, is defined as:

$$\frac{Q_T}{Q_\theta} \times 100 = \tan\theta \times 100\%$$

For motion in the transverse (XZ) plane along any other axis (inclined at an angle ϕ from the X axis) the transverse sensitivity is $Q_t = Q_T \cos\phi$. Thus, a more general expression becomes: % of transverse sensitivity =

$$\frac{Q_t}{Q_\theta} \times 100 = \tan\theta \cos\phi \times 100$$
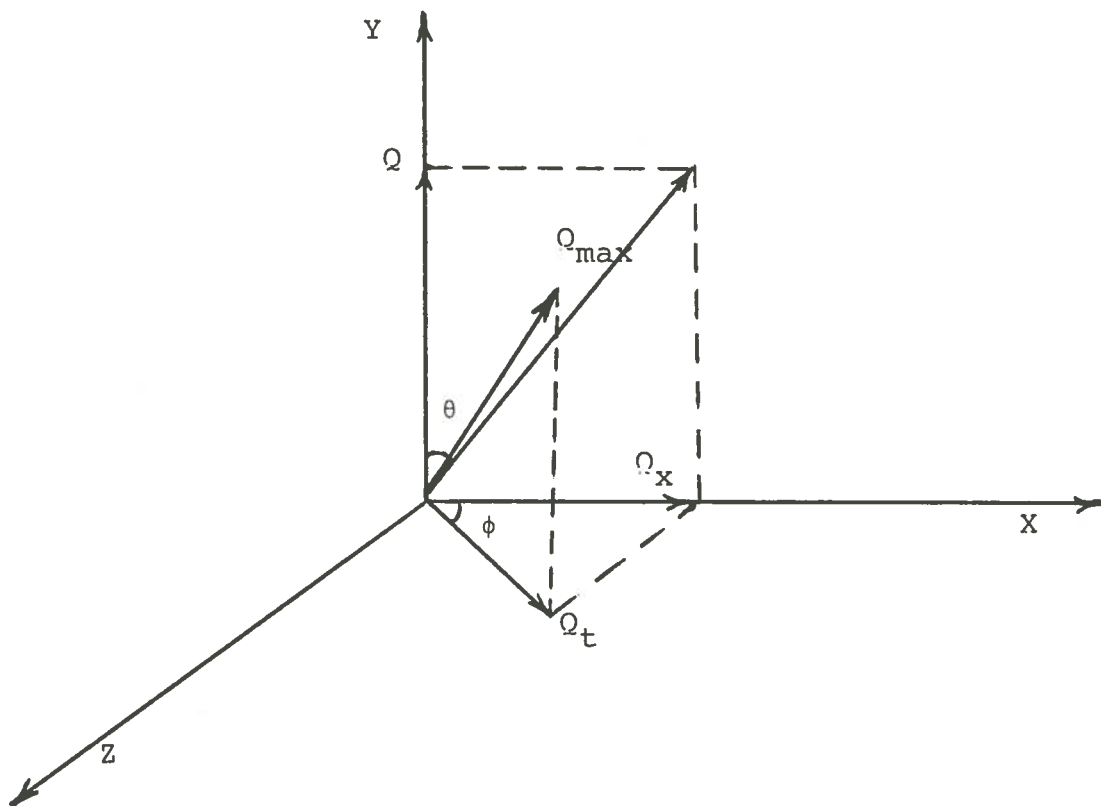
Fig.4.1. Transfer sensitivity of piezoelectric accelerometer
(Redrawn from Endevco[13])

Frequency Response

Low frequency response. A piezoelectric accelero-
meter is a self-generating transducer that produces an
electrical output signal that is proportional to acceler-
ation, without the use of an external power source or
carrier voltage. In practice, such a transducer cannot
be used to measure constant or steady-state accelerations.
At zero frequency no mechanical energy is being put into
the system, thus electrical energy cannot be continuously
removed.

When using charge amplifiers the system low frequency
response is determined primarily by the low frequency
response of the amplifier. The length of cable between
transducer and amplifier will not affect the low frequency
of the system, which is limited only by the characteristics
of the amplifier.

When using voltage amplifiers, the low frequency
response of a piezoelectric accelerometer is a function of
the RC time constant of the accelerometer and the input
resistance of the matching electronics. For instance,
the Model 2220C or other Piezite ® Element Type P-8
accelerometer, with an internal capacitance of approxi-
mately 750 pF and used with a 200 pF cable, requires a
high input resistance (100 MΩ or better) to work into a
voltage amplifier and provide satisfactory frequency
response to 5 Hz.

Of course, the low frequency response of any accelerometer can be improved by swamping with additional shunt capacitance, such as long cables, to raise the RC time constant. However, this technique will also affect sensitivity, as discussed later.

Actual response at any frequency can be measured from Figure 4.2. where:

f = frequency in Hz

R = input resistance of the matching amplifier in ohms

C = total capacitance in farads of the accelero-meter, plus additional applied shunt capacitance, if any.

If the frequency (f) of the desired measurements is 10 Hz, the total capacitance (C) of the accelerometer and cable is 500 pF, and the amplifier input impedance (R) is 100 MΩ (Endevco® cathode follower), we can determine:

$$f \times R \times C = 10 \times 100 \times 10^6 \times 500 \times 10^{-12} = 0.50$$

Using Figure 4.2, we find that the relative response corresponding to fRC = 0.5 is 95%, indicating that the signal at 10 Hz will be down approximately 5%.

High frequency response. High frequency response is a function of the mechanical characteristics of the accelerometer. Most accelerometers can be represented as

an undamped single-degree-of-freedom spring-mass system, the response of which is shown in Figure 4.3 as a function of frequency.

This curve can be considered as showing the variation in sensitivity of the transducer with frequency. The response curve shows that at 1/5 the resonance frequency, f_n, the response of the system is 1.04. This means that the sensitivity of the accelerometer is 4% higher at that frequency than at the lower frequencies. Since 5% is the maximum error that most users permit, the "flat" accelerometer frequency range should be considered limited to 1/5 the resonance frequency.

Resonance frequency. Resonance frequency is that frequency at which the sensitivity is a maximum. Several methods can be used to determine accelerometer resonance frequency. Unfortunately, they do not all give the same answer. The simplest method for an undamped spring-mass, the resonance frequency is computed using the following equation:

$$f_n = \frac{1}{2\pi} \sqrt{\frac{k}{m}}$$

To be conservative, the accelerometer should be rated with the lowest resonance frequency obtained. An accelerometer should be selected with resonance frequencies at least 5 times higher than the highest frequency of interest.
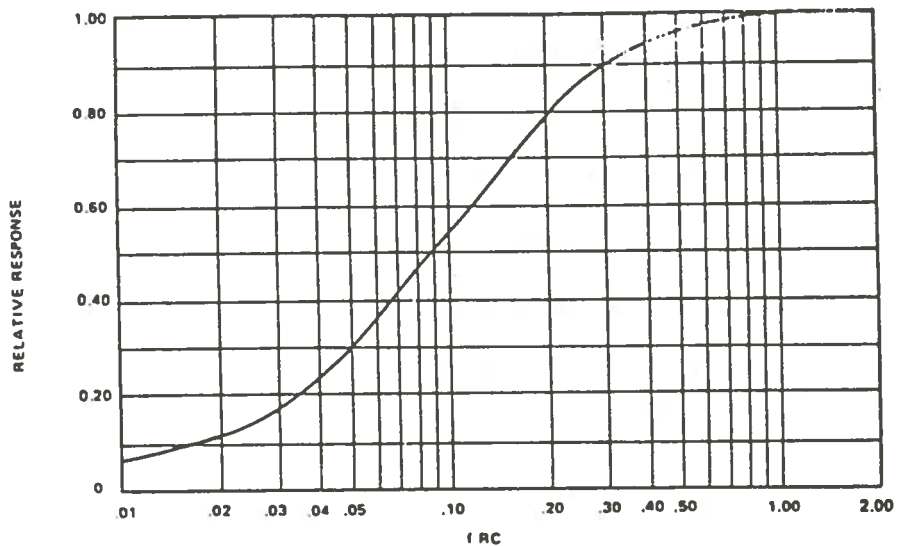
Fig. 4. 2. Low frequency response VS. loading (voltage amplifiers)
(Per Endevco[13])
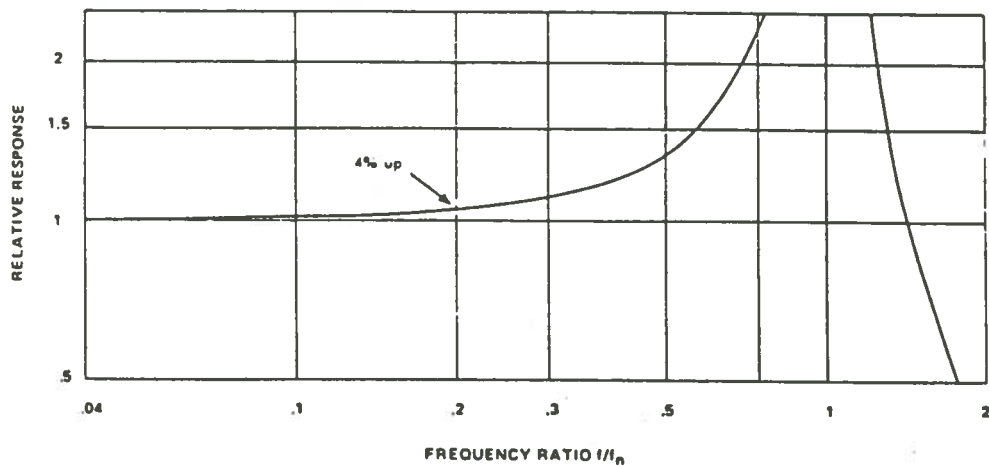
Fig. 4.3 Response of an undamped single-degree-of-freedom
spring-mass transducer when the case is undergoing
sinusoidal acceleration.
(Per Endevco[13])

Amplitude Range and Linearity

The range of input acceleration levels for which accelerometer sensitivity remains constant is defined as the range of "Amplitude Linearity". The sensitivity of most accelerometers increase with acceleration level. Accelerometers tend to have a very predictable non-linearity that can be expressed as a percentage increase in sensitivity with applied acceleration. For example, for piezoelectric accelerometer model 2273AM1, sensitivity increases approximately 1% per 1000 g.

Temperature Deviation

Some accelerometers show variations in sensitivity, capacitance, and resistance within their usable temperature range. The deviation of voltage output with temperature is almost always different from the charge output deviation. At higher temperatures, the internal resistance of an accelerometer decreases, causing a reduction in the effective RC time constant when operated into voltage amplifiers. Therefore low frequency response of the system will change. Since charge-sensing electronics can operate with lower source resistance than voltage amplifiers, charge amplifiers are recommended for use at very high temperatures. In addition some accelerometers also exhibit an electrical output which is a function of the rate of change of temperature. These outputs can be quite large and are due primarily to two

effects: 1) thermal transients may cause non-uniform stresses in the accelerometer structure which results in a changing force on the crystal element that, in turn, produce an electrical output; and 2) some accelerometers exhibit pyroelectric effect in which an electrical output occurs as a function of temperature change.

Nuclear Radiation

Accelerometers can be exposed to relatively large radiation doses without any harmful effects. Battelle Memorial Institute reports[14] that piezoelectric accelerometers have been exposed to a neutron fluence of 10^{16} n/cm^2 and to gamma radiation up to 10^{11} ergs/g. Most of the accelerometers tested operated normally without displaying any effects due to these radiation environments.

Accelerometer Sensor[15]

A accelerometer is an instrument used to measure shock and vibration. It is useful for both high and low frequencies. It can be idealized by a mass element connected to the case by a spring and a damping medium. The transducing element produces an electrical output proportional to the displacement of the mass element relative to the case and also proportional to the acceleration applied to the case. Most accelerometers can be

represented as a single-degree-of-freedom system and are sensitive only to one axis.

A simplified model of a typical accelerometer is shown in Figure 4.4 where m is the sensitive mass of the accelerometer, k is the spring constant, and c is the damping coefficient. The basic equation of motion of the mass m is given by

$$-m \frac{d^2 x_1}{dt^2} + c \left(\frac{dx_1}{dt} - \frac{dx_2}{dt}\right) + k (x_1 - x_2) = 0 \qquad (4.1)$$

The displacement of m with respect to accelerometer housing is given by

$$x = x_1 - x_2 \qquad (4.2)$$

and therefore, Eq. (4.1) becomes

$$m \frac{d^2 x}{dt^2} + c \frac{dx}{dt} + kx = -m \frac{d^2 x_2}{dt^2} \qquad (4.3)$$

Dividing both sides of Eq. (4.3) by m and redefining the constant coefficient leads to

$$\frac{d^2 x}{dt^2} + 2\xi w \frac{dx}{dt} + w^2 x = -a(t) \qquad (4.4)$$

where

w = k/m, circular natural frequency

$$\xi = c/2 \quad 1/mk, \text{ ratio of actual to critical damping}$$

$$a(t) = \frac{d^2 x_2}{dt^2}, \text{ time dependent acceleration input to the}$$
$$\text{system.}$$

The relation (4.4) is the governing equation for an accelerometer system with a(t) being the impact acceleration at the sensor location.

The sensitive element of an accelerometer (k in Figure 4.4) is a piezoelectric crystal which is in effect a capacitor that produces a charge, q, across its plates proportional to a force applied to the crystal. The actual circuit diagram of an accelerometer is shown in Figure (4.5). The internal resistance and inductance can be ignored when considering the general performance of an accelerometer.

The output voltage of the accelerometer is equal to the charge generated by the piezoelectric element divided by the transducer capacitance, or

$$E(\frac{volts}{g's}) = \frac{q-(picocoulombs/g's)}{Cp(picofarads)}$$

where 1 g rms of shake (1 g = 386.089 inch/sec^2 or 9.806 m/sec^2). The simplified equivalent circuit for both modes is shown in Figure (4.6). The shunt resistance is usually the input resistance of an associated amplifier and the external capacitance c_t is the capacitance of the cable. Since the charge generated by the transducer does
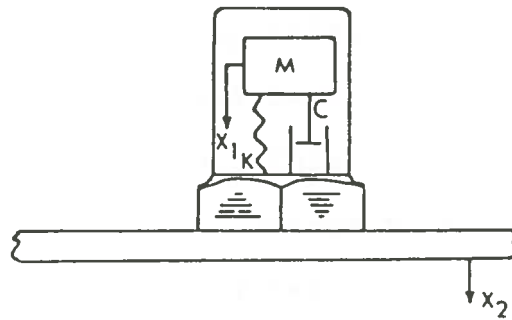
Fig. 4.4. A simplified accelerometer design
(Per Shahrakhi[15])
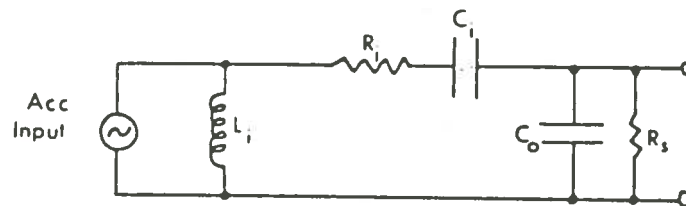
Fig. 4. 5. Circuit diagrom of a piezoelectric accelerometer
(Per Shahrakhi[15])

a. Charge Eq.

$$e = \frac{q}{C_p + C_t}$$

b. Voltage Eq
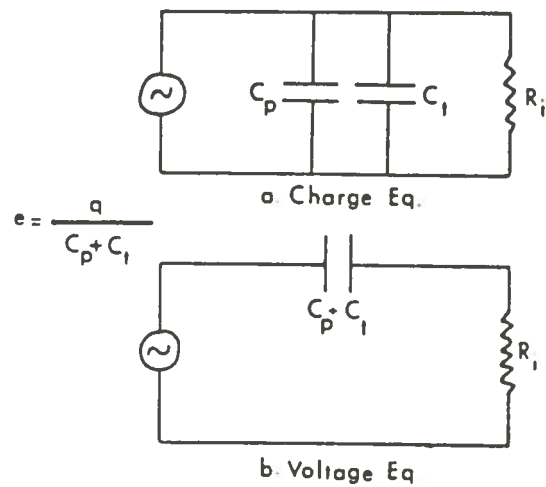
Fig. 4. 6. Equivalent circuits for piezoelectric transducer
system
(Per Shahrakhi[15])

not change as the cable capacitance (c_t, long and short cables), the charge sensitivity of the accelerometer system remains unaffected. This characteristic explains the practical advantage of charge-sensitive electronics over a voltage-sensitive system.

Each accelerometer is provided with a voltage and a charge sensitivity calibration. Charge sensitivity is measured or derived directly from $Q = EC$ but when using a voltage amplification system the factory voltage sensitivity will change according to the type and length of cable used from the transducer to the amplifier. The following two equations give the new voltage sensitivity of the system.

$$E = \frac{Q}{C_p + C_t} \times 1000$$

$$= E_{cal} \frac{C_p + C_{cal}}{C_p + C_t} \tag{4.5}$$

where

E = new sensitivity being determined, mv/g

Q = factory supplied charge sensitivity, Pe/g

C_p = transducer internal capacitance pF

C_t = total capacitance external to the transducer, pF

C_{cal} = external capacitance used when calibrated at factor, pF

E_{cal} = factor supplied voltage sensitivity, mv/g.

Acoustic Emission Transducer[16]

Several different transducers (in type or sensitivity), different electronic systems, and different measurement parameters are used for acoustic emission measurements.

Transducers are now almost always piezoelectric, and are usually undamped or lightly damped so that sensitivity is not lost. A typical design for an acoustic emission transducer is shown in Figure 4.7. The transducer will be coupled to the structure being monitored via a thin coupling layer, usually of oil or grease. The piezoelectric element is often faced by a protective shoe and may or may not be backed up by a damping material.

The acoustic emission transducer is a layered medium. The layers are identified in Figure 4.8. In trying to formulate a theory to explain the response of the acoustic emission transducer to a stress wave signal, we consider a wave travelling from left to right (Figure 4.8) and incident normally on the multilayer system. Medium 1 is usually steel or some other metal, although it may be a non-metal in certain cases. Medium 2 is the coupling layer, which may be grease, or oil, or a solid. Medium 3 will be the transducer protective shoe which is usually present. Medium 4 will be the piezoelectric material which carries out the acoustic-electric transduction
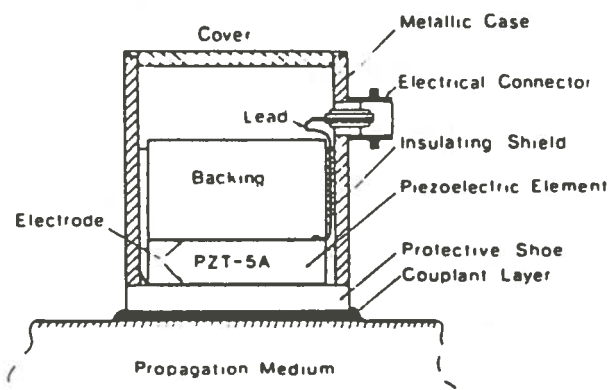
Fig. 4.7. A typical acoustic emission design
(Per Hill[16])
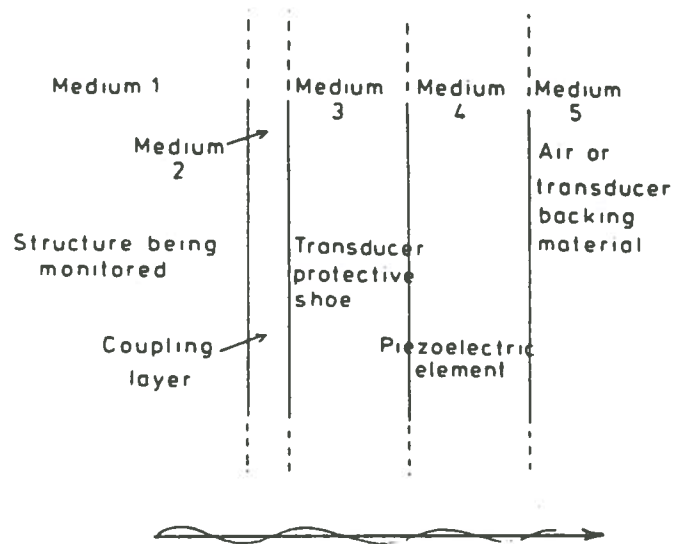
Fig. 4.8. The layers in an acoustic emission transducer
(Per Hill[16])

process. Medium 5 may be air, or a damping material
used to provide a broadband transducer. If the backing
material is effective, then any wave transmission into
medium 5 may be lost due to attenuation, or may be dealt
with by considering the theory in terms of 6 layers. If
medium 5 is air then the medium is considered infinite.
In this case the mismatch of acoustic impedance between
the piezoelectric medium 4 and air would mean that very
little signal was transmitted. In all cases, the final
medium is considered to be, in effect, infinite with no
reflected wave being present.

Multilayer transmission theory has been shown by
Hill[17] to be generally applicable to multilayer acoustic
emission transducers. Here we consider an acoustic
emission transducer to be a 5-layer system with a wave
normally incident on the interface between layers 1 and 2.
The incident wave has pressure p and velocity v_1, the
reflected wave has pressure p_r and velocity v_r and the
transmitted wave has pressure p_t and v_t. The detailed
notation for waves normally incident on n layers is shown
in Figure 4.9.

The following assumptions are made concerning the
transmission of waves through the multilayer system:

1) the layers are assumed to be of infinite extent
in the y and z directions; 2) the reflected wave in medium
n is assumed to be non-existent; 3) even though the
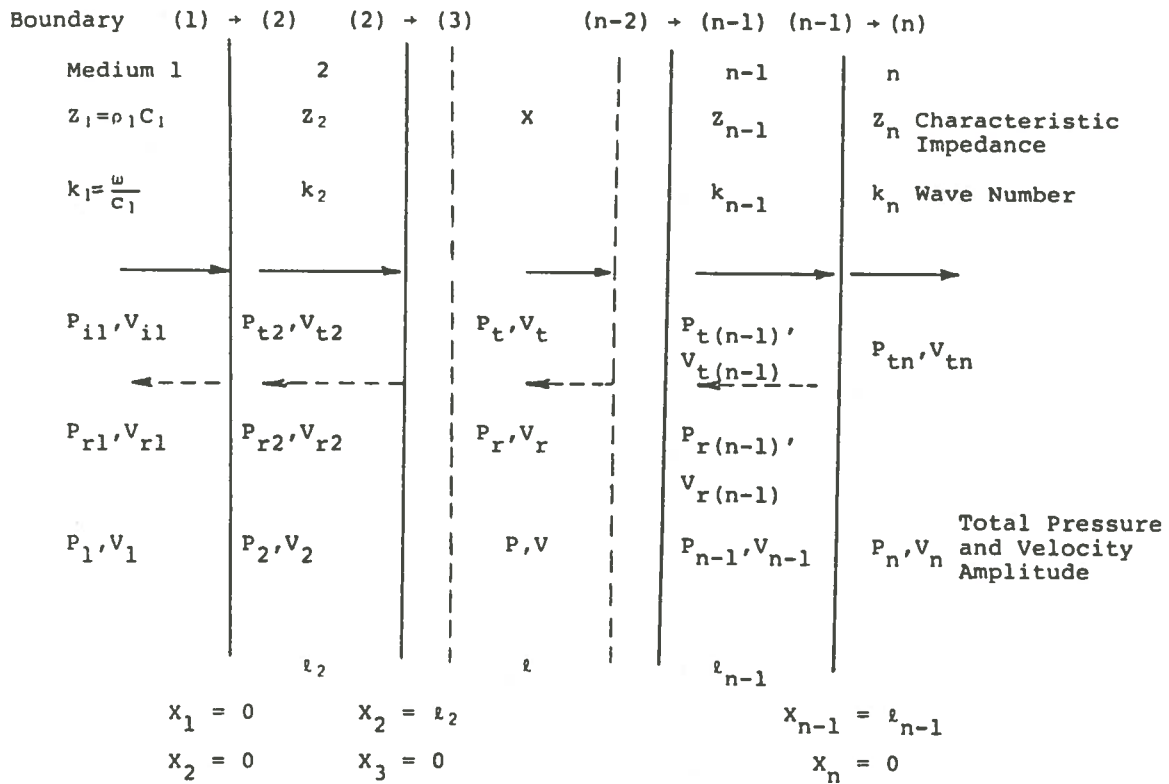
Figure 4.9. The transmission of normally incident longitudinal waves through a multilayer system. (Per Hill[16])

bounded media would produce multiple reflections and transmissions at the boundaries surrounding it, it is sufficient to suppose that there is only one wave in each direction (provided that the boundary conditions are satisfied, these will include all the individual components); and, 4) the fact that, during the transmission process, the P.Z.T. element does actually extract some energy from the acoustic wave and convert it to an electrical one is neglected. This approximation is correct only if the transducer is open circuit. It has been pointed out by de Klerk[18] that the great mismatch in electrical impedance between the transducer and the amplifier would indicate that very little signal is lost in such a manner.

Five Layer Transmission Theory

It has been shown by Hill that adapting the matrix technique for a solution proposed by Thomson[19], a solution for five layer transmission can be obtained. This theory is applicable to transmission through the various layers of some acoustic emission transducers.

If the amplitude of the wave transmitted into layer 5 is A_5, and the amplitude of the incident wave is A_1, then:

$$\frac{A_1}{A_5} = \frac{1}{2} \left(F_1 \cos k_2 \ell_2 \cos k_3 \ell_3 \cos k_4 \ell_4 \right.$$

$$- F_2 \sin k_2 \ell_2 \sin k_3 \ell_3 \cos k_4 \ell_4 - F_3 \cos k_2 \ell_2 \sin$$

$$k_3 \ell_3 \sin k_4 \ell_4$$

$$- F_4 \sin k_2 \ell_2 \cos k_3 \ell_3 \sin k_4 \ell_4)$$

$$+ j \, (F_5 \cos k_2 \ell_2 \sin k_3 \ell_3 \cos k_4 \ell_4 + F_6 \cos k_2 \ell_2$$

$$\cos k_3 \ell_3 \sin k_4 \ell_4$$

$$+ F_7 \sin k_2 \ell_2 \cos k_3 \ell_3 \cos k_4 \ell_4 - F_8 \sin k_2 \ell_2 \sin$$

$$k_3 \ell_3 \sin k_4 \ell_4) \tag{4.6}$$

where

$$F_1 = 1 + \frac{z_1}{z_5} \qquad , \qquad F_2 = \frac{z_2}{z_3} + \frac{z_1 z_3}{z_2 z_5}$$

$$F_3 = \frac{z_3}{z_4} + \frac{z_1 z_4}{z_3 z_5} \qquad , \qquad F_4 = \frac{z_2}{z_4} + \frac{z_1 z_4}{z_2 z_5}$$

$$F_5 = \frac{z_1}{z_3} + \frac{z_3}{z_5} \qquad , \qquad F_6 = \frac{z_1}{z_4} + \frac{z_4}{z_5}$$

$$F_7 = \frac{z_1}{z_2} + \frac{z_2}{z_5} \qquad , \qquad F_8 = \frac{z_1 z_3}{z_2 z_4} + \frac{z_2 z_4}{z_3 z_5}$$

$$\tag{4.7}$$

The sound pressure transmission coefficient is given by:

$$\alpha_{p5} = \frac{A_5}{A_1}$$

and the sound power transmission coefficient by

$$\alpha_{w5} = \left| \frac{A_5}{A_1} \right|^2 \frac{Z_1}{Z_5} \tag{4.8}$$

Six Layer Transmission Theory

Using the matrix method of solution for a six layer system yields a matrix equation of the form:

$$T_1 = C_2\, C_3\, C_4\, C_5\, T_5 \tag{4.9}$$

If this matrix equation is written out in full;

$$\begin{bmatrix} A_1+B_1 \\ \\ \dfrac{A_1-B_1}{Z_1} \end{bmatrix} = \begin{bmatrix} \cos k_2 \ell_2 & jZ_2 \sin k_2 \ell_2 \\ \\ \dfrac{j \sin k_2 \ell_2}{Z_2} & \cos k_2 \ell_2 \end{bmatrix} \begin{bmatrix} \cos k_3 \ell_3 & jZ_3 \sin k_3 \ell_3 \\ \\ \dfrac{j \sin k_3 \ell_3}{Z_2} & \cos k_3 \ell_3 \end{bmatrix}$$

$$\times \begin{bmatrix} C_4 \end{bmatrix} \times \begin{bmatrix} C_5 \end{bmatrix} \begin{bmatrix} A_6 \\ A_6 \\ \dfrac{A_6}{Z_6} \end{bmatrix} \tag{4.10}$$

Matrix T_1 contains terms relating to medium 1 only. A_1 is the amplitude of the incident pressure wave, B_1 is the amplitude of the reflected wave and Z_1 is the specific acoustic impedance for medium 1. The matrices C_2, C_3, C_4, C_5 each contain constants relating to media 2,....5 respectively. The form of these matrices is seen in

Eq. 4.10 for media 2 and 3. Matrix T_5 contains the pressure amplitude A_6 applicable at boundary 5 and in medium 6.

Solution of Eq. 4.10 yields the following result:

$$
\begin{aligned}
\frac{A_1}{A_6} = \frac{1}{2} \Big[\big(& S_1 \cos k_2 \ell_2 \cos k_3 \ell_3 \cos k_4 \ell_4 \cos k_5 \ell_5 \\
& + S_2 \sin k_2 \ell_2 \sin k_3 \ell_3 \sin k_4 \ell_4 \sin k_5 \ell_5 \\
& - S_3 \sin k_2 \ell_2 \sin k_3 \ell_3 \cos k_4 \ell_4 \cos k_5 \ell_5 \\
& - S_4 \cos k_2 \ell_2 \sin k_3 \ell_3 \sin k_4 \ell_4 \cos k_5 \ell_5 \\
& - S_5 \sin k_2 \ell_2 \cos k_3 \ell_3 \sin k_4 \ell_4 \cos k_5 \ell_5 \\
& - S_6 \sin k_2 \ell_2 \cos k_3 \ell_3 \sin k_4 \ell_4 \sin k_5 \ell_5 \\
& - S_7 \sin k_2 \ell_2 \cos k_3 \ell_3 \cos k_4 \ell_4 \sin k_5 \ell_5 \\
& - S_8 \sin k_2 \ell_2 \cos k_3 \ell_3 \sin k_4 \ell_4 \cos k_5 \ell_5 \big) \\
+ j \big(& S_9 \cos k_2 \ell_2 \cos k_3 \ell_3 \cos k_4 \ell_4 \sin k_5 \ell_5 \\
& + S_{10} \cos k_2 \ell_2 \cos k_3 \ell_3 \cos k_4 \ell_4 \cos k_5 \ell_5 \\
& + S_{11} \cos k_2 \ell_2 \sin k_3 \ell_3 \cos k_4 \ell_4 \cos k_5 \ell_5 \\
& + S_{12} \sin k_2 \ell_2 \cos k_3 \ell_3 \cos k_4 \ell_4 \cos k_5 \ell_5 \\
& - S_{13} \sin k_2 \ell_2 \sin k_3 \ell_3 \cos k_4 \ell_4 \sin k_5 \ell_5 \\
& - S_{14} \cos k_2 \ell_2 \sin k_3 \ell_3 \sin k_4 \ell_4 \sin k_5 \ell_5
\end{aligned}
$$

$$- S_{15} \sin k_2 \ell_2 \cos k_3 \ell_3 \sin k_4 \ell_4 \sin k_5 \ell_5$$

$$- S_{16} \sin k_2 \ell_2 \sin k_3 \ell_3 \sin k_4 \ell_4 \cos k_5 \ell_5)]$$

$$(4.11)$$

where

$$S_1 = 1 + \frac{z_1}{z_6} \qquad\qquad S_2 = \frac{z_2 z_4}{z_3 z_5} + \frac{z_1 z_3 z_5}{z_2 z_4 z_6}$$

$$S_3 = \frac{z_2}{z_3} + \frac{z_2 z_3}{z_2 z_6} \qquad\qquad S_4 = \frac{z_3}{z_4} + \frac{z_1 z_4}{z_3 z_6}$$

$$S_5 = \frac{z_2}{z_4} + \frac{z_1 z_4}{z_2 z_6} \qquad\qquad S_6 = \frac{z_4}{z_5} + \frac{z_1 z_5}{z_4 z_6}$$

$$S_7 = \frac{z_2}{z_5} + \frac{z_1 z_5}{z_2 z_6} \qquad\qquad S_8 = \frac{z_3}{z_5} + \frac{z_1 z_5}{z_3 z_6}$$

$$S_9 = \frac{z_1}{z_5} + \frac{z_5}{z_6} \qquad\qquad S_{10} = \frac{z_1}{z_4} + \frac{z_4}{z_6}$$

$$S_{11} = \frac{z_1}{z_3} + \frac{z_3}{z_6} \qquad\qquad S_{12} = \frac{z_1}{z_2} + \frac{z_2}{z_6}$$

$$S_{13} = \frac{z_1 z_3}{z_2 z_5} + \frac{z_2 z_5}{z_3 z_6} \qquad\qquad S_{14} = \frac{z_1 z_4}{z_3 z_5} + \frac{z_3 z_5}{z_4 z_6}$$

$$S_{15} = \frac{z_1 z_4}{z_2 z_5} + \frac{z_2 z_5}{z_4 z_6} \qquad\qquad S_{16} = \frac{z_1 z_3}{z_2 z_4} + \frac{z_2 z_4}{z_3 z_6} \qquad (4.12)$$

Again, the sound pressure transmission coefficient is given by:

$$\alpha_{p6} = A_6/A_1 \qquad\qquad (4.13)$$

and the sound power transmission coefficient by

$$\alpha_{w6} = \left| \frac{A_6}{A_1} \right| ^2 \frac{Z_1}{Z_6} \tag{4.14}$$

Evaluation of the Five Layer Sound Pressure Transmission Coefficient

In Figure 4.10, the sound pressure transmission coefficient is calculated for a Dunegan/Endevco S750 transducer coupled to aluminum using silicone grease. The graphs show the theoretical variation of transmission coefficient with frequency for couplant thicknesses of 0.3 mm, 0.5 mm and 1.0 mm. The sound pressure transmission coefficient (P.T.C) is plotted in decibels (dB).

The value of 0 dB corresponds to a P.T.C. of unity, i.e., all the incident signal is transmitted through the five layer system. The curves in Figure 4.10 show peaks corresponding to enhanced signal transmission at specific frequencies, the positions of these peaks being dependent on the thickness of the couplant layer.

Multilayer transmission theory has important applications in the design of acoustic emission components selected to give a specified frequency response. The response of the system is modified by the thickness of the couplant depending on the frequency band being used. Care would be needed at certain frequencies where measurement precision would be severely degraded by couplant thickness fluctuations.
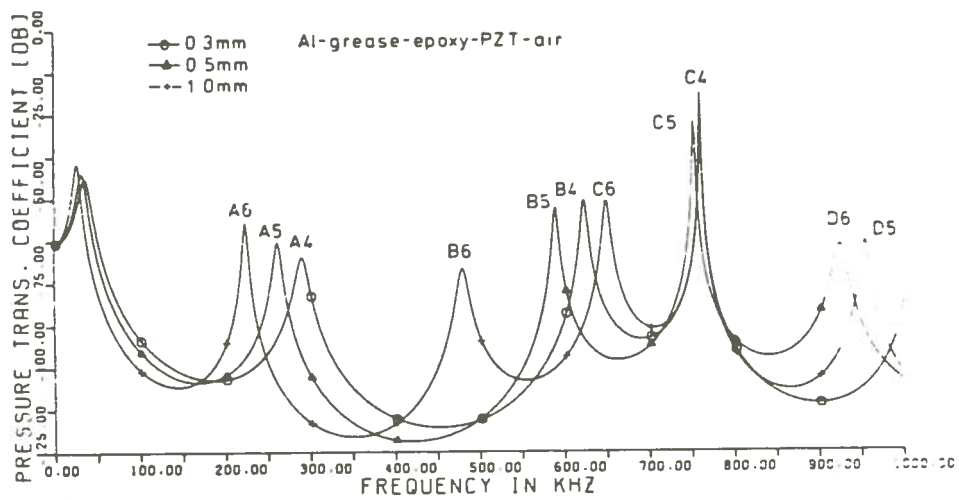
Fig. 4.10. Theoretical "response" for an S750 transducer using a grease couplant of the specified thickness. (Per Hill[16])

Chapter 5

IMPACT LOCATION METHODS

One-Dimensional Impact Location

Acoustic Emission Impact Location by Time Difference Module

The Time Difference Module[20] (TDM) as shown in
Figure 5.1 compares the time-of-arrival of an acoustic
event at two different sensors (channels). The first
sensor to detect the event starts the location clock, the
second stops it. We refer to this difference in time as
Delta t or DT.

If an acoustic event (AE) occurs at point (a) in
Figure 5.1, beyond or equal to the location of sensor #1,
then the location clock will be on for the longest time.
This will be the highest DT possible. The wave velocity
in the test specimen can be easily determined by the
familiar formula:

R = D/T, or velocity = distance (measured)/max DT

    x location clock period.

If the AE occurs at the exact midpoint between the
sensors, as in case b above, then the AE signal will
reach the sensors simultaneously, and DT will be zero.

We assume that the AE signal travels omnidirection-
ally at equal velocities; therefore, if the AE source lies

63

Sensor #1

Sensor #2

TEST SPECIMEN

(* = source of AE)

(a) DT=MAXIMUM-------
(b) DT=∅.
(c) DT=LOCATION-------
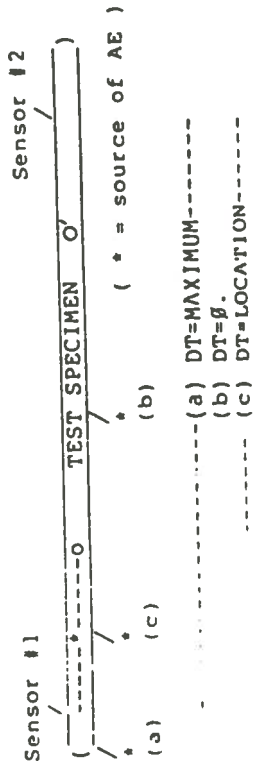
Figure 5.1 Arrival time of acoustic event
(Per AET20)

TDM

Sensor #1

Sensor #2

Specimen

Source of
Acoustic Event
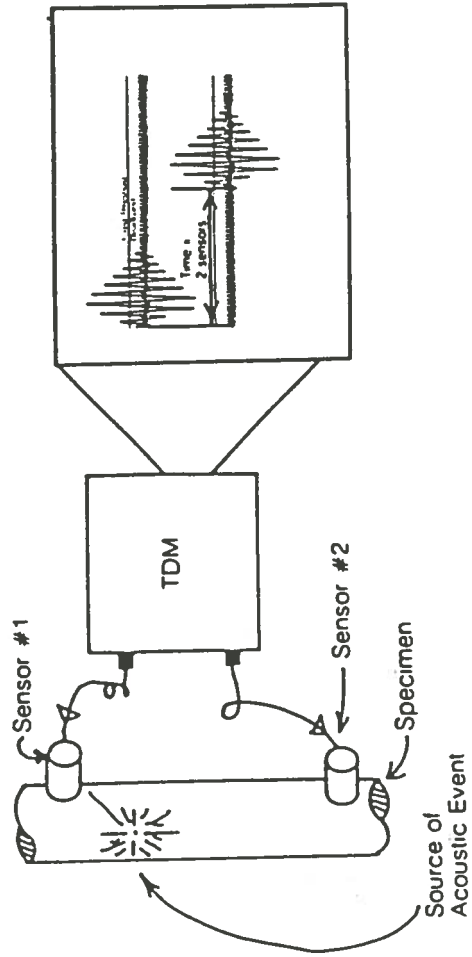
Figure 5.2 time difference module
(Per AET20)

nearer one sensor than the other (as in example (c)),
the location clock will start when the AE signal reaches
point "O" and will stop when it reaches sensor #2. The
location of point (c) is therefore determined by the
formula:

$$\text{Location} = \frac{(\text{maximum DT}) - \text{sample DT}}{2} \times \frac{\text{sensor spacing}}{\text{max DT}}$$

An event occurring at location O causes a certain
DT. But an event at a location O' at the other end of
the test specimen might cause an identical DT, except
that sensor #2 would activate the location clock. There-
fore, every possible DT (other than zero) indicates two
locations. The first sensor to receive the AE wave
indicates the precise location. If the AE occurs at
point O, the sensors will be struck in the order 1,2.
Should the origin of the AE lie at point O', the sensors
will be struck in the order 2,1. Formulas for location O
and O' are:

$$\text{Location O} = \frac{(\text{max DT}) - \text{DT}}{2} \times \frac{\text{sensor spacing}}{\text{max DT}}$$

$$\text{Location O'} = \text{sensor spacing} - \frac{(\text{max DT}) - \text{DT}}{2}$$
$$\times \frac{\text{sensor spacing}}{\text{max DT}}$$

The time difference module is shown in Figure 5.2.

Impact Location by Signal Amplitude Ratio Module

A Signal Amplitude Ratio Module (SAM) is based upon the fact that the sensor closer to the impact has higher response. This technique uses short-term-averaged, root-mean-square (RMS) signal representation. With a proper choice of averaging time, information-bearing waveform features can be retained while purely statistical fluctuations are effectively eliminated. In addition, an easily discerned maximum response value is obtained (e.g., for use with locational algorithms based on signal attenuation with distance from the impact), and the non-linear treatment of the large signal amplitudes associated with true impact signals that is provided by the RMS computation helps discriminate against small-amplitude background noise and thereby improves the signal-to-noise ratio.

Location is determined by matching signal amplitude at each detector to a signal attenuation curve, as shown in Figure 5.3 and Figure 5.4. If the signal-to-signal ratio (detector 1 signal/detector 2 signal) is 2:1, the impact is 100 ft. to the left of center of the section. If the ratio is 4:1 then the impact is located at 275 ft. to the left of mid-point.
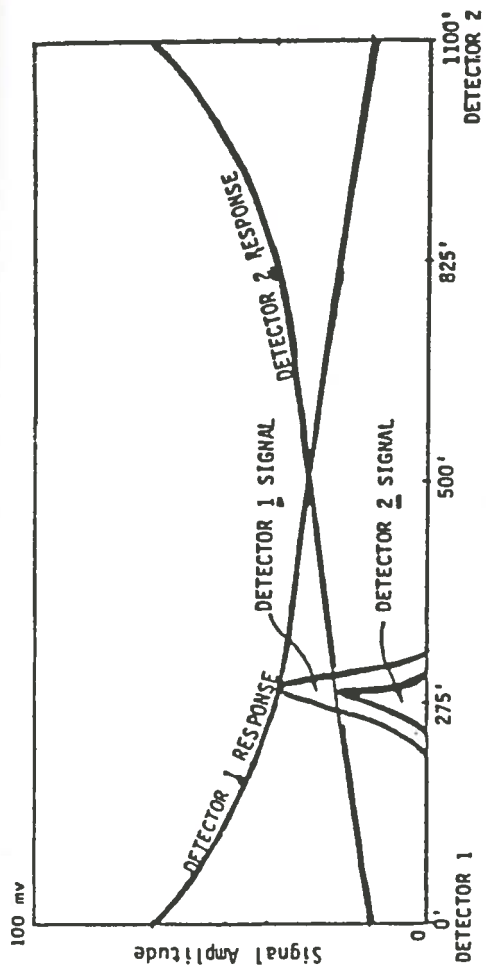
Fig. 5.3. Location of impact using signal amplidude/ratio
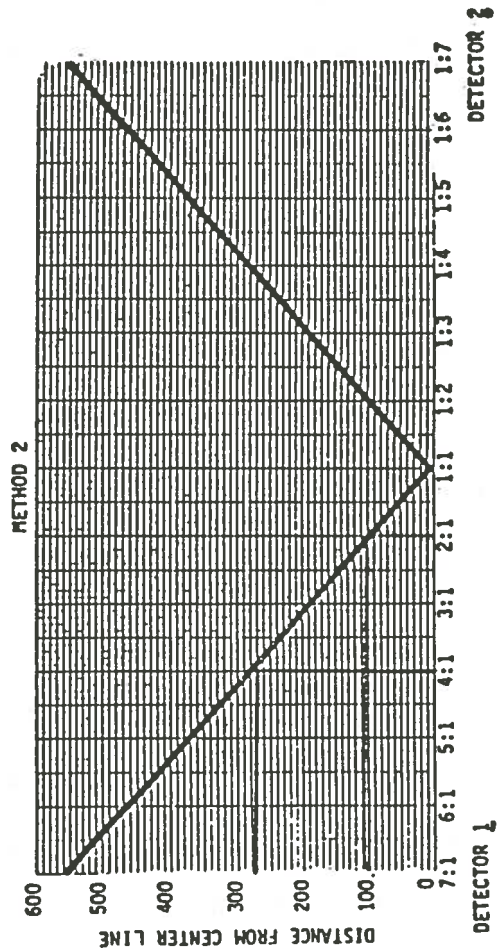
Fig. 5.4. Calibration of signal attenuation

Two-Dimensional Impact Location

Impact Location Using Time Difference Method[21]

Impact location using time difference method is based upon the knowledge of the speed of impact wave propagation. This method has been employed in most current commercial LPMS's used on nuclear power plants. The general formulation for impact location on a flat surface in a two-dimensional cartesian coordinate system is given by

$$[(x-x_i)^2 + (y-y_i)^2]^{1/2} - [(x-x_j)^2 + (y-y_j)^2]^{1/2}$$

$$= f(\Delta L)_{ij} \qquad (5.1)$$

where

(x,y) = coordinate of the impact point

$(x_i,y_i),(x_j,y_j)$ = coordinate of accelerometer i and j

$f(\Delta L)_{ij}$ = a function that relates ΔL to a signal parameter (e.g., time of arrival or amplitude at arrival or frequency content at arrival).

$(\Delta L)_{ij}$ = acoustical path difference between accelerometer i and j.

In this method, the function $f(\Delta L)$ can be expressed in exact form by

$$f(\Delta L)_{ij} = \Delta t_{ij} * V \qquad (5.2)$$

where

V = speed with which the acoustic wave traverses the medium

Δt_{ij} = difference in signal arrival time from sensor j to i.

The speed of acoustic wave propagation can be measured using known impact positions and accelerometer locations. Also the time difference of the wave arrival can be measured from the accelerometers' time domain signal. Substituting Eq. (5.2) into (5.1) will lead to the equation of a hyperbola. The point of impact is located at the intersection of three hyperbola obtained from the time-of-arrival difference of three accelerometer signals. This method can be used for any complicated structure (e.g., pressure vessel). Knowing the speed of propagation and time of impact arrival at several positions, a simple triangulation should locate the point of impact. In practice one must determine the velocity of impact wave experimentally. This is warranted due to nonideal condition of practical structures such as surface conditions, material thickness and obstructions.

Impact Location Using Amplitude Ratio Method[22]

Impact location using the amplitude ratio method is based upon the fact that, given several monitoring positions on the reactor pressure vessel and unknown impact

upon the vessel, the sensor closest to the impact has the highest response. To use a relative-signal-amplitude-at-arrival description for $f(\Delta L)$, Eq. (5.1) must be modified, with ratios of acoustic path lengths rather than their differences now constituting the appropriate modeling variable. Accordingly, with an assumption that the amplitude A_i of the ith accelerometer's response is inversely proportional to its distance $\bar{r}_i$ from the impact point raised to an appropriate power j, that is

$$A_i = A_o/(\bar{r}_i)^j \qquad (5.3)$$

where

A_i = response of accelerometer i to an impact a distance $\bar{r}_i$ away,

$\bar{r}_i$ = vector from point of impact to accelerometer i,

j = attenuation power (typically $1 \leq j \leq 2$, depending on the structure geometry),

A_o = impact constant.

For a two-dimensional flat plate, the general formula for impact location is as follows:

$$[\frac{(x-x_j)^2 + (y-y_j)^2}{(x-x_i)^2 + (y-y_i)^2}]^{1/2} = A_i/A_j, \qquad (5.4)$$

where A_i and A_j are peak amplitude or peak RMS at position i and j. This equation can be solved for the impact coordinates (x,y). In this method, the peak time-dependent RMS recorded by each accelerometer was selected as the measure of signal amplitude and used as the sensor response.

Three-Dimensional Impact Location

Triangulation techniques are used to find the impact location. One system for triangulation involves construction of three intersecting hyperbolas by using two or three equations of the type

$$X^2 - Y^2 = A^2$$

A second method for impact location is to employ the Apolonian construction discovered by Appolonius of Perga, a 3rd century B.C. Greek mathematician.[23] This construction locates the center of a circle which passes through a fixed point and is tangent to two given circles. Actual construction of the unknown circle with radius e is not necessary. A much simpler method consists of drawing a series of concentric circles on a thin clear plastic overlay sheet and by observation and trial and error finding the circle which is the best fit for the condition. The center of this circle is the impact

location. It should be noted that there are usually more possible solutions to the Appolonian construction. The correct solution is obtained by noting the order in which the emissions are received at each sensor.

In both analyses, the accuracy of impact location depends heavily upon uniform acoustic properties of the specimen. Since acoustic emissions are primarily surface waves.

Another method of impact location that uses the signal arrival time from impact to the accelerometer is the arrival time, as obtained from accelerometers, is used for the pattern information that is inherent in impact position. This method is briefly discussed in Appendix A.

Chapter 6

EXPERIMENTAL LOCATION OF LOOSE PARTS IMPACT

Experimental Facility and Procedures

The three-dimensional impact location experiments were conducted on a modified subcritical assembly vessel. The vessel has a radius 58.42 centimeters and a thickness of 0.635 centimeters, and was 152.4 centimeters in height. The only obstruction on the vessel is an overflow outlet pipe.

A total of six AET model AC 175-L sensors were used. The sensors were attached to the vessel and a couplant used as an interface. The sensors were held to the vessel by adhesive tape. Sensors locations are shown in Figure 6.1 and Figure 6.2. To simulate boiling, a hose in the form of series of concentric circles was layed on the fuel rod holder. Small holes were drilled into the hose uniformly; one end of the hose was sealed off, and the other was attached to an air compressor as shown in Figure 6.3. The electronics and data acquisition system used consists of AET model AC 175-L sensors with a nominal resonance of 175 KHZ. The preamplifiers were AET model 160B's, which provides 60 dB of gain, an eight-channel acoustic processing unit, an AET 5000 TV screen, and a printer. The schematic diagram of the data collection is shown in Figure 6.4.
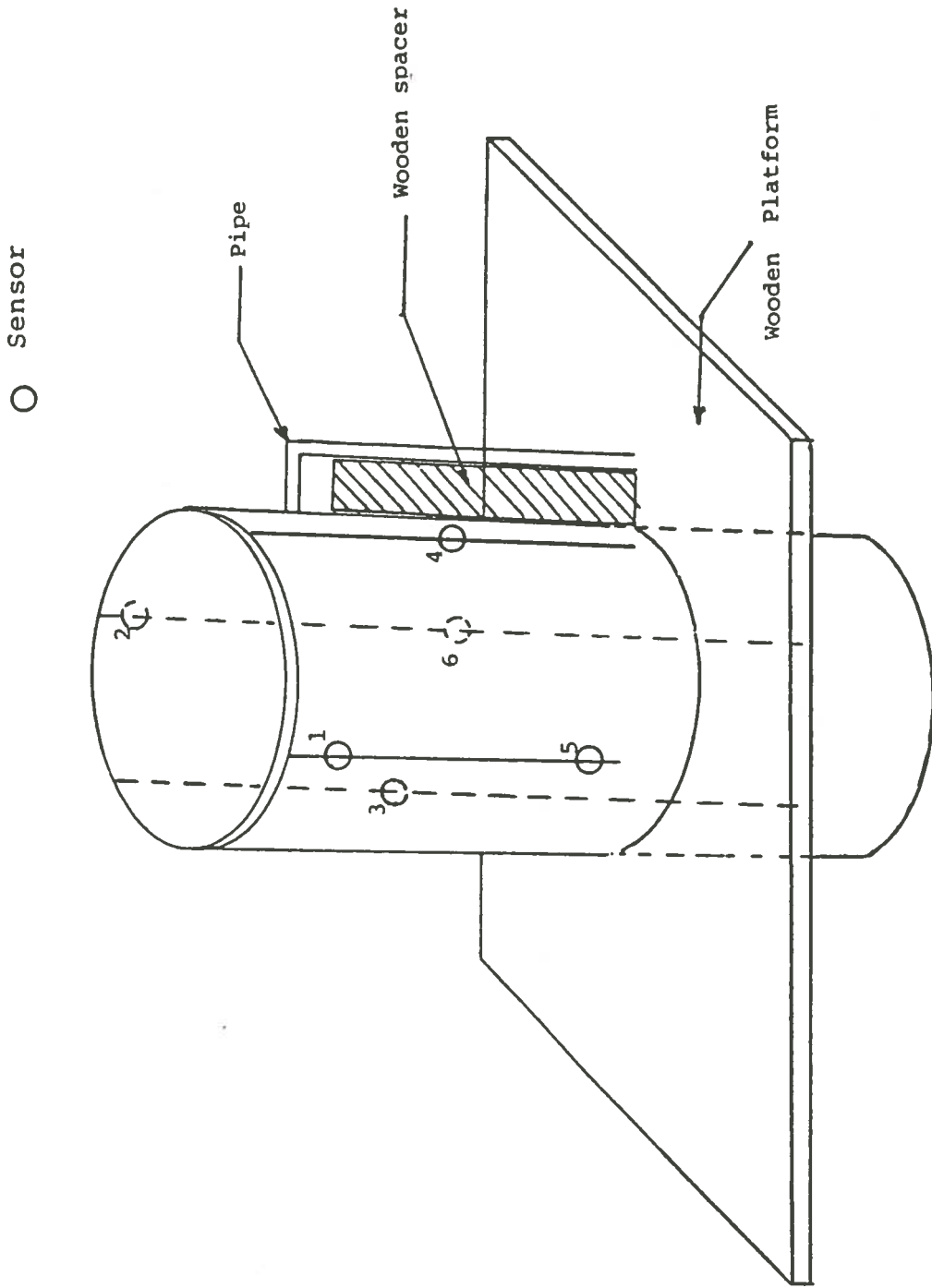
Fig. 6.1. Vessel for the subcritical reactor assembly
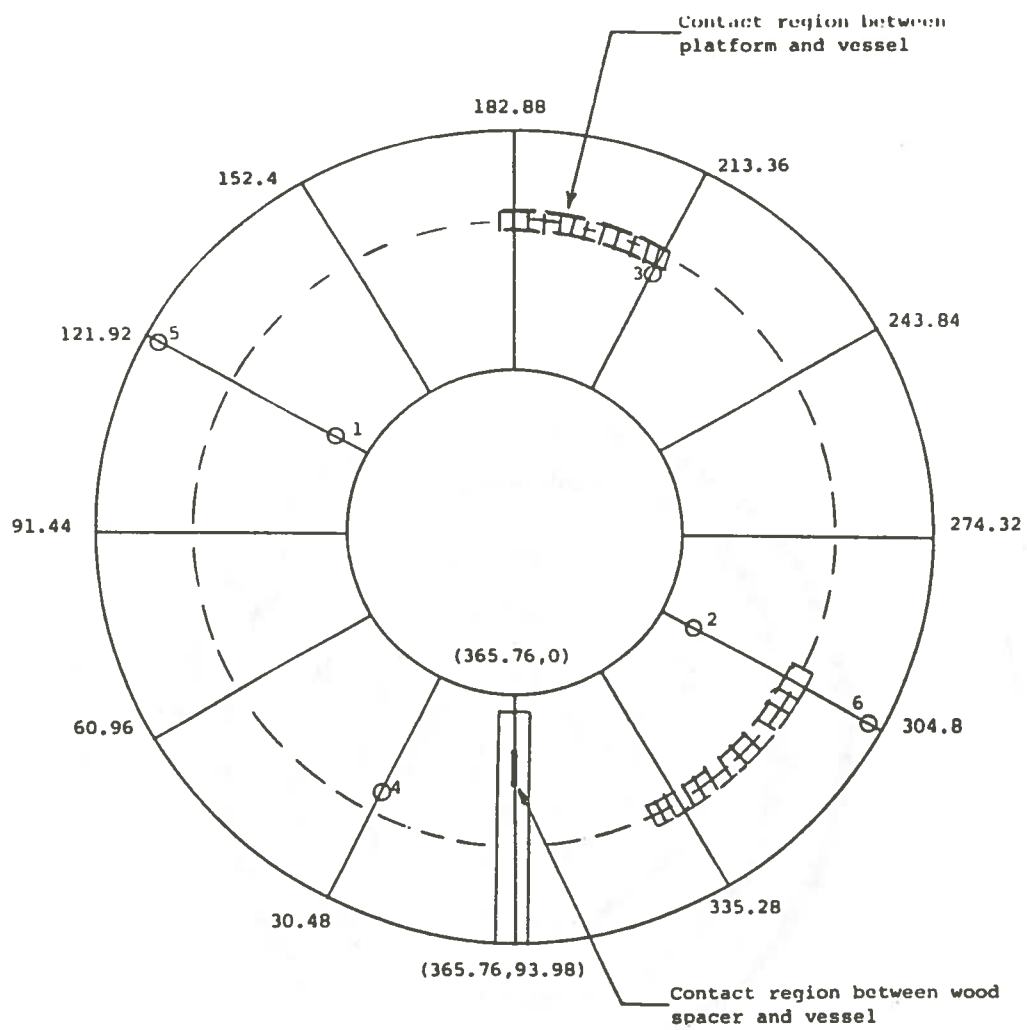
Fig. 6.2.   Layout of Vessel
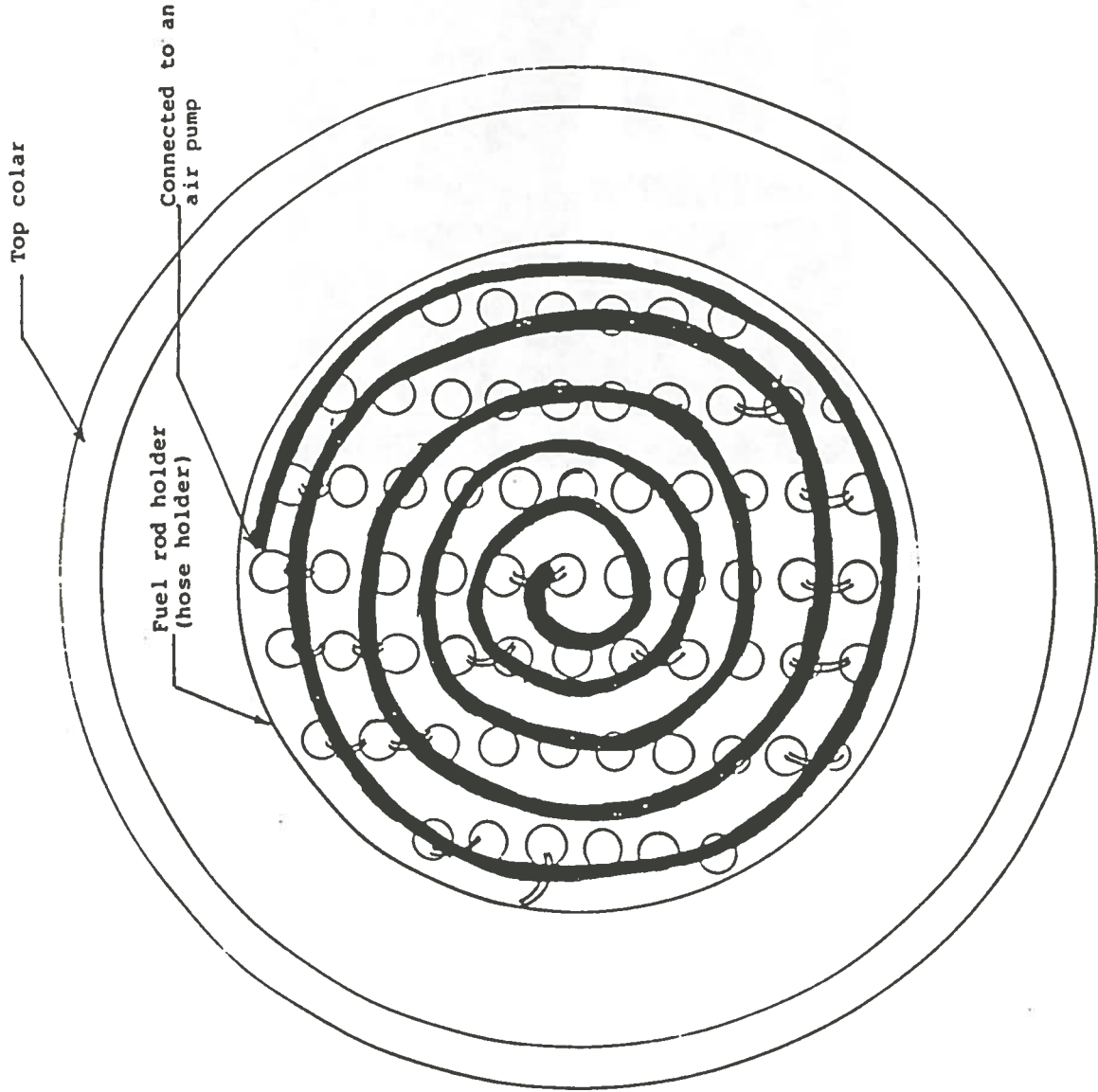
Fig. 6.3. Hose layout for boiling simulation
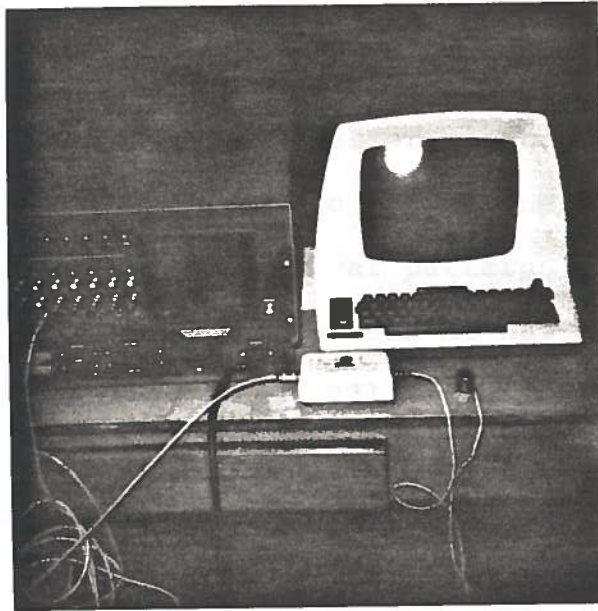
Fig. 6.4. Schematic diagram for data collection

Procedures for chosing zones (area of interest) are as follows: six sensors were used for this test. At least three sensors are required but more sensors will give better results. Sensors were placed on the vessel as shown in Figure 6.2. A total of eight zones are produced which will be assigned to region one. For each zone, all possible signal arrival patterns were input into the system. For example, zone Al has six possible signal arrival patterns (213, 231, 123, 132, 312, 321) as shown in Figure 6.5.

This method of impact location will provide us two useful pieces of information: 1) the order in which the acoustic waves strike the sensors and 2) the difference in the times of arrival of the acoustic wave betwen sensors.

Results and Discussion

Impact Energy

A toy gun was used as the impactor. To find the impact energy on the vessel the following experiment was performed. Assume the gun is fired from point A with a muzzle velocity V_1, as shown in Figure 6.6. When the gun is located at an elevation h above the ground, the equation that describes the trajectory AB can be obtained. When the ball is at the arbitrary point $P(x,y)$, the three
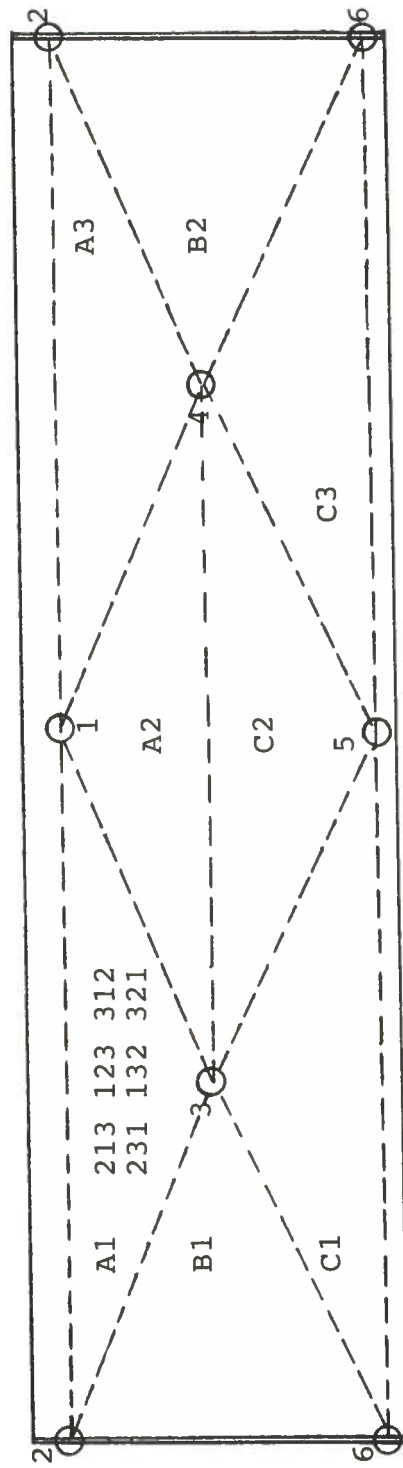
Fig. 6.5. Location of each zone on the vessel

unknowns between point A and P are the velocity components V_x and V_y at P and the time of flight, t. The initial velocity has components $(V_x)_1 = V_1$ and $(V_y)_1 = 0$, and the acceleration at any point has components $a_x = 0$, $a_y = -g$. To obtain the equation of the path, $y = f(x)$, the position coordinates x and y can be expressed in terms of the unknown parameter t. Eliminating t yields the locus $y = f(x)$. In particular, the x coordinate is related to t by the equation

$$S_x = (S_x)_1 + (V_x)_1 t$$

$$x = 0 + V_1 t$$

Similarly, y is related to t by the equation

$$S_y = (S_y)_1 + (V_y)_1 t + 1/2\ a_c t^2$$

$$y = 0 + 0 - 1/2\ gt^2$$

Eliminating t and solving for y yields

$$y = \frac{-g}{2V_1^2}\ x^2$$

This parabolic path AB is shown in Figure 6.6. Note that the range R or horizontal distance to where the ball strikes the ground, is determined by substituting $y = -h$ into the above equation and solving for $x = R$, i.e.,
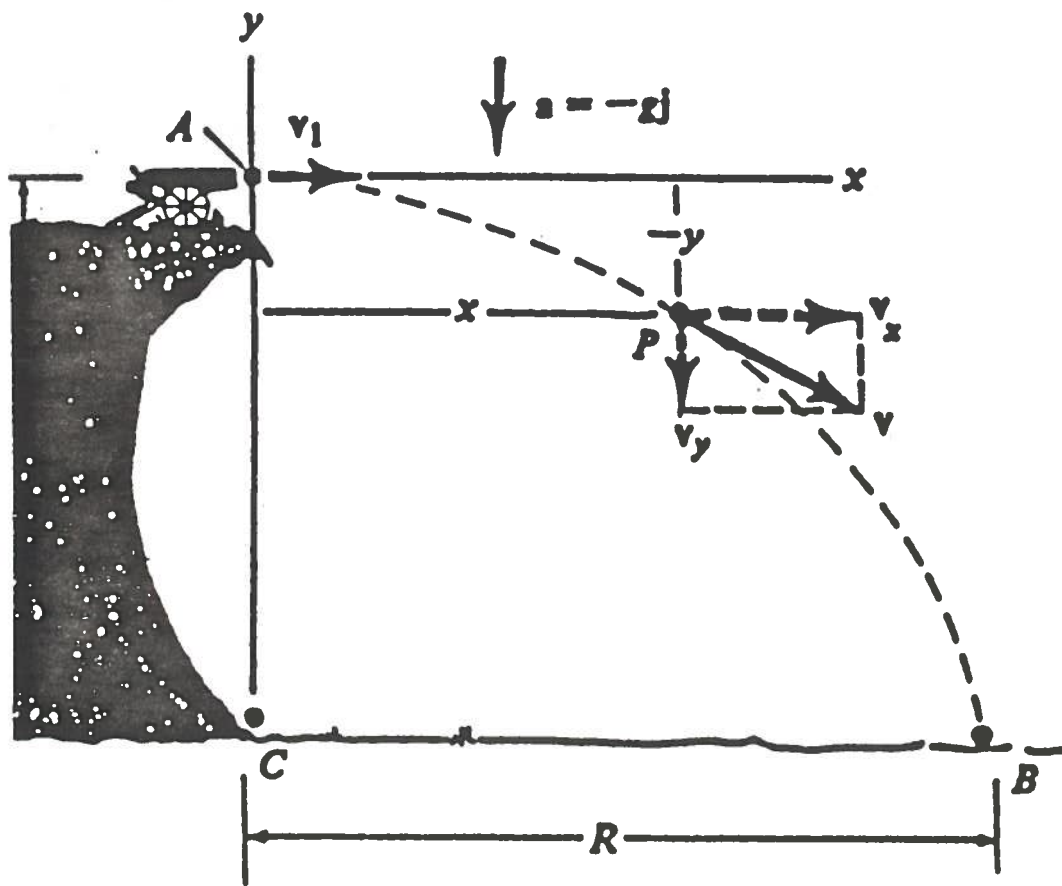
Fig. 6.6. Missile trajectory (R. C. Hibbeler,
       Engineering Mechanics: Dynamics,
       Macmillan Publishing Co., New York,
       (1978), p. 30)

$R = V_1 \sqrt{2h/g}$. The kinetic energy at the nozzle will be given by the equation:

$$KE = 1/2 \; mV_1^2$$

The impact energy is equal to kinetic energy at the nozzle because the gun was held right on the surface of vessel when fired each time. The calibration (for this spring type toy gun) experiment leads to

$$m = 1/3 \text{ gram}$$
$$h = .94 \text{ m}$$
$$R = 18.6 \pm 0.1 \text{ m}$$
$$g = 9.80 \text{ m/s}^2$$

$$V_1 = \frac{R}{2 \; h/g}$$

$$KE = 1/2 \; MV_1^2 \; (1/3)(42.46)^2/1000 = .3 \; \frac{kg \; m^2}{s^2}$$

$$= .3j$$

Impact Wave Velocity

The impact wave velocity was measured using known impact positions and sensor locations, and the time of arrival differences. Table 6.1 shows several velocity measurements. Then the Chauvenet criterion is used for the rejection of data. Chauvenet's criterion states that an observation should be discarded if the probability of

Table 6.1. Measured Velocity of Impact Wave in Vessel

Observation N	Impact Coordinates (cm) X	Y	Signal Arrival	Shortest Path Difference (cm) (R_2-R_1)	Time Difference (μsec)	Velocity Measured (m/sec)	$\tau = (n-\bar{n})/s$
1	60.96	33.02		64-34	55	5454	.03
2(a)	60.96	58.42		87-33.5	65	8230	2.15>2.13
3	91.44	33.02		66-37	46	6304	.63
4(a)	91.44	58.42		46-55	34	2647	2.24>2.13
5	152.4	33.02		61-37	46	5217	.22
6	152.4	83.82		70-27	88	4886	.48
7	182.88	58.42		63.5-33	63	4841	.52
8	243.84	58.42		68-32	77	4675	.65
9	274.32	83.82		71-32	84	4642	.67
10	274.13	33.02		62-37	41	6097	.46
11	345.44	33.02		63-35	41	6829	1.04
12	345.44	58.42		55-40	35	4285	.05
13	365.76	33.02		65-34	52	5961	.36
14	365.76	58.42		66.5-34	50	6500	.78

(a) Velocity should be discarded

mean velocity $\bar{n} = \sum_1^{14} V/14 = 5501.75$ m/sec

standard deviation $s = \sqrt{1/N-1 \sum_1^{14} (n-\bar{n})^2} = \pm 1270$ m/sec

$$\tau = \frac{1(n-\bar{n})1}{s}$$

its occurrence is equal to or less than $1/(2N)$. Where N is the number of observations. For simplicity, these limits are given in Table 6.2 in terms of the ratio of the deviation to the standard deviation, i.e., $(n-\bar{n})/s$, for various numbers of observations N. Comparing Table 6.1 and 6.2, it is obvious that the second and fourth observations should be discarded. The remaining data in Table 6.3 were tested again after rejections, and all values satisfied Chauvenet's criterion. The impact wave velocity was taken as the average velocity of the 12 remaining observations, which is 5474.25 m/sec. (See Table 6.3).

Parabolic Intersection Procedure

In principle, the impact point of a loose part with the wall of a vessel can be calculated exactly from the hyperbolic equations developed in the preceding chapter for a three-sensor array. The intersection of the three hyperbolas for each sensor pair will be the exact theoretical impact point. In reality, however, a number of factors introduce uncertainties into the parabola calculations, and these therefore are best represented as paths with finite width. The uncertainties are introduced from indeterminate experimental errors such as the measurement of the speed of sound and the finite resolving time

Table 6.2. Chauvenet's Criterion (G. D. Chase, J. L. Rabinowitz, Principles of Radioisotope Methodology, Third Edition, p. 105)

N	$(n-\bar{n})/s = \tau$	N	$(n-\bar{n})/s = \tau$
2	1.15	30	2.40
3	1.38	35	2.45
4	1.54	40	2.50
5	1.65	50	2.58
6	1.73	75	2.71
7	1.80	100	2.81
8	1.86	200	3.02
9	1.91	250	3.09
10	1.96	300	3.14
12	2.04	400	3.23
15	2.13	500	3.29
20	2.24	1000	3.48
25	2.33		

Table 6.3. Measured Velocity of Impact Wave in Vessel

Observation N	Coordinates (cm) X	Y	Signal Arrival	Shortest Path Difference (cm) (R_2-R_1)	Time Difference (μsec)	Velocity Measured (m/sec)	τ = (n-n̄)/s
1	60.96	33.02		64-34	55	5454	.02
2	91.44	33.02		66-37	46	6304	.98
3	152.4	33.02		61-37	46	5217	.95
4	152.4	83.82		70-27	88	4886	.99
5	182.88	58.42		63.5-33	63	4841	.30
6	243.84	58.42		68-32	77	4675	.70
7	274.32	83.82		71-32	84	4642	.75
8	274.13	33.02		62-37	41	6097	.74
9	345.44	33.02		63-35	41	6829	.58
10	345.44	58.42		55-40	35	4285	1.22
11	365.76	33.02		65-34	52	5961	1.61
12	365.76	58.42		66.5-34	50	6500	1.4

mean velocity $\bar{n} = \sum_1^{14} v/12 = 5474.25$

standard deviation $s = \sqrt{1/N-1 \sum_1^{14} (n-\bar{n})^2} = \pm 840$

$$\tau = \frac{1(n-\bar{n})1}{s}$$

of the sensor. In addition calculational errors are introduced by numerical procedures used in determining the intersection of three parabolas within a superimposed finite grid with 1 cm spacing. The impact point is located somewhere within the area defined by the inter-section of the three parabolic paths, but cannot be established with a precision better than that of the path widths.

A computer program was written to generate the finite-width parabolic paths on a color monitor and determine the area of intersection (see Appendix B). The program steps through all points in a rectangular grid overlayed on the region of interest, and determines if the grid point under consideration is a valid solution, within a prescribed uncertainty, for one, two, or all three of the paths, or for none of them. Each valid point is plotted in a unique color to provide a visual solution to the data provided. Grid points which are valid solutions to all three para-bolic paths simultaneously are printed out as possible impact points. The program allows for successive choices of prescribed uncertainty, beginning with the most precise and increasing to larger uncertainties. For this purpose, the uncertainty E is employed in a condition test such that

$$(1-E) \leq F = \frac{[(X-X_1)^2+(Y-Y_1)^2]^{1/2}-[(X-X_2)^2+(Y-Y_2)^2]^{1/2}}{V \Delta T_{12}} < (1+E)$$

Mathematically this uncertainty is represented as

$$\text{uncertainty} = \min \ (F(x,y)-1)$$

The physical significance of this procedure is represented in Figure 6.7, in which H_1 is the distance between sensor 1 and the grid point under test, H_2 is the distance between sensor 2 and the same grid point, and H_1' and H_2' are the distances between the known impact point and the respective sensors. From the mathematical development for the impact point (X_p, Y_p),

$$V\Delta T_{12} = [(X_p-X_1)^2 + (Y_p-Y_1)^2]^{1/2} - [(X_p-X_2)^2 + (Y_p-Y_2)^2]^{1/2}$$

If ε is defined as $E \cdot (V\Delta T_{12})$, with E being the chosen uncertainty parameter for the computer test of the grid point (x,y), then a successful detection of the impact point will be reported by the program when

$$V\Delta T_{12} - \varepsilon \leq [(X-X_1)^2+(Y-Y_1)^2]^{1/2}-[(X-X_2)^2+(Y-Y_2)^2]^{1/2}$$

$$\leq V\Delta T_{12} + \varepsilon$$

Thus, if the difference between $(H_1'-H_2')$ and (H_1-H_2) is within the limit ε, then successful detection is reported. An example is provided by the first line of Table 6.4 with E = 0.03:
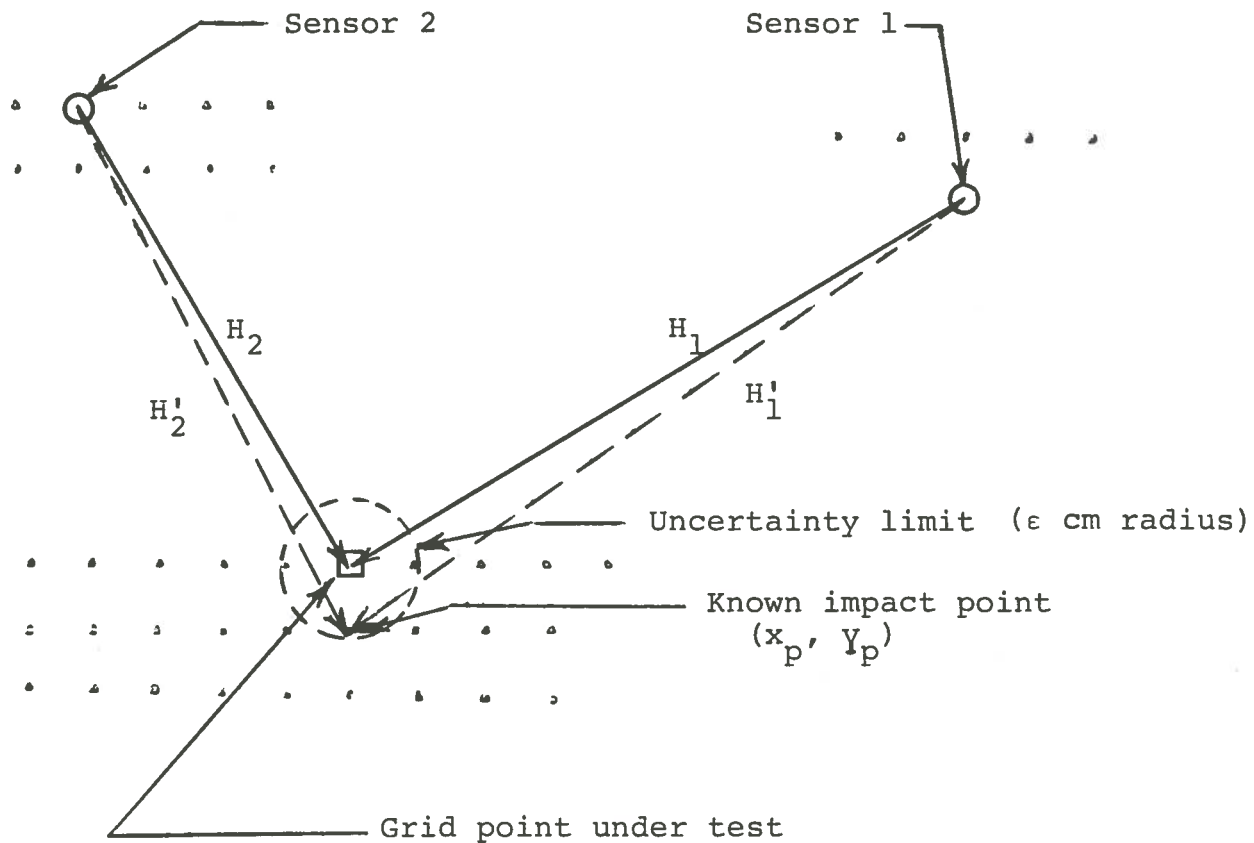
Fig. 6.7. Physical Significance of Uncertainty Limit

"True Location"

$$H_1' = [(X_p-X_1)^2 + (Y_p-Y_1)^2]^{1/2}$$

$$H_2' = [(X_p-X_2)^2 + (Y_p-Y_2)^2]^{1/2}$$

"Grid Location"

$$H_1 = [(X-X_1)^2 + (Y-Y_1)^2]^{1/2}$$

$$H_2 = [(X-X_2)^2 + (Y-Y_2)^2]^{1/2}$$

$$V\Delta T_{12} = 31.6 \text{ cm}, \quad \varepsilon_{12} = 0.948 \text{ cm}$$

$$V\Delta T_{13} = 49.4 \text{ cm}, \quad \varepsilon_{13} = 1.482 \text{ cm}$$

$$V\Delta T_{23} = 17.8, \quad \quad \varepsilon_{23} = 0.534 \text{ cm}$$

and the average linear error for this impact point found by the computer solution is 0.98 cm.

In some cases, the three hyperbolas intersect in two places on the plane of interest. This can be resolved using the sign of one or more ΔT's (i.e., if $\Delta T_{12} < 0$ then $T_2 - T_1 > 0$ which indicates that the impact is closer to detector number 1, but if $\Delta T_{12} < 0$ then impact is closer to detector number 2.

Experimental results are given in Tables 6.4, 6.5, 6.6, and 6.7 for the vessel full and half full of water each time for noise-free and boiling conditions respectively. In these tables "error area" expresses how close the computational impact location is to actual impact coordinates, and is defined as the product of the difference in X-coordinates times the difference in Y-coordinates as shown in Figure 6.8. The fraction of the error area to the total vessel area under consideration is defined as "fraction".

An important conclusion which may be drawn from the experimental data is that an impact point must be farther than 7.5 inches from the closest sensor in the array. At distances closer than this, ΔT values were spurious, and

Table 6.4.   Results of impact location using ΔT method on the vessel full of water
            with no boiling.

Impact Coordinates (cm)		Signal Arrival	Time Difference Measured (μsec)			Impact Location (cm)		Uncertainty[a]	Error Area (cm²)	Fraction
X	Y		ΔT_{12}	ΔT_{13}	ΔT_{23}	X	Y			
60.96	33.02	415	55	86	31	62.0	35.5	.03	2.57	7.5 E-05
60.96	58.42	451	65	84	19	60.5	60.5	.03	.956	2.78E-05
60.96	83.82	451	12	79	67	62.5	87	.03	7.97	2.32E-04
91.44	33.02	154	46	49	3	92.5	35	.09	2.09	6.10E-05
91.44	58.42	514	29	42	13	92.5	61	.03	2.73	7.95E-05
91.44	83.82	541	81	91	10	92.5	85.5	.03	1.78	5.18E-05
121.92	31.75	153	891	966	75	NF[b]				
121.92	50.8	513	6	106	100	NF		>.4		
121.92	69.85	513	85	145	60	NF				
152.4	33.02	153	46	47	1	151.5	33.5	.07	.432	1.25E-05
152.4	58.42	513	35	39	4	155	60	.29	4.10	1.19E-04
152.4	83.82	531	88	103	15	151.4	89.5	.07	5.11	1.48E-04
182.88	33.02	315	66	87	21	183	40	.03	1.25	3.65E-05
182.88	58.42	351	63	92	29	184	65	.09	7.76	2.25E-04
182.88	83.82	351	19	97	78	182	86	.19	1.78	5.20E-05
213.36	33.02	312	155	158	3	NF		>.4		
213.36	73.66	356	117	132	15	NF		>.4		
243.84	33.02	326	66	100	34	240.5	32	.009	3.40	9.91E-05
243.84	58.42	362	77	90	13	240.5	58	.03	1.40	4.08E-05
243.84	83.82	362	26	95	69	242	87	.09	5.85	1.70E-04
274.32	33.02	236	41	46	5	273	33.5	.05	.633	1.84E-05
274.32	58.42	623	31	41	10	274.5	61.5	.03	.554	1.61E-05
274.32	83.82	632	84	96	12	275.5	88.5	.03	.5.52	1.60E-04
304.8	31.75	263	61	136	75	NF		>.4		
304.8	50.8	623	12	110	98	NF				
304.8	69.85	624	87	152	65	NF		>.4		
335.28	33.02	264	41	52	11	332	36.5	.03	11.41	3.32E-04
335.28	58.42	624	35	50	15	332.5	63	.03	12.73	3.70E-04
335.28	83.82	642	90	104	14	333.5	93	.03	16.34	4.75E-04
365.76	33.02	426	52	82	30	363.5	35.5	.01	5.60	1.63E-04
365.76	58.42	462	50	79	29	363	63	.17	12.69	3.67E-04
365.76	83.82	462	7	86	79	363	90	.11	17.05	4.96E-04
396.24	33.02	412	151	157	6	NF				
396.24	73.66	456	128	130	2	NF				

[a] See text for meaning

[b] NF = not found by computation with ± 40% error.

Table 6.5. Results of impact location using ΔT method on the vessel full of water with boiling.

Impact Coordinates (cm)		Signal Arrival	Time Difference Measured (μsec)			Impact Location (cm)		Uncertainty (a)	Error Area (cm²)	Fraction
X	Y		ΔT_{12}	ΔT_{13}	ΔT_{23}	X	Y			
60.96	33.02	415	54	94	40	60.5	30	.03	1.38	4.04E-05
60.96	58.42	451	65	77	12	61.5	57	.03	.766	2.23E-05
60.96	83.82	451	22	82	60	62	83.5	.03	.33	9.68E-06
91.44	33.02	145	50	54	4	91.5	31	.07	.1211	3.52E-06
91.44	58.42	514	28	42	14	92.5	60.5	.05	2.20	6.41E-05
91.44	83.82	541	81	91	10	92.5	85.5	.03	1.78	5.18E-05
121.92	31.75	153	65	138	73	NF (b)				
121.92	50.8	513	11	104	93	NF		>.4		
121.92	69.85	513	85	145	60	NF				
152.4	33.02	135	46	46	0	152.5	34.5	.03	.148	4.30E-06
152.4	58.42	513	35	45	10	151.5	63	.03	4.12	1.19E-04
152.4	83.82	531	88	103	15	151.5	89.5	.07	5.11	1.48E-04
182.88	33.02	315	65	93	28	184	35.5	.03	2.92	8.51E-05
182.88	58.42	351	67	88	21	185	62	.03	7.8	2.27E-04
182.88	83.82	351	21	102	81	183.5	89.5	.17	3.86	1.12E-04
213.36	33.02	312	155	168	13	NF		>.4		
213.36	73.66	356	125	149	24	NF		>.4		
243.84	33.02	326	73	108	35	238	31	.01	11.79	3.43E-04
243.84	58.42	362	83	98	15	238.5	59	.03	3.09	9.01E-05
243.84	83.82	362	28	98	70	241.5	87	.11	7.44	2.16E-04
274.32	33.02	236	47	53	6	273.5	31.5	.03	1.24	3.62E-05
274.32	58.42	623	24	33	9	273.5	59.5	.05	.88	2.57E-05
274.32	83.82	632	75	89	14	274	86.5	.03	.85	2.49E-05
304.8	31.75	263	68	136	68	NF		>.4		
304.8	50.8	623	4	102	98	NF				
304.8	69.85	623	76	144	68	NF		>.4		
335.28	33.02	234	0	0	0	NF				
335.28	58.42	625	36	222	186	NF				
335.28	83.82	625	97	242	145	NF				
365.76	33.02	426	63	98	35	368.5	31.5	.01	4.16	1.21E-04
365.76	58.42	462	64	94	30	364.5	63	.21	5.77	1.67E-04
365.76	83.82	462	14	95	81	365	90	.15	4.69	1.36E-04
396.24	33.02	412	155	161	6	NF				
396.24	73.66	456	131	134	3	NF				

(a) See text for meaning

(b) NF = not found computation with ± 40% error

Table 6.6. Results of impact location using ΔT method on the vessel half way water with no boiling.

Impact Coordinates (cm)		Signal Arrival	Time Difference Measured (μsec)			Impact Location (cm)		Uncertainty(a)	Error Area (cm²)	Fraction
X	Y		ΔT_{12}	ΔT_{13}	ΔT_{23}	X	Y			
60.96	33.02	415	54	93	39	61	30.5	.03	.101	2.93E-06
60.96	58.42	451	59	78	19	61.5	60.5	.03	1.12	3.96E-05
60.96	83.82	451	15	80	65	62	88	.03	4.34	1.26E-04
91.44	33.02	145	51	55	4	92	30	.05	1.69	4.91E-05
91.44	58.42	514	27	40	13	92	60	.03	.88	2.57E-05
91.44	83.82	541	81	91	10	92.5 (b)	85	.03	1.25	3.63E-05
121.92	31.75	153	1852	1927	75	NF (b)				
121.92	50.8	153	662	769	107	NF				
121.92	69.85	513	82	144	62	NF				
152.4	33.02	153	46	55	9	149	34.5	.05	5.03	1.46E-04
152.4	58.42	513	36	46	10	151.5	63	.05	4.12	1.19E-04
152.4	83.82	531	88	103	15	151.5	89.5	.07	5.11	1.48E-04
182.88	33.02	315	65	85	20	84	35.5	.03	2.92	8.51E-05
182.88	58.42	351	60	91	31	185.5	62	.03	9.59	2.79E-04
182.88	83.82	351	20	97	77	184	89.5	.09	6.70	1.94E-04
213.36	33.02	312	155	156	1	NF		>.4		
213.36	73.66	356	119	135	16	NF		>.4		
243.84	33.02	326	63	101	38	241	30.5	.029	7.15	2.08E-04
243.84	58.42	362	76	88	12	241.5	57	.03	3.32	9.66E-05
243.84	83.82	362	34	94	60	239	86.5	.01	12.97	3.77E-04
274.32	33.02	236	49	52	3	276	33.5	.07	.807	2.34E-05
274.32	58.42	623	28	40	12	275	60.5	.05	1.41	4.11E-05
274.32	83.82	632	83	95	12	275.5	88.5	.01	5.52	1.60E-04
304.8	31.75	263	66	142	76	NF		>.4		
304.8	50.8	623	13	111	98	NF				
304.8	69.85	624	83	151	68	NF		>.4		
335.28	33.02	264	49	54	5	332.5	34	.05	2.23	6.50E-05
335.28	58.42	624	34	50	16	332.5	62.5	.03	11.34	3.29E-04
335.28	83.82	642	92	102	10	332.5	90.5	.03	18.57	5.40E-04
365.76	33.02	426	53	82	29	364	35.5	.03	4.36	1.29E-04
365.76	58.42	462	49	79	30	362	63	.19	17.22	5.00E-04
365.76	83.82	462	7	84	77	363	90	.09	17.05	4.96E-04
396.24	33.02	412	146	161	15	NF				
396.24	73.66	465	131	136	5	NF				

(a) See text for meaning

(b) NF = not found for computation with ± 40% error

Table 6.7. Results of impact location using AT method on the vessel half way water with boiling.

Impact Coordinates (cm)		Signal Arrival	Time Difference Measured (usec)			Impact Location (cm)		Uncertainty[a]	Error Area (cm²)	Fraction
X	Y		ΔT_{12}	ΔT_{13}	ΔT_{23}	X	Y			
60.96	33.02	415	54	94	40	60.5	30	.03	1.38	4.04E-05
60.96	58.42	451	67	78	11	61.5	56.5	.03	1.03	3.01E-05
60.96	83.82	451	24	81	57	61.5	83	.03	.44	1.28E-05
91.44	33.02	154	57	66	9	95	33.5	.13	1.70	4.97E-05
91.44	58.42	514	21	34	13	91.5	58	.05	2.51	7.33E-07
91.44	83.82	541	79	89	10	92.5	85	.03	1.25	3.63E-05
121.92	31.75	153	1166	1232	66	NF[b]				
121.92	50.8	513	3	98	95	NF		>.4		
121.92	69.85	513	83	145	62	NF				
152.4	33.02	135	52	53	1	151	32.5	.05	.727	2.11E-05
152.4	58.42	513	34	45	11	151.5	62.5	.03	3.67	1.06E-04
152.4	83.82	531	87	102	15	152	89.5	.07	2.27	6.6 E-05
182.88	33.02	315	65	94	29	183.5	40	.03	4.74	1.38E-04
182.88	58.42	351	69	90	21	183	65	.13	1.18	3.44E-05
182.88	83.82	351	21	95	74	184	89.5	.1	6.70	1.94E-04
213.36	33.02	312	154	156	2	NF		>.4		
213.36	73.66	356	126	134	8	NF		>.4		
243.84	33.02	326	62	99	37	241	30.5	.01	7.15	2.08E-04
243.84	58.42	362	75	87	12	242	57	.03	2.61	7.60E-05
243.84	83.82	362	33	93	60	240	85.5	.01	6.45	1.87E-04
274.32	33.02	236	49	53	4	274	32	.03	.326	9.49E-06
274.32	58.42	623	22	33	11	273.5	58.5	.05	6.56	1.90E-06
274.32	83.82	632	88	93	5	274.5	87	.03	.572	1.66E-05
304.8	31.75	263	72	141	69	NF		>.4		
304.8	50.8	623	3	102	99	NF				
304.8	69.85	623	82	151	69	NF		>.4		
335.28	33.02	264	49	53	4	333.5	34	.05	1.74	5.07E-05
335.28	58.42	624	26	43	17	333.5	59.5	.03	1.92	5.59E-05
335.28	83.82	642	88	100	12	333.5	90.5	.03	11.89	3.45E-04
365.76	33.02	426	52	82	30	363.5	35.5	.01	5.60	1.63E-04
365.76	58.42	462	57	78	21	365	61.5	.03	2.34	6.80E-05
365.76	83.82	462	15	86	71	365.5	90	.05	1.60	4.67E-05
396.24	33.02	412	150	154	4	NF				
396.24	73.66	465	143	147	4	NF				

[a] See text for meaning

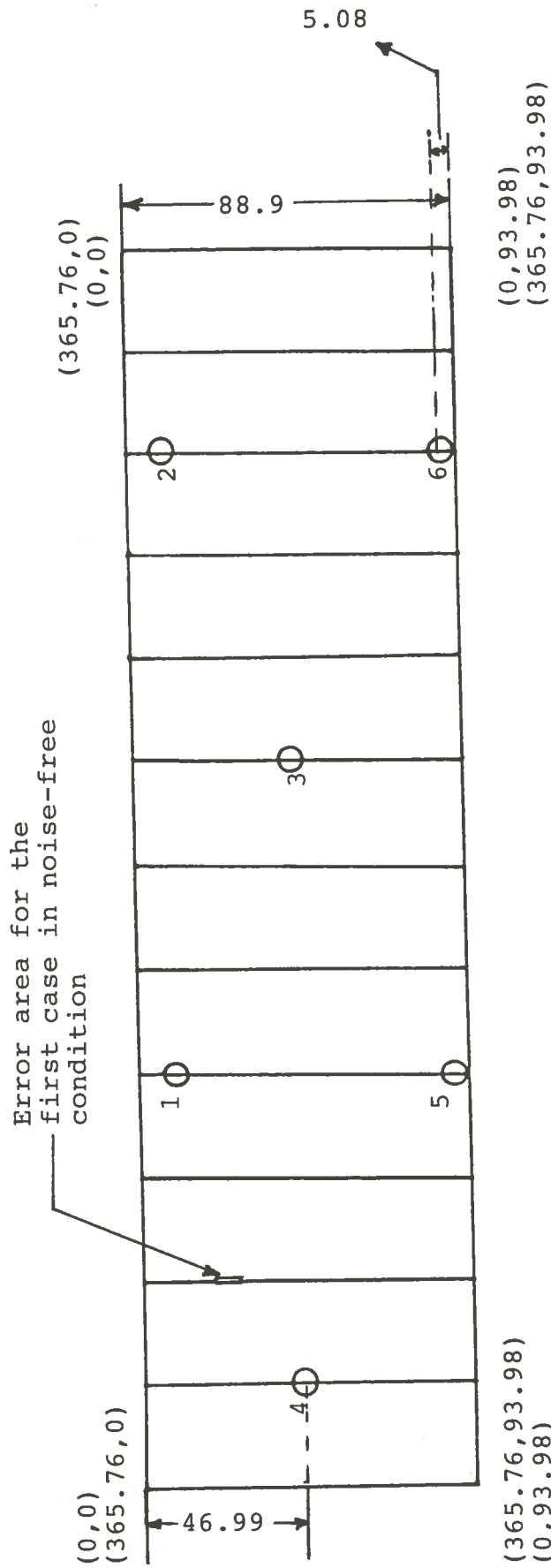[b] NF = not found for computation with ± 40% error

Fig. 6.8. The error area with respect to total area

location calculation was meaningless. This minimum impact-to-detector distance is considered to be a characteristic of the particular sensor type and measurement system, and would be expected to have some other value for another system.

The magnitudes of the uncertainties associated with impact-point location can be affected by such parameters and conditions as

1. the experimental velocity measurement

2. angle of impact

3. material irregularity

4. sensor position

5. damping by platform, wood between pipe and tank, pitting, welding, and top collar

In principle, the more nearly equal the distance from impact-point to all sensors becomes, the more precise the location calculation should become. This is expected because all errors should be essentially equal, and no one error will dominate when they are combined into a cumulative error term. Figure 6.9 is a plot of uncertainty as a function of minimum impact-sensor distance, from which no convincing minimum can be discerned. The only influence of distance therefore appears to be a failure of the method to detect an impact too close to the nearest sensor. Additional factors from the list given above may introduce large errors which are not directly related to distance.
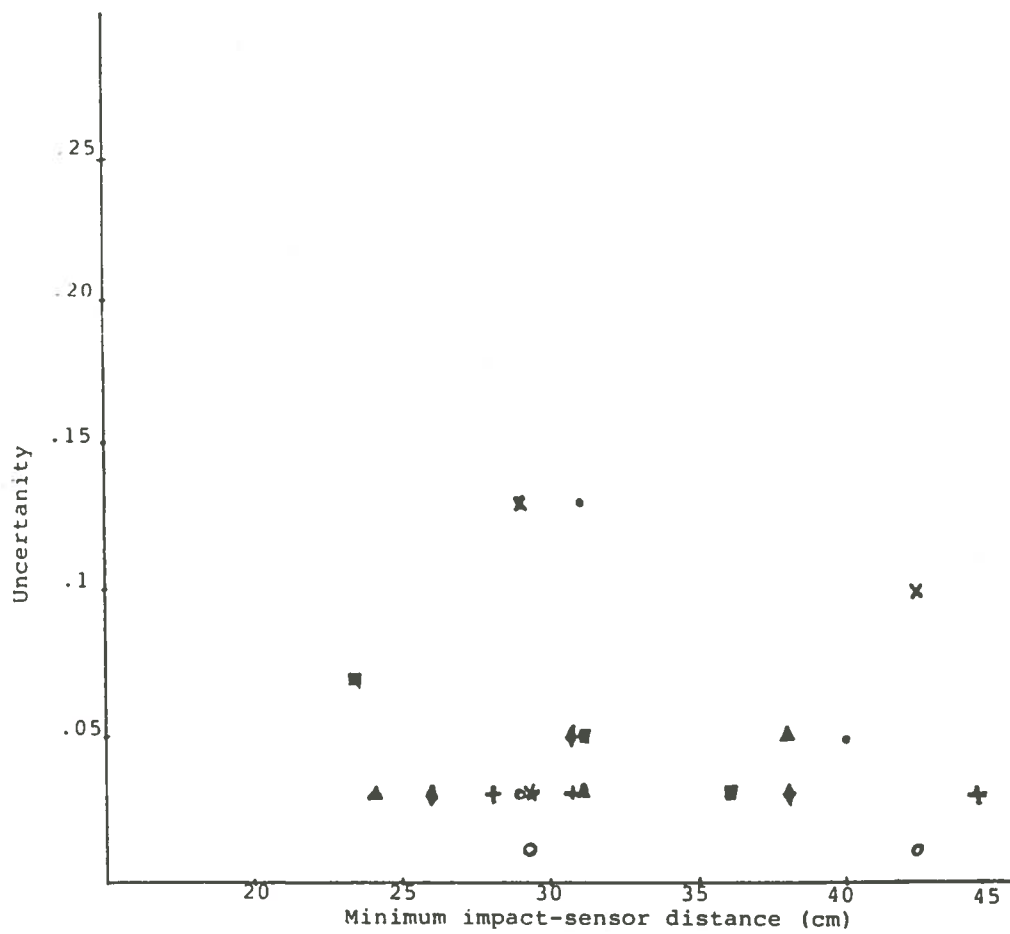
Fig. 6.9. Uncertanity versus minimum impact-sensor distance

Isolation of parameters and conditions which have major influence uncertainty in impact location was considered as being beyond the scope and objective of this thesis. Specific experiments with more sensitive and reliable equipment will be required for this aspect of loose parts monitoring simulation tests.

In a nonideal case when the impact is too close to one sensor, the equipment fails in measuring ΔT's. To overcome this problem, at least four sensors are required to find the impact point. The condition is such that the distance between any two sensors should be greater than twice the minimum useful distance to a sensor so that if one sensor fails to perform the other three sensors measure ΔT's correctly.

Apollonian Construction Procedure[23]

This method was applied to a point with coordinates (60.96, 33.02) for the vessel full of water with boiling condition. Figure 6.10 shows this type of construction. This construction locates the center of a circle which passes through a fixed point (the third sensor position) and is tangent to two given circles (each with a radius equal to $V*\Delta T$). The impact location is the center of this circle. This circle intersects one of the given circles in two points. The reason for this may come from any of

$$R_{51} = v*DT_{51} = 30*v = 16.35$$
$$R_{41} = v*DT_{41} = 54*v = 29.5$$

Impact location
(60.5,29)

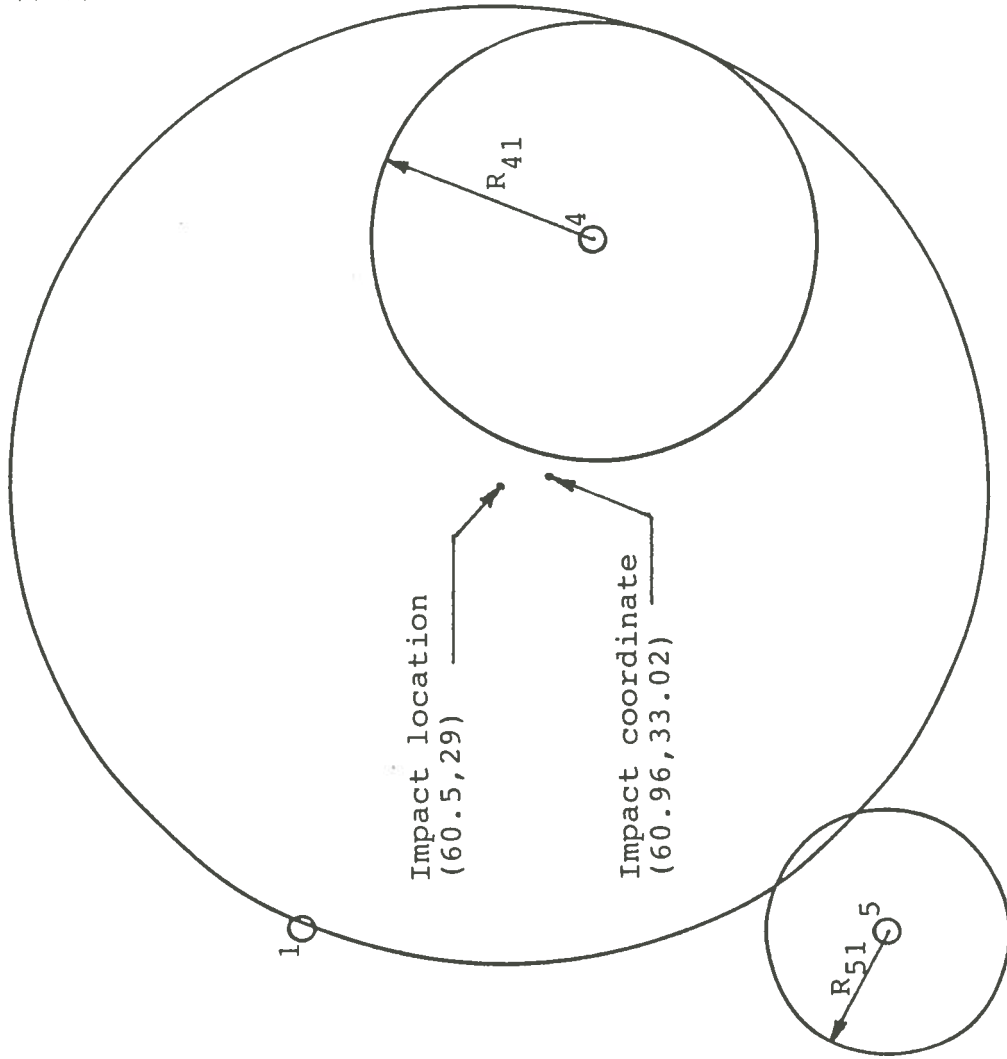Impact coordinate
(60.96,33.02)

R_{41}

R_{51}

Fig. 6.10. Apollonian method of impact location

the parameters and conditions listed before. This method is very slow and impractical for impact location in industry.

Chapter 7

LOOSE PARTS JOURNEY IN A BWR/6

The preceding experimental verification of impact location with good precision even in the presence of simulated boiling noise provides encouragement for analysis of possible journeys of loose parts in a BWR/6 reactor vessel. Loose parts monitoring and parts journeys through external flow loops is considered as a separate problem, and was not undertaken here.

In any reactor, great care is taken to remove and prevent any object from entering the reactor system through strictly controlled operating and startup procedures. However there exists the possibility, remote as it may seem, that some object could either escape detection or break loose from the vessel internals. Such an object may fall anywhere in the vessel depending on its size, weight, and shape. It is very unlikely to have a loose part sitting on the steam dryer assembly but it can be left undetected inside the system of troughs. This object may either lodge in the flow path or it might be carried by flow and drains to the pool surrounding the separators and then into the recirculation downcomer annulus between the core shroud and reactor vessel wall as shown in Figure 7.1. Any object that breaks loose
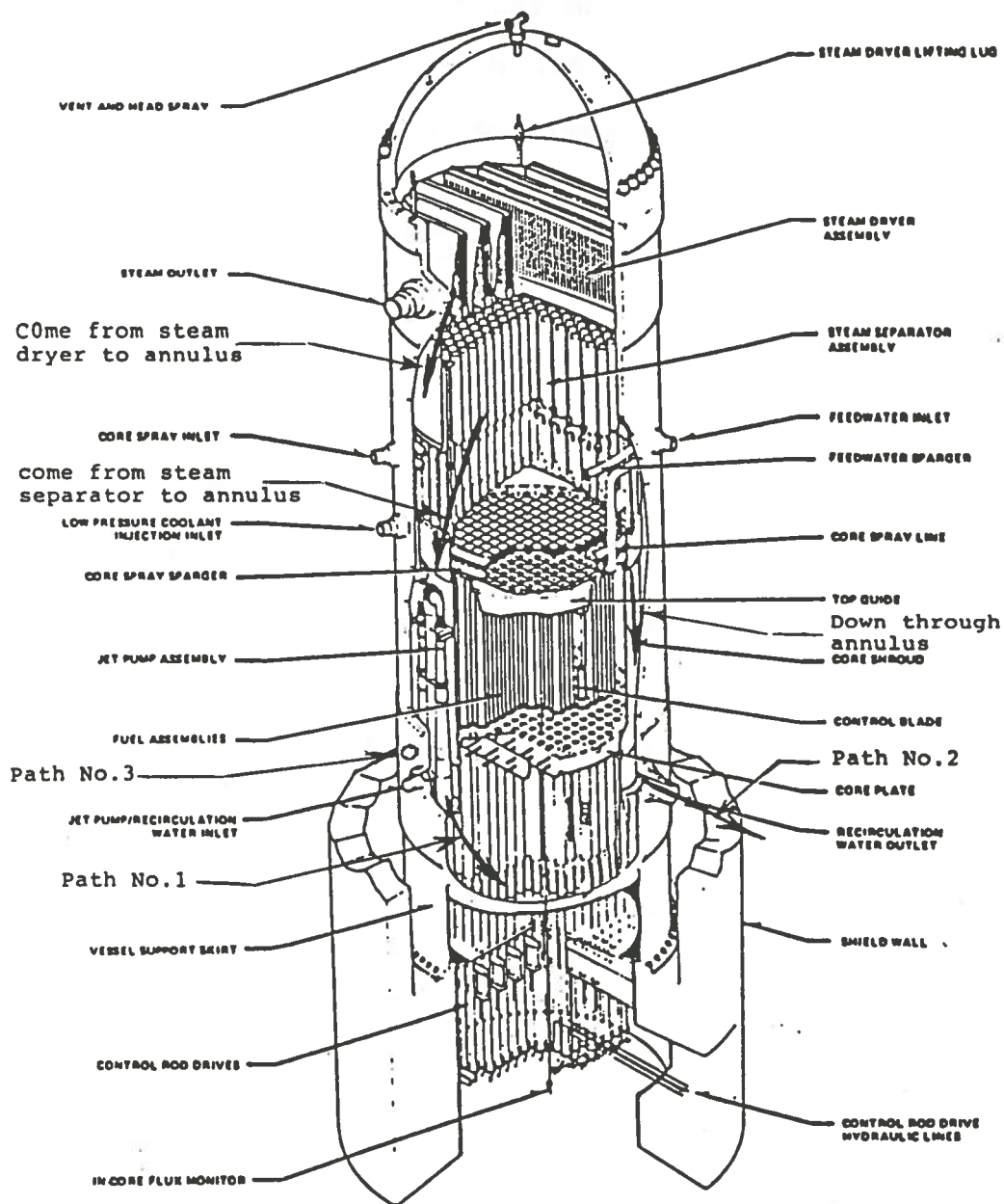
Fig.7.1 Loose part journey in a BWR/6

within the steam separator assembly may float on the water
or fall down on the upper shroud. Such an object will
slide down into the annulus between the core shroud and
vessel wall. This object would travel in any of these
three paths: 1) it can make its way into the lower plenum
through the jet pumps that have a typical nozzle diameter
of 1.3 inches with the throat diameter of 6 inches, 2) it
also can go into the 20 inch reactor recirculation outlet
to the suction of the reactor recirculation pumps, or 3)
it may end up sitting on the baffle plate. Once the
object enters the lower plenum (if it was not there to
begin with), it would tend to drift toward the vessel
centerline where horizontal velocities are low and the
boundary layers on the vessel may be thicker than the
object[9] as shown in Figure 7.2. Thus, the boundary-layer
effect would reduce the capability of the fluid to sweep
the piece up off the floor or the vessel so that the
vertical velocity components could carry it upward. Even
if the objects were somehow swept upward, it seems unlikely
to pass through an orifice and then through the lower tie
plate nosepiece and the lower tie plate to enter into the
fuel channel; (this would require very unlikely situation
of alignment of the object and passage through holes of
only 0.410 inch diameter). Even if the object somehow
swept upward into a fuel channel, it would be stopped by

Jet pump

Control rod
drive

Fig.7.2. Flow in the lower plenum

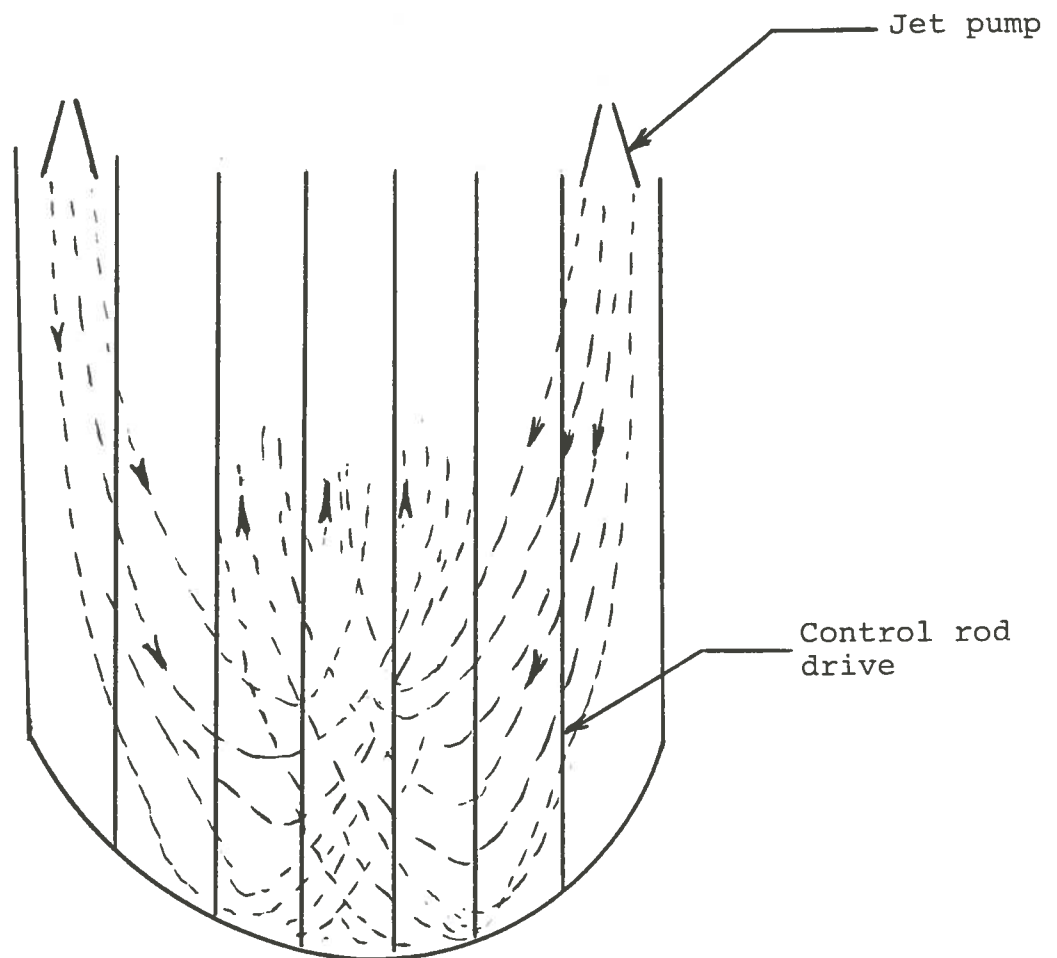the first spacer. So no object can enter the core unless through water rods* or it was there to begin with. This object must be small (<.55 inch dia.) to enter the upper plenum, and even smaller (<.14 inch dia.) to jam the control rod. As a result, the lower plenum of the vessel is the most likely place for a loose part in the primary system to end up.

---

* See text for description of water rod

Chapter 8

FAILURE OF COMPONENT FROM
LOOSE PART IMPACT
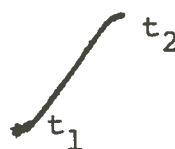
A. Introduction to Impact

Impact refers to the collision between two bodies
and is characterized by the generation of relatively
large contact forces which act over a very short interval
of time. The theory of impact is based primarily on the
impulse-momentum law for rigid bodies and is limited to
a specification of the initial and terminal velocity
states of the objects and the applied linear or angular
impulse.[24] Consider motion of a particle of mass m in space.
The resultant Σ_F of all forces on m is in the direction
of its acceleration $\dot{v}$. The basic equation of motion by
Newton's Law

$$\Sigma_F = m\dot{v} = \frac{d}{dt}(mv)$$

$$\Sigma_F = \frac{d}{dt}(G) = \dot{G} \tag{8.1}$$

The effect of resultant force Σ_F on the linear momentum
of the particle over a finite period of time can be found
simply by integrating Eq. 8.1 with respect to time t.

$$\int_{t_1}^{t_2} \Sigma_F \, dt = G_2 - G_1$$

where the linear momentum at time t_2 is $G_2 = mv_2$ and the linear momentum at time t_1 is $G_1 = mv_1$.

In addition to the equation of linear impulse, there exists a parallel set of equations for angular impulse. In Figure 8.1, the moment of the linear momentum vector mv about the origin O is defined as the angular momentum H_O of P about O and is given by the cross-product relation for the moment of a vector. The scalar components of angular momentum may be obtained from the expansion

$$H_O = r \times mv = im(V_z y - V_y z) + jm(V_x z - V_z x)$$

$$+ km(V_y x - V_x y) \tag{8.2}$$

or

$$H_O = m \begin{vmatrix} i & j & k \\ x & y & z \\ V_x & V_y & V_z \end{vmatrix}$$

so that

$$H_x = m(V_z y - V_y z), \quad H_y = m(V_y z - V_z x),$$

$$H_z = m(V_y x - V_x y)$$

Now, consider the moment of Σ_F all forces acting on the particle P about the origin O is

$$\Sigma M_O = r \times \Sigma F = r \times m\dot{v}$$

where Newton's second law $F = m\dot{v}$ has been substituted.
We now differentiate Eq. 8.2 with time, using the rule
for the differentiation of a cross product and get

$$\dot{H}_O = \dot{r} \times mv + r \times m\dot{v} = v \times mv + r \times m\dot{v}$$

The term $v \times mv$ is zero since the cross product of equal and,
hence, parallel vectors is identically zero. Substituting
into the expression for ΣM_O gives

$$\Sigma M_O = \dot{H}_O \qquad (8.3)$$

This equation states that the moment about the fixed
point 0 of all forces acting on m equals the time rate of
change of angular momentum of m about 0. To obtain the
effect of the moment ΣM_O on the angular momentum of the
particle over a finite period of time, Eq. 8.3 may be
integrated from t_1 to t_2.

$$\int_{t_1}^{t_2} \Sigma M_O dt = H_{O_2} - H_{O_1} \qquad (8.4)$$

where $H_{O_2} = r_2 \times mv_2$ and $H_{O_1} = r_1 \times mv_1$. The product of
moment and time is defined as angular impulse, and Eq.
8.4 states that the total angular impulse on m about the
fixed point 0 equals the corresponding change in angular
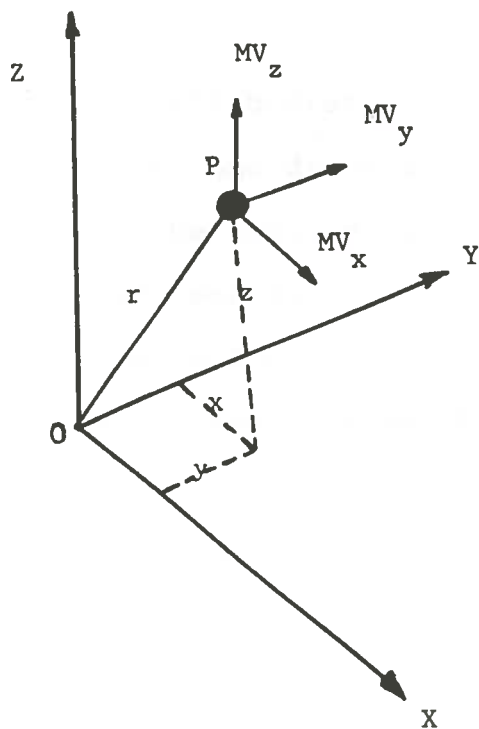momentum of m about 0. The general impulse momentum

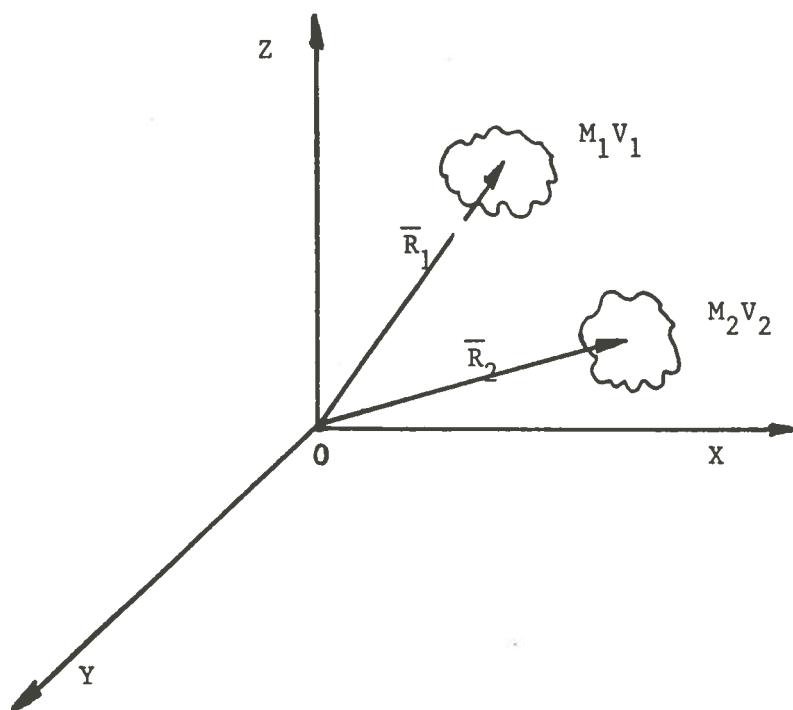Fig. 8.1. Linear momentum of a particle in space
(Redrawn from Meriam[24])

Fig. 8. 2. Coordinates of two moving particles
(Redrawn from Shahrakhi[25])

relation is applicable to all bodies. Since only normal impact is of interest here, one dimensional impact theory is sufficient. Moreover, the impulse momentum relations are written for rigid-body models.

Consider particles m_1 and m_2 with velocities v_1 and v_2 as shown in Figure 8.2. Inasmuch as the contact forces are equal and opposite during impact, the linear momentum of the system remains unchanged. By conservation of linear momentum:[25]

$$m_1 v_1 + m_2 v_2 = m_1 v_1' + m_2 v_2'$$

Following contact, a short period of deformation takes place until the contact area between them ceases to increase. At this instant both particles are moving with the same velocity v_o. During the remainder of contact, a period of restoration occurs lasting until the contact area reduces to zero. A commonly used parameter in this type of analysis is the coefficient of restitution e which can be expressed by the ratio of the magnitude of the restoration impulse to the magnitude of the deformation impulse. F_r and F_d represent the magnitudes of the contact forces during the restoration and deformation periods, respectively, as shown in Figure 8.3; the impact forces vary from zero to their peak value during the deformation portion of the impact and again back to zero
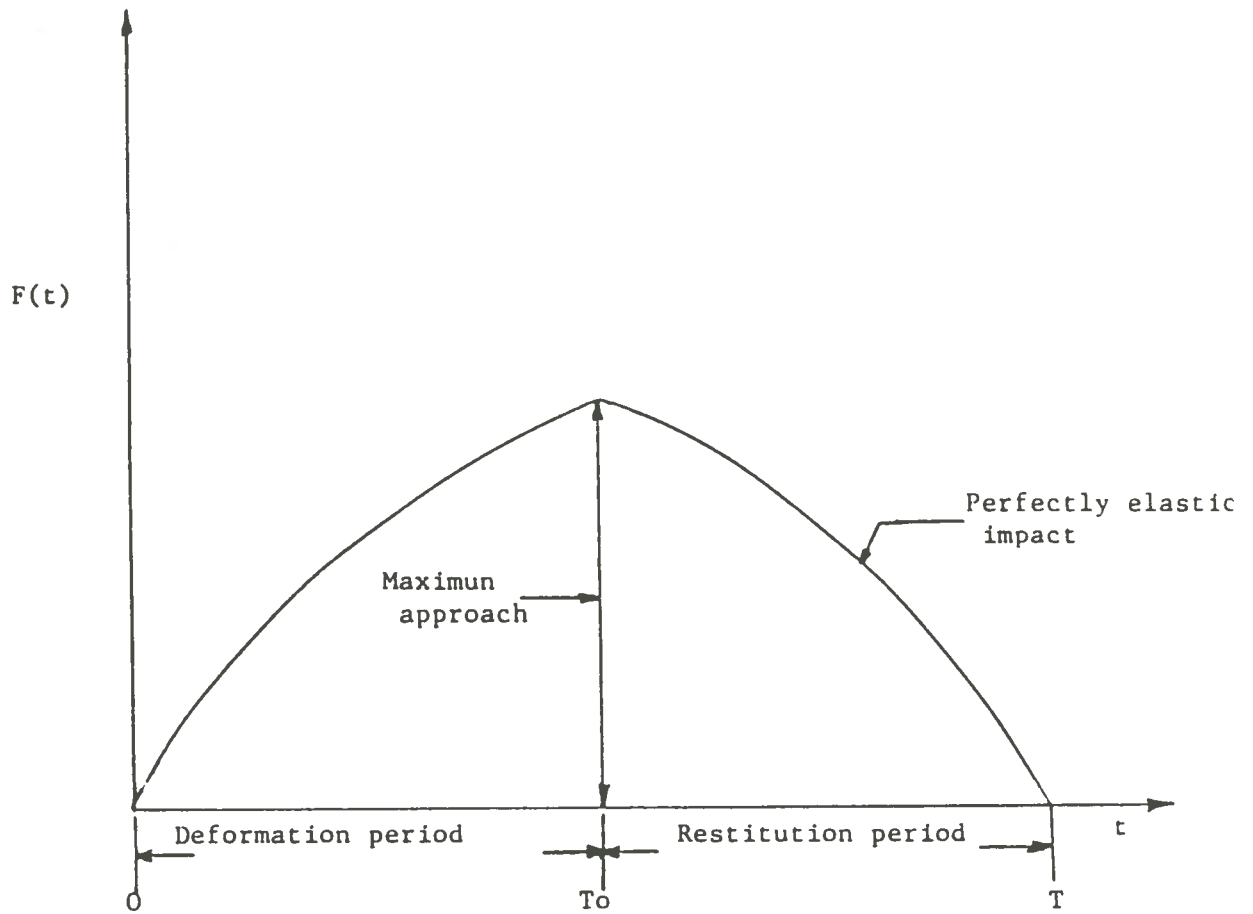
Fig. 8.3. Time dependent force during impact

during the restoration period. For particle 1 the definition of e together with the impulse-momentum equation gives us

$$e = \frac{\int_{t_o}^{t} F_r dt}{\int_{o}^{t_o} F_d dt} = \frac{m_1(-V_1' - [-V_o])}{m_1(-V_o - [-V_1])} = \frac{V_o - V_1'}{V_1 - V_o}$$

(8.5)

Similarly for particle 2 we have

$$e = \frac{\int_{t_o}^{t} F_r dt}{\int_{o}^{t_o} F_d dt} = \frac{m_2(V_2' - V_o)}{m_2(V_o - V_2)} = \frac{V_2' - V_o}{V_o - V_2}$$

The time for the deformation is taken as t_o and the total time of contact is t. Eliminating V_o between the two expressions for e gives us:

$$e = \frac{V_2' - V_1'}{V_1 - V_2} = \frac{\text{relative velocity of separation}}{\text{relative velocity of approach}}$$

According to the theory of impact the value $e = 1$ means that the capacity of the two particles to recover equals their tendency to deform. This condition is one of elastic impact with no energy loss. The value $e = 0$, on the other hand, describes inelastic or plastic impact where the particles cling together after collision and the loss of energy is a maximum.

Using the previous definitions, the collision of two non-rotating bodies can be classified as:[26]

1. Residual velocities

$$V_1' = V_1 - (1 + e) \frac{m_2 V_1 - m_2 V_2}{m_1 + m_2}$$

$$V_2' = V_2 - (1 + e) \frac{m_1 V_1 - m_1 V_1}{m_1 + m_2} \qquad (8.6)$$

2. Kinetic energy

The loss of kinetic energy in the system is given by:

$$\Delta k = \frac{1}{2} \left(\frac{m_1 m_2}{m_1 + m_2}\right) (1 - e^2) (V_1 - V_2)^2 \qquad (8.7)$$

The energy loss vanishes for the impact of completely elastic bodies, when $e = 1$.

3. Impulse quantity

The total impulse delivered to either body 1 or 2 is the change in the momentum:

$$\Delta G = (1 + e) \frac{m_1 m_2}{m_1 + m_2} (V_1 - V_2) \qquad (8.8)$$

Consider a one-dimensional impact problem described above and a target of mass M_T (reactor vessel) and a loose

part of mass M_L. Given the initial velocity of the vessel to be zero. The residual loose part and vessel velocities V_L, V_T are given by:

$$V_L = \frac{M_L - eM_T}{M_L + M_T} V_O$$

$$V_T = (1 + e) \left(\frac{M_L}{M_L + M_T}\right) V_O \qquad (8.9)$$

The total impulse transferred to the vessel is given by:

$$G = \frac{1 + e}{1 + \phi} M_L V_O = \frac{1 + e}{1 + \phi} G_{INIT} \qquad (8.10)$$

where

$$\phi = M_L / M_T$$

V_O = loose part velocity before impact

G_{INIT} = loose part potential impulse.

The total energy delivered to the vessel due to impact is given by:

$$E_T = \frac{1}{2} M_T V_T^2$$

$$= \frac{1}{2} M_L V_O^2 \left[\frac{1}{\phi} \left(\frac{1 + e}{1 + 1/\phi}\right)^2\right]$$

$$= E_{INIT} \left[\phi \left(\frac{1 - e}{1 + \phi}\right)^2\right] \qquad (8.11)$$

where E_{INIT} is the initial energy of the loose part.

Damage in Material Due to Low Velocity Impact[27]

The approach in studying the response of isotropic materials to low velocity impact is shown in Figure 8.4. The three major steps of the approach are: (1) determination of impactor-induced surface pressure and its distribution, (2) determination of internal stresses in the composite target caused by the surface pressure, and (3) determination of failure modes in the target caused by the internal stresses. For the most general case the target is assumed to be a multilayer. It is assumed that (1) the target and the impactor are linear elastic, (2) impact duration is long compared to stress-wave transit times in the impactor (or target of finite thickness), and (3) the impact is normal to the target surface. These assumptions are valid for failure analysis of reactor components from loose part impact.

Pressure Distribution

Spherical Impactor, Isotropic Target. Denoting the mass and the velocity of the impactor as m_1 and v_1, respectively and the target mass and its velocity as m_2 and v_2, the rates of change of velocity during impact (as the two bodies come in contact) are

$$m_1 \frac{dv_1}{dt} = -P, \quad m_2 \frac{dv_2}{dt} = -P \tag{8.12}$$

Impactor

Impact causes
pressure (pressure
is time dependent)

Pressure cause
stresses

Stresses cause
failure
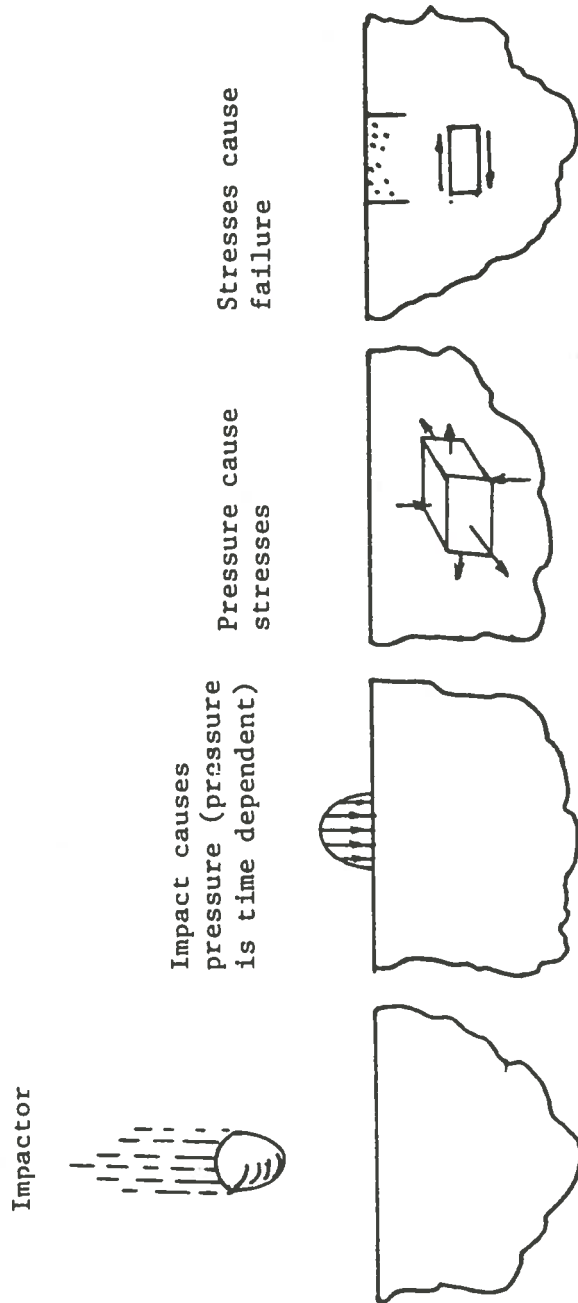
Fig. 8.4. Essential feature of the approach
(Redrawn from Zukas[27])

where P is the contact force

If we denote by α the distance that the impactor and the target approach one another because of local compression at the point contact, the velocity of this approach is

$$\dot{\alpha} = v_1 + v_2 \qquad (8.13)$$

Results obtained by Rayleigh (1906)[27] shows that if the contact duration between the impactor and the target is very long in comparison with their natural periods, vibrations of the system can be neglected. It can therefore be assumed that the Hertz law

$$P = n \; \alpha^{3/2} \qquad (8.14)$$

established for statical conditions, applies also during impact. The term n is defined as

$$n = \frac{4 \; (R_1)^{1/2}}{3\pi(k_1 + k_2)} \qquad (8.15)$$

where R_1 is the radius of a spherical impactor or indenter,

$$k = \frac{1 - \mu_1^2}{\pi E_1} \qquad (8.16)$$

$$k_2 = \frac{1 - \mu_1^2}{\pi E_2} \qquad (8.17)$$

where E and μ are the Young's modulus and Poisson's ratio respectively, and the subscripts 1 and 2 refer to the

impactor and the target. Differentiation, combination, and substitution of the resultant equation yields

$$\ddot{\alpha} = n \, M \, a^{3/2} \qquad (8.18)$$

where

$$M = \frac{1}{m_1} + \frac{1}{m_2} \qquad (8.19)$$

if both sides of (8.18) are multiplied by α and the resultant equation is integrated the following results:

$$(\dot{\alpha}^2 - v^2) = -\frac{4}{5} \, M \, n \, \alpha^{5/2} \qquad (8.20)$$

where v is the approach velocity of the two bodies at $t = 0$, that is, at the beginning of impact. Maximum deformation, α_1, occurs when $\dot{\alpha} = 0$ and is

$$\alpha_1 = (\frac{5v^2}{4Mn})^{2/5} \qquad (8.21)$$

An alternate way of arriving at relationship given by (8.21) is to start with the energy balance of the system. Assuming that the target is seminfinite and stationary and the impactor is moving at velocity, v_1, the energy balance becomes

$$\frac{1}{2}m_1 v_1^2 = \int_0^{\alpha_1} P \, d\alpha \qquad (8.22)$$

Substitution of Eq. (8.14) into Eq. (8.22) followed by evaluation of the resulting integral gives

$$\frac{1}{2}m_1 v_1 = \frac{2}{5} n \ \alpha_1^{5/2} \tag{8.23}$$

which when solved for α_1 is identical to the result given by Eq. (8.21). It is noted that in this case, $v_1 \equiv v$ and $M \equiv 1/m_1$. Substitution of Eq. (8.21) into Eq. (8.14) gives the following final realtionship

$$P = n^{2/5} \ (\frac{5v^2}{4M})^{3/5} \tag{8.24}$$

For the case of the Hertzian contact problem involving a sphere pressed onto a flat surface by a force P, the relationship between P and a, the radius of the area of contact is

$$a = [\frac{3\pi P}{4} (k_1 + k_2) R_1]^{1/3} \tag{8.25}$$

Combining Eq. (8.25) and Eq. (8.24), the maximum radius of the area of contact between a flat target and a spherical impactor then becomes

$$a = (R_1)^{1/2} \ (\frac{5v^2}{4Mn})^{1/5} \tag{8.26}$$

It has been shown that the pressure distribution over the area of contact is

$$q_{x,y} = q_0 \left[1 - \frac{x^2}{a^2} - \frac{y^2}{a^2}\right]^{1/2} \tag{8.27}$$

where q_0 is the surface pressure at the center of area of contact, at $x = y = 0$. At the boundary of the surface

$$\frac{x^2}{a^2} + \frac{y^2}{a^2} = 1 \tag{8.29}$$

and therefore

$$q_{x,y} = 0 \tag{8.29}$$

By summing the pressure acting on the area of contact and equating the result to P, we obtain

$$q_0 = \frac{3P}{2\pi a^2} \tag{8.30}$$

Combining Eqs. (8.24), (8.26), (8.27), and (8.30) and introducing polar coordinates, the following equation is obtained for the magnitude and distribution of the surface pressure:

$$q_r = (\frac{3n}{2\pi R_1}) \ (\frac{5v^2}{4nM})^{1/5} \ [1 - (\frac{r}{a})^2]^{1/2} \qquad (8.31)$$

$$q_0 = (\frac{3n}{2\pi R_1}) \ (\frac{5v^2}{4nM})^{1/5} \qquad (8.32)$$

Equations (8.24), (8.26), and (8.31) are the final equations that give the impact force, radius of the area of the contact, and magnitude and distribution of the surface pressure in terms of the impact velocity and geometry of the impactor, as well as the elastic properties and masses of the impactor and the target.

　　　　Impact duration. The maximum pressure q_0 occurs at a time $0.5t_0$, where t_0 is the impact duration. The latter can be determined using an approach similar to that described by Timoshenko.[27] From the problem of impact of two bodies [Eq. (8.20)] $(\alpha^2 - v^2) = \frac{4}{5} Mn\alpha^{5/2}$; then solving for $\dot{\alpha}$,

$$\alpha = (v^2 - \frac{4}{5} Mn \ \alpha^{5/2})^{1/2} \qquad (8.33)$$

Substituting $\dot{\alpha} = \frac{d\alpha}{dt}$ in Eq. (8.33) and solving for dt

$$dt = \frac{d\alpha}{(v^2 - 4/5 \ Mn \ \alpha^{5/2})^{1/2}} \qquad (8.34)$$

Combining Eq. (8.34) with Eq. (8.21) and integrating gives

$$t = \frac{2\alpha_1}{v} \int_0^X \frac{dx}{(1-x^{5/2})^{1/2}} \qquad (8.35)$$

where $x = (\alpha/\alpha_1)$. The total impact duration, t_o, is obtained by integrating between the limits $x = 0$ and $x = 1$ and is

$$t_o = 2.94 \frac{\alpha_1}{v} = 2.94 \left(\frac{5}{4Mn'v^{1/2}}\right)^{2/5} \qquad (8.36)$$

The variation of surface pressure q_0, radius of the area of contact, a, and surface pressure distribution, q_r, with time can be determined by first numerically integrating Eq. (8.35) and determining α/α_1 as a function of time t/t_o. The resultant plot is shown in Figure 8.5. The curve can be approximated fairly accurately by equation (8.37):

$$\alpha = \alpha_1 \sin \frac{\pi t}{t_o} \qquad (8.37)$$

or, substituting Eq. (8.36) for t_o,

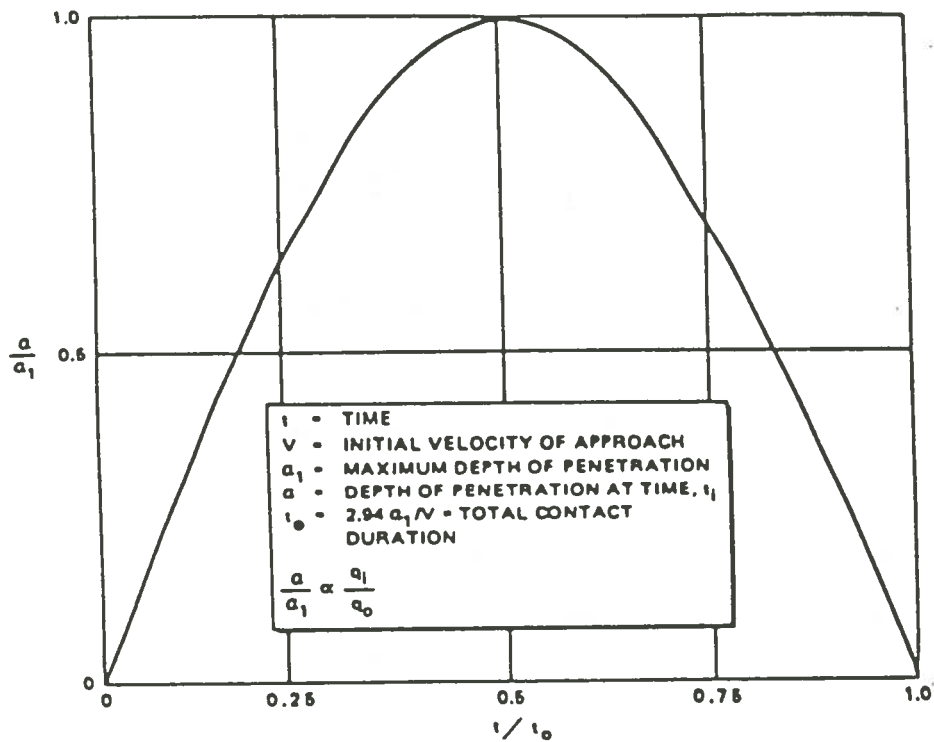$$\alpha = \alpha_1 \sin \frac{\pi t v}{2.94\alpha_1} \qquad (8.38)$$

Fig. 8.5. Generalized pressure-time relationship for a particle impacting a target. (Per Zukas[27])

Substitution of Eq. (8.14) into Eq. (8.26), and Eq. (8.30) followed by substitution of Eq. (8.38) into the resultant equations yields the following expressions for a, and q_0 as a function of time, t:

$$a(t) = (\frac{R_1}{4} \alpha_1 \sin \frac{\pi t v}{2.94\alpha_1})^{1/2} \qquad (8.39)$$

$$q_0(t) = \frac{6n}{\pi R_1} (\alpha_1 \sin \frac{\pi t v}{2.94\alpha_1})^{1/2} \qquad (8.40)$$

The distribution of surface pressure follows from Equation (8.27).

Internal stresses caused by impact pressure. Semiinfinite Isotropic Solid. In the case of semiinfinite isotropic solids subjected to surface pressure q_r distributed according to Eq. (8.27), the maximum tensile, compressive, and shear stresses (σ_t, σ_c, and σ_s, respectively) that occur in targets made of isotropic materials are related to the surface pressure by the following simple equations (Timoshenko),[27]

$$\sigma_t = (\frac{1-\nu}{3} 2) q_0(t) \qquad (8.41)$$

$$\sigma_c = q_0(t) \qquad (8.42)$$

$$\sigma_s = [(1+\nu)(s \cot^{-1} s - 1) + \frac{3}{2(1+s^2)}] q_0(t) \qquad (8.43)$$

Failure Criteria

The final step is to establish failure modes from internal triaxial stresses caused by impact-induced surface pressure. This can be done by applying appropriate failure criteria to the impact-induced triaxial stress state at each point in the target. There are two choices: (1) a failure criteria based on maximum stress or shear or (2) a failure criteria that accounts for stress interaction, such as, one based on distortion energy theory.

Chapter 9

SUMMARY AND CONCLUSIONS

The presence of loose parts in primary coolant
systems of today's nuclear reactors is a proven reality.
Loose parts monitoring is straight forward and effective
in a PWR which operates in a generally quiet mode. In
a BWR, however, the noise introduced by boiling imposes
a high background which must be overcome by any acoustical
noise detection system. A 1976 letter survey of licensees
conducted by the U.S. NRC Division of Operating Reactors
produced a wide range of both positive and negative replies
to questions regarding operational experience with these
systems. Some installations had reportedly been able to
use their LPMS's effectively, but many complained of re-
current false alarms.

The best source of information for loose parts origins
are the results from the vessel internals vibration test.
This test demonstrates the flow-induced vibration for the
following systems: a) reactor recirculation systems, b)
residual heat removal system, c) high pressure core spray
system, d) low pressure core spray system, and e) reactor
core isolation cooling system. A loose part may come
from failed or weakened internal components in the reactor
vessel. The principal components of a BWR/6 reactor vessel

internals are the vessel itself, and the internal components of the core, shroud, shroud head, steam separator, dryer assemblies, and jet pumps.

A flow blockage accident is very unlikely, but some flow blockage accidents have indeed occurred in operating reactors. The occurrence of these accidents clearly indicates that flow blockages by foreign objects are within the realm of possibility. One of the most obvious ways in which coolant flow could be restricted is for some foreign object to become lodged in the flow path of a channel. This can occur only in certain locations: the orifice could become partially restricted, an object could become lodged between the fuel support piece and the lower tie plate nosepiece, or an object could enter the fuel bundle and become lodged between fuel rods. This latter type of blockage is of less consequence than the former two because any one single objects cannot restrict enough flow to pose a serious threat to the integrity of a bundle. However, while it is possible for certain size objects to be swept upward toward the bundle entrance, the following factors tend to reduce this possibility: a) radial velocity of the flow in the lower plenum, b) boundary layer effect, c) vertical orientation of orifices.

The best practical impact sensors used with loose part monitoring systems are the piezoelectric accelerometers and the acoustic emission sensor, which both are

also used in structural vibration monitoring. An accelerometer can be idealized by a mass element connected to the case by a spring and a damping medium. The transducing element produces an electrical output proportional to the displacement of the mass element relative to the case and also proportional to the acceleration applied to the case. Each accelerometer is provided with a unique voltage and charge sensitivity calibration. Since the charge generated by the transducer does not change with cable capacitance (c_t, long and short cables), the charge sensitivity of the accelerometer system remains unaffected by cable run. This characteristic explains the practical advantage of charge-sensitive electronics over a voltage-sensitive system.

Several different transducers (in type or sensitivity), different electronic systems, and different measurement parameters are used for acoustic emission measurements. The acoustic emission transducer is a layered medium. Medium 1 is usually steel or some other metal, although it may be a non-metal in certain cases; medium 2 is the coupling layer, which may be grease or oil, or a solid; medium 3 will be the transducer protective shoe which is usually present; medium 4 will be the piezoelectric material which carries out the acoustic-electric transduction process; and medium 5 may be air, or a damping material. The acoustic emission response of a system is

modified by the thickness of the couplant depending on the frequency band being used.

Several techniques are available for location of an impact point from acoustical transducer/accelerometer arrays, including time differencing and amplitude ratioing. The Time Difference Module compares the time of arrival of an acoustic event at different sensors (channels). The first sensor to detect the event starts the location clock, the second stops it. Impact location using time difference methods is based upon the knowledge of the speed of impact wave propagation. The general formulation for impact on a flat surface in a two-dimensional cartesian coordinates system is given by

$$[(X-X_i)^2 + (Y-Y_i)^2] - [(X-X_j)^2 + (Y-Y_j)^2]^{1/2} = f(\Delta L)_{ij}$$

where $f(\Delta L)_{ij} = \Delta T_{ij} * V$

A Signal Amplitude Ratio Module (SAM) is based upon the fact that the sensor closer to the impact has higher response. This technique uses short-term-averaged, root-mean-square (RMS) signal representation. For two-dimensional impact location, $f(\Delta L)$ must be modified with ratios of acoustic path lengths such that the amplitude A_i of the ith sensor's response is inversely proportional to its distance $\bar{r}_i$ from the impact point raised to an appropriate power j, that is

$$A_i = A_o \, (\bar{r}_i)^j$$

$$\frac{[(X-X_j)^2 + (Y-Y_j)^2]^{1/2}}{[(X-X_i)^2 + (Y-Y_j)^2]^{1/2}} = A_i/A_j$$

One scheme for three-dimensional impact location is to employ the Apollonian construction. This construction locates the center of a circle which passes through a fixed point and is tangent to two given circles.

As a test facility for impact location, the tank for a subcritical assembly was modified to simulate a boiling water reactor. The tank has a radius of 58.42, wall thickness of 0.635, and a height of 152.4 centimeters. The detector array consisted of six AET model AC175L sensors mounted on the outer surface of the tank. To simulate boiling, compressed air was forced through small holes in a hose in the form of series of concentric circles layed on the fuel rod support plate near the midplane of the tank. The small holes were drilled into the hose at regular intervals; one end of the hose was sealed off, and the other was attached to an air compressor. The electronics and data acquisition system used consists of six AET model 160B preamplifiers, an eight-channel acoustic processing unit, an AET 5000 TV screen, and a printer. The sensor array provided a total of eight zones for impact location.

For each zone, all possible signal arrival patterns were input into the system.

A reproducible impact of 0.3j was obtained by firing of steel BB from a spring loaded gun at a constant distance (< .3 cm) from the outer wall of the tank. Preliminary sound velocity experiments indicated the impact wave velocity of 5474 $\pm$ 840 m/sec in the aluminum alloy tank. For each impact, information was obtained from only three sensors. This method provided two useful pieces of information: 1) the order in which the acoustic waves struck the sensors and 2) the difference in the times of arrival of the acoustic wave between sensors.

A triangulation technique based on time differencing was used to find the impact locations on the experimental subcritical assembly tank. In principle, the impact point of a loose part with the wall of a vessel can be calculated exactly from the hyperbolic equations for a three sensor array of the type

$$X^2 - Y^2 = A^2$$

The intersection of the three hyperbolas for each sensor pair will be the exact theoretical impact point. In reality, however, a number of factors introduce uncertainties into the parabola calculations, and these therefore are best represented as paths with finite width.

The uncertainties are introduced from experimental
errors such as the measurement of the speed of sound
and the finite resoluting time of the sensor. In addition,
calculational errors are added by the numerical procedure
used in determining the intersection of three parabolas
within a superimposed finite grid with a 1-cm spacing.
The impact point is located somewhere within the area
defined by the intersection of the three parabolic paths,
but cannot be established with a precision better than
that of the path widths.

Analysis of possible journeys of loose parts in a
BWR/6 reactor vessel leads to the following generalization:
It is very unlikely to have a loose part sitting on the
steam dryer assembly, but it could be left undetected in-
side the system of troughs. This object may either lodge
in the flow path or it might be carried by flow and drains
to the pool surrounding the separators and then into the
recirculation downcomer annulus between the core shroud
and reactor vessel wall. Any object that breaks loose
within the steam separator assembly may float on the water
or fall down on the upper shroud. Such an object will
slide down into the annulus between the core shroud and
vessel wall. This object would travel in any of these
three paths: 1) it can make its way into the lower plenum
through the jet pumps that have a typical nozzle diameter

of 1.3 inches with the throat diameter of 6 inches, 2) it also can go into the 20 inch reactor recirculation outlet to the suction of the reactor recirculation pumps, and 3) it may end up sitting on the baffle plate.

Damage of reactor components from loose part impact at low velocity is discussed. It is assumed that (1) the target and the impactor are linear elastic, (2) impact duration is long compared to stress-wave transit times in the impactor (or target of finite thickness), (3) the impact is normal to the target surface, and for the most general case the target is assumed to be a multilayer. These assumptions are valid for failure analysis of reactor components from loose parts impact.

Conclusions

Objective 2 of the Problem Statement leads to the conclusion that a loose part would travel in any of these three paths: 1) it can make its way into the lower plenum through the jet pumps that have a typical nozzle diameter of 1.3 inches and throat diameter of 6 inches, 2) it also can go into the 20 inch reactor recirculation outlet to the suction of the reactor recirculation pumps, or 3) it may end up sitting on the baffle plate.

Objective 4 of the Problem Statement was to determine an appropriate procedure to assess the probability of

failure of reactor-vessel component from loose parts impact. Mathematical development based upon path analysis and flow velocity distribution resulted in equations from which stresses may be calculated. Necessary input parameters for these calculations have been identified, but were not available for this thesis. Results for single and repeated impacts would be an important continuation for this work.

Objective 5, characterization of sensors and sensing techniques, was met to the extent that existing published work and manufacturer's literature was reviewed. Candidate sensors and sensing techniques have been identified but will require direct experimental tests in the simulator facility to establish optimum operating characteristics.

Conclusions which may be drawn from objective 6 for impact location are listed below:

1) For this particular experimental configuration an impact point must be farther than 7.5 inches from the closest sensor in the array. At distances closer than this, ΔT values were spurious, and location calculations were meaningless.

2) At least four sensors are required to find the impact point. The condition is such that the distance between any two sensors should be greater than twice the

minimum useful distance to a sensor so that no more than one sensor can be within the minimum 7.5 inches.

3) No convincing minimum in the plot of uncertainty as a function of the impact-to-sensor distance can be discerned.

4) Both Apollonian construction, and parabolic intersection programs developed in this work would be too slow and somewhat impractical for routine industrial use.

5) No effect from simulation of boiling at atmospheric pressure was noticed for the arrangement described in Chapter 6.

6) Experimental data for the tank full and half full of water represent did not indicate any noticable differences in ΔT measurements.

Recommended Minimum Number and Approximate Location of Acoustical Emission Sensors on BWR/6

There are some limitations and restrictions for locating the sensor. For example, the NRC does not allow the mounting of sensors directly on the reactor vessel, therefore these must be mounted on the exterior of primary system piping and other components. It is very difficult to place a sensor in the center of the bottom of a reactor vessel because of the forest of control-rod drive shrouds located there.

Not withstanding these restrictions and difficulties, the ideal array of sensors suggested by the experimental

results would be to locate four sensors on the bottom head
of the reactor vessel in such a way that three are on the
outer edge (120° apart) and one is in the middle. These
sensors should be attached on the control-rod drive shrouds
as close as possible to their intersections with reactor
bottom head. At least one sensor is required for each of
the following locations: instrumentation nozzle (upper
vessel), recirculation water inlet, and feedwater inlet.
More sensors will give better results in finding where the
loose part comes from originally and where it will end up.
High frequency acoustical emission sensors should be used
to avoid detection of small disturbances due to control
rod movement, vibration, and general background noise
from coolant flow and any other sources. Attachment of
sensors to rod-drive shrouds near the center of the vessel
bottom will be difficult, but should be possible with
specially designed tools.

Recommendations for Future Work

The work accomplished for this thesis has opened avenues for further experimentation, and has pointed to other areas which need additional attention. Specifically, more study needs to be done to determine:

1. The sensitivity of the predicted impact location to variations of parameters and conditions which have been listed in the text,

2. The location of impact when sensors are not directly attached to the vessel,

3. Modifications of impact location techniques using acoustical emission equipments useful for practical purposes to industry.

4. Methods of attachment, considering temperatures and radiation levels that exist during full power operation,

5. Failure mechanisms from repeated impact, and

6. Periodic calibration of sensors remotely.

Additional information also must be obtained for operational BWR/6 reactors with regard to vibration tests and noise signatures to improve knowledge of loose parts origins and required sensor characteristics.

REFERENCES

1. "Loose-part detection program for the primary system of light-water-cooled reactors", Regulatory Guide 1.133, U.S. Nuclear Regulatory Commission, pp. 1.133-2, Revision 1, May 1981.

2. Ibid., pp. 1.133-1.

3. Charles Jackson, The Practical Vibration Primer, Gulf Publishing Company, Book Division, Houston, 1979, pp. 2-9.

4. R. C. Kryter, C. W. Ricker, Characteristics and performance experience of loose-part monitoring systems in U.S. commercial power reactors, prepared for U.S. Nuclear Regulatory Commission, ORNL/NUREG/TM-254, pp. 2.

5. "Meeting of the subcommittee on electrical systems, control and instrumentation on loose part monitoring systems", Advisory Committee on Reactor Safeguards, Nuclear Regulatory Commission, Los Angeles, CA, pp. 60-61.

6. Ibid., pp. 62-63.

7. R. T. Lahey, Jr. and F. J. Moody, The thermal-hydraulics of a boiling water nuclear reactor, American Nuclear Society, pp. 15-23.

8. "General description of a boiling water reactor (BWR/6)", Nuclear Energy Group, revised Sept. 1980, pp. 2-2.

9. Consequences of a postulated flow blockage incident in a boiling water reactor, licensing topical report, General Electric Company, NEDO-10174, October 1977, pp. 3-4.

10. Ibid., pp. 5-41.

11. Ibid., pp. 5-42.

12. Ibid., pp 3-6 to 3-10.

13. Ibid., pp. 3-13.

14. "Piezoelectric Accelerometers", No. 101, Endevco-Dynamic Instruments Division, 1969, pp. 3-11.

15. F. Shahrokhi, "Metallic loose-part detection and characterization", a dissertation at the University of Tennessee, Knoxville, TN, June, 1980, pp. 23-28.

16. R. Hill and Samir M. A. El-Dardiry, "Variable in the use and design of acoustic emission transducers", Advances in acoustic emission, Proceedings of International Conference on Acoustic Emission, Dunhart Publishers, Knoxville, TN, 1981, pp. 22-38.

17. Hill, R., El-Dardiry, S.M.S., "A theory for optimization in the use of acoustic emission transducers", (in press), (Per R. Hill et al. ibid., p. 25).

18. de Klerk, J., "Thin film piezoelectric transducers used as generators and detectors of microwave phonons with some attentuation measurement in SiO2", J. Appl. Phys. 33, 4522-4528, (1966), (Per R. Hill et al., ibid., p. 24).

19. Thompson, W. T., "Transmission of elastic waves through a stratified solid medium", J. Acoust. Soc. Am., 21, 89-93 (1950) (Per R. Hill et al. ibid., p. 25).

20. Preliminary operating instructions for the AET 5000, Acoustic Emission Technology Corporation, Sacramento, CA, pp. II-50-II-52.

21. F. Shahrakhi, Loc. cit., pp. 50-55.

22. R. C. Kryter, F. Shahrokhi, Summary of studies on methods for detecting, locating, and characterizing metallic loose parts in nuclear reactor coolant system, NUREG/CR-2344, pp. 18-20.

23. N. O. Cross, L. L. Laushin, and J. L. Thompson, "Acoustic emission testing of pressure vessels for petroleum refineries and chemical plants," Acoustic Emission, STP 505, American Society for Testing and Materials, pp. 270-296.

24. J. L. Meriam, Engineering Mechanics, Volume 2, Dynamics, John Wiley & Sons, New York, pp. 156-158.

25. Ibid., pp. 190-193.

26. F. Shahrokhi, Loc. cit., pp. 12-14.

27. Zukas, Nicholas, Swift, Greszzuk, and Curran, Impact dynamics, John Wiley & Sons, New York, pp. 55-75.

28. Personal communication with Dr. J. C. Courtney.

APPENDIX A

Pattern Recognition Techniques for Impact Location[28]

This method uses the signal arrival time from impact to the accelerometer. The arrival time, as obtained from accelerometers, is used for the pattern information that is inherent in impact position. Different impact positions may have different patterns, but the same impact positions may have the same or very similar patterns. In this method, the information of patterns corresponding to reference impact positions are previously collected in a reference pattern library in a computer memory. The impact position is determined as being in some neighborhood of the reference impact position that has a pattern closest to that of the impact to be located. To select the closest pattern from the library, the distance between the patterns must be defined as an index of the pattern similarity. The pattern distance, D^T between impact positions A and B is defined as:

$$D^T = [\frac{1}{N} \sum_{i=1}^{N} (\Delta T_i - \overline{\Delta T})^2]^{1/2}$$

where

$$\Delta T_i = \tau A_i - \tau B_i$$

$$\overline{\Delta T} = \frac{1}{N} \sum_{i=1}^{N} \Delta T_i$$

τ_{Ai}, τ_{Bi} = impact time to the ith accelerometer from impact A and B, respectively.

140

N = number of accelerometers.

The relationship between the pattern distance and the actual impact distance is studied (by S. Izumi, M. Senoh-Hitachi Erl-Japan) using impact data from nine accelerometers attached on a cylindrical steel tank with a height of 5 m and a diameter of 2 m. Experimental results were plotted in Figure A.1. The pattern distance, D^T, has a strong correlation with the impact distance; however, D^T still has a deviation of 20%. This deviation is caused by the fact that D^T is not exactly proportional to the actual distance. The traces of pattern distances corresponding to unknown impact positions on coaxial circles with radii of 0.2, 0.4, 0.6, 0.8, and 1.0 m about a reference impact on the tank outer wall are calculated theoretically and shown in Figure A.2. The traces of the pattern distance are distorted and variable, depending on the direction of the unknown impact position from the reference impact. The deviation of pattern distance in Figure A.1 can be reduced by a correction based on the theoretical calculation results. After this correction, a deviation of 5% is obtained. From this, we can conclude that the actual distance between two impacts can be estimated from the corrected pattern distance and the pattern recognition technique can be applied to the location of impact position on pressure vessels.
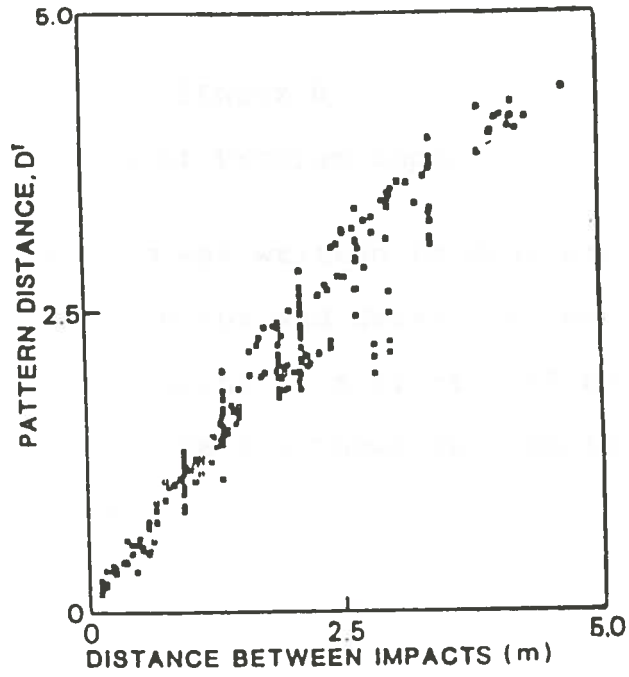
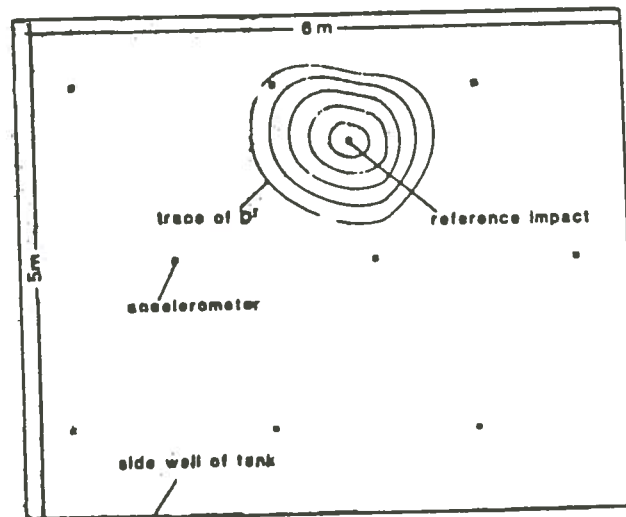Fig. A.1. Relationship between pattern distance and impact distance

Fig.A.2. traces of pattern distance corresponding to unknown impacts on coaxial circles with radii of 0.2,0.4,0.6,0.8,and 1.0 m (calculated)

APPENDIX B

A Listing of Program Impact

A computer program was written to generate the finite-width parabolic paths and determine the area of intersection. The following is a listing of basic impact of program. Figure B.1 shows an example of finite-width parabolic paths.

```
10 REM  "IMPACT" IS A POINT PLOTTING ROUTINE
20 SF=3
30 REM
40 REM   MCILHENNY & ZADAFSHAR / NSC / MARCH, '84
50 REM
60 REM   DEFINE CONSTANTS
70  YF=.4843:XOFF=100:YOFF=224
80 REM   SET SYSTEM FIXED POINTS
90  CLS
100  FOR I=1 TO 4: READ X(I),Y(I): NEXT I
110  READ DT12,DT13,DT23
120  V=5474.25
130  V=V*.0001
140  VT12=DT12*V:VT13=DT13*V:VT23=DT23*V
150 REM   PLOT POINTS
160  CLS
170  FOR I=1 TO 4
180    IF I<4 THEN C=2 ELSE C=4
190    X=X(I):Y=Y(I):GOSUB 520
200  NEXT I
210 REM   SEARCH FOR FIRST LOCUS
220  FOR E=.03 TO .3 STEP .02
230   FOR I= 35 TO 100 STEP .5
240    FOR J=10 TO 70  STEP .5
250     X=I:Y=J
260     P1=0:P2=0:P3=0
270     LOCATE 5,1:PRINT I,J,E
280     RP1=(X-X(1))^2+(Y-Y(1))^2
290      IF RP1<0 THEN RP1=0 ELSE RP1=SQR(RP1)
300     RP2=(X-X(2))^2+(Y-Y(2))^2
310      IF RP2<0 THEN RP2=0 ELSE RP2=SQR(RP2)
320     RP3=(X-X(3))^2+(Y-Y(3))^2
330      IF RP3<0 THEN RP3=0 ELSE RP3=SQR(RP3)
340     T12=ABS(RP1-RP2)/VT12
350      IF T12<1-E OR T12>1+E THEN 380
360     P1=1
370      C=1:GOSUB 520
380     T13=ABS(RP1-RP3)/VT13
390      IF T13<1-E OR T13>1+E THEN 420
400     P2=1
410      C=3:GOSUB 520
420     T23=ABS(RP2-RP3)/VT23
430      IF T23<1-E OR T23>1+E THEN 480
440     P3=1
450     IF P1=P2 AND P1=P3 AND P1=1 THEN 455 ELSE 470
455     A1=ABS(X-X(4))
456     A2=ABS(Y-Y(4))
457     A=A1*A2
458     FR=A/34374.13
459     LPRINT "X =";X(4);"  Y =";Y(4)
460     LPRINT "X =";X;"   Y =";Y;"      ERROR =";E"     AREA =";A;" FRACTION =";FR
470      C=5:GOSUB 520
480    NEXT J
490   NEXT I
500  NEXT E
510 END
520 REM   POINT PLOT SUBROUTINE
530  XP=XOFF+SF*X
540  YP=(YOFF-YF*SF*Y)
550  PSET (XP,YP),C
560 RETURN
570  DATA 30.48,46.99,121.92,88.9,121.92,12.7,60.96,58.42
580  DATA 65,84.19
```
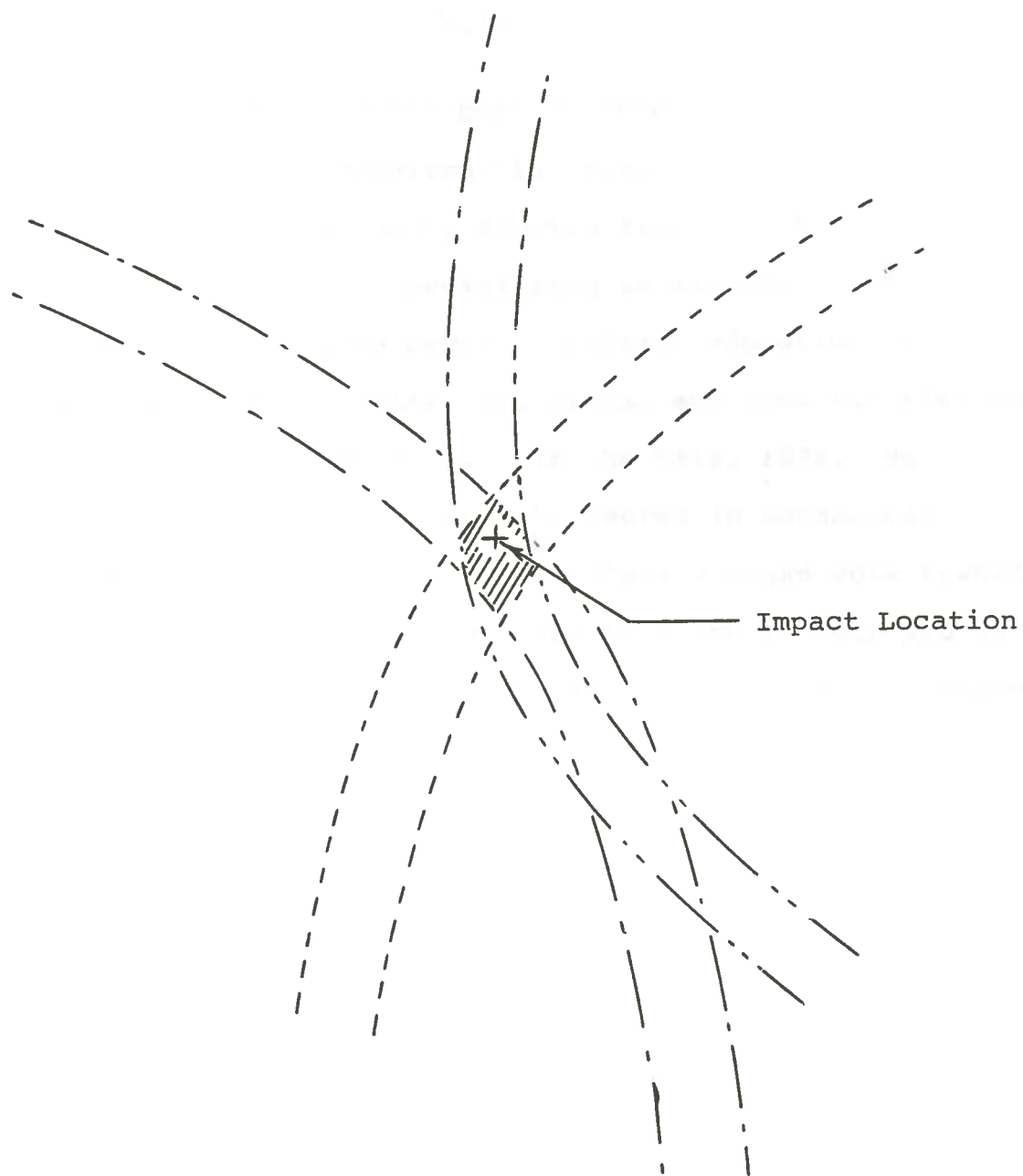
Fig. B.1.   Representation of parabolas as paths with
a finite width

VITA

Hosein Zadafshar was born on June 19, 1959 in Isfahan, Iran. He received his primary and secondary education in Isfahan and graduated from Adab-Sadi High School in June, 1976, specializing in mathematics. In the summer of 1977, he began his college education at the University of Southwestern Louisiana, and then transferred to Louisiana State University in the Fall, 1978. He received his bachelor of science degree in mechanical engineering in May 1981. He immediately began work toward a M.S. degree in nuclear engineering which he received in May 1984. He is currently happily married to Maryam Shams Josdany.